Title

Falling through spacetime : four studies in neutrino astrophysics

Author

Kishimoto, Chad T.

Publication Date

2009

UNIVERSITY OF CALIFORNIA, SAN DIEGO

Falling through Spacetime: four studies in neutrino astrophysics

A dissertation submitted in partial satisfaction of the
requirements for the degree
Doctor of Philosophy

in

Physics

by

Chad T. Kishimoto

Committee in charge:

Professor George Fuller, Chair
Professor Patrick Diamond
Professor Bruce Driver
Professor Kevin Quest
Professor Arthur Wolfe

2009

The dissertation of Chad T. Kishimoto is approved, and it is acceptable in quality and form for publication on microfilm:

Chair

University of California, San Diego

2009

DEDICATION

for Carrie

EPIGRAPH

Neutrinos, they are very small.
They have no charge and have no mass
And do not interact at all.
The earth is just a silly ball
To them, through which they simply pass,
Like dustmaids down a drafty hall
Or photons through a sheet of glass.
They snub the most exquisite gas,
Ignore the most substantial wall,
Cold shoulder steel and sounding brass,
Insult the stallion in his stall,
And scorning barriers of class,
Infiltrate you and me! Like tall
and painless guillotines, they fall
Down through our heads into the grass.
At night, they enter at Nepal
and pierce the lover and his lass
From underneath the bed - you call
It wonderful; I call it crass.

—John Updike

TABLE OF CONTENTS

LIST OF FIGURES

LIST OF TABLES

ACKNOWLEDGEMENTS

First and foremost, I would like to thank my advisor, George Fuller, without whom this dissertation would not be possible. His support – financial, scientific, and professional – has been an invaluable aspect of my graduate tenure and a great boon for my career. I appreciate the opportunities he has given me, from providing me the means to travel to conferences around the world, to ensuring my funding, especially during the time of my wedding. His physical insight has allowed me to achieve a greater appreciation of physics, and in particular astroparticle physics, a field I would never have envisioned myself in before entering graduate school.

I would like to thank a couple of my colleagues who have facilitated me in the work that appears in this dissertation. Justin Kao, who has helped me with many computational aspects associated with this work, and Christel Smith, who I have collaborated with, shared an office with and commiserated about the travails of graduate work with.

Six years in graduate school can be a tiring ordeal; I would like to thank those who have helped me pass the time: those who I have shared an office with, those who I have grilled with, and those who I have spent countless hours at CASS tea time with. I would like to acknowledge those who allowed me to take my mind off work, including the Monday night volleyball group, Sunday Softball, and the Pomerado Community Band. I am grateful for the camaraderie of Teddy Yu, Megan Kennedy, Daniel Wu, Stephanie Chan, Ginna & Nate Vandelinder, Marc & Lauren Rafelski, and many others who have helped me to live life to its fullest.

I would be remiss without acknowledging the National Science Foundation and Department of Energy who have funded the grants that have paid my tuition and stipend throughout my graduate tenure. I am also thankful to the Achievement Rewards for College Scientists (ARCS) Foundation, Inc. for financial support.

Finally, and most importantly, I would like to thank my family. I am very fortunate to have four loving parents who have supported my endeavors throughout my life, in particular financially supporting my Caltech education. A special debt of gratitude is owed to my wife who has loved and supported me throughout this entire process. I appreciate her enduring support, understanding, and sacrifices she continues to make to allow me to pursue a career in science.

Chapter 2, in part, is a reprint of material previously published as C. T. Kishimoto, G. M. Fuller, and C. J. Smith, "Coherent Active-Sterile Neutrino Flavor Transformation in the Early Universe", *Physical Review Letters* **97**, 141301 (2006). I was the primary investigator and author of this paper.

Chapter 3, in full, is a reprint of material previously published as C. T. Kishimoto and G. M. Fuller, "Lepton Number-Driven Sterile Neutrino Production in the Early Universe", *Physical Review* D**78**, 023524 (2008). I was the primary investigator and author of this paper.

Chapter 4, in full, is a reprint (with the exception of the citation style, which has been revised to ensure consistency with the rest of the dissertation) of material previously published as C. T. Kishimoto and G. M. Fuller, "Neutrino-Accelerated Hot Hydrogen Burning", *Astrophysical Journal* **656**, 1104 (2007). I was the primary investigator and author of this paper.

Chapter 5, in part, is a reprint of material previously published as G. M. Fuller and C. T. Kishimoto, "Quantum Coherence of Relic Neutrinos", *Physical Review Letters* **102**, 201303 (2009). I was the primary investigator and author of this paper.

VITA

2003	Bachelor of Science with Honor in Physics, California Institute of Technology, Pasadena, CA
2003-2004	Teaching Assistant, University of California, San Diego
2004-2009	Research Assistant, University of California, San Diego
2009	Doctor of Philosophy in Physics, University of California, San Diego

PUBLICATIONS

G. M. Fuller and C. T. Kishimoto, “Quantum Coherence of Relic Neutrinos”, *Physical Review Letters* **102**, 201303 (2009).

C. T. Kishimoto and G. M. Fuller, “Lepton Number-Driven Sterile Neutrino Production in the Early Universe”, *Physical Review* D**78**, 023524 (2008).

C. J. Smith, G. M. Fuller, C. T. Kishimoto and K. N. Abazajian, “Light Element Signatures of Sterile Neutrinos and Cosmological Lepton Numbers”, *Physical Review* D**74**, 085008 (2006).

C. T. Kishimoto, G. M. Fuller and C. J. Smith, “Coherent Active-Sterile Neutrino Flavor Transformation in the Early Universe”, *Physical Review Letters* **97**, 141301 (2006).

C. T. Kishimoto and G. M. Fuller, “Neutrino-Accelerated Hot Hydrogen Burning”, *Astrophysical Journal* **656**, 1104 (2007).

ABSTRACT OF THE DISSERTATION

Falling through Spacetime: four studies in neutrino astrophysics

by

Chad T. Kishimoto
Doctor of Philosophy in Physics

University of California San Diego, 2009

Professor George Fuller, Chair

For a significant fraction of the history of the universe, neutrinos freely fall through spacetime. While they only weakly interact with matter, neutrinos have a significant impact in astrophysics. Experimental neutrino physics and observational cosmology are amidst an interesting era, where precision measurements in both fields have significantly improved scientific understanding of the standard model of particle physics and of the universe. Experiments in neutrino physics have not only discerned that neutrinos are massive particles, but have also measured their relative masses (but not their absolute masses) and the quantum mechanical mixing matrix that is a consequence of these differing mass scales. Meanwhile, precision cosmological observations have determined the energy content of the universe, which in turn has presented a self-consistent story of the history and evolution of the universe and its contents.

The topics discussed in this dissertation are based upon an interplay between these two fields, at times pushing the envelope, but always focused upon the basic physical processes that affect massive neutrinos in an expanding universe. A hearty, pedagogical introduction is presented to highlight the relevant neutrino physics described in this work and an overview of cosmology, strongly biased toward the early universe, the paradigm in which much of the work in this dissertation is based. Sterile neutrinos in different regimes of mass and mixing with active neutrinos are proposed as well as asymmetries between the number density of active neutrinos and antineutrinos in the early universe. The consequences of these two propositions are discussed in terms of observables such as primordial light element abundances and the observables related to a sterile neutrino dark matter candidate. Neutrino emission from high-entropy electron-positron plasmas are introduced, and the effects of this large flux of neutrinos and antineutrinos on hot hydrogen burning are explored. Finally, the nature of the cosmic neutrino background, a relic of the hot Big Bang, is discussed as they freely fall through spacetime from weak decoupling to the present epoch.

Chapter 1

Introduction

Throughout this dissertation, with the exception of Chapter 4 and where ever it is otherwise stated, natural units will be used where $\hbar = c = k_B = 1$. Since there are four independent units associated with these physical constants (length, mass, time, temperature), making three dimension-full constants dimensionless results in one remaining unit. In this dissertation, energy is used as the remaining unit, in particular the MeV is a useful unit when discussing astroparticle physics in the early universe. Appendix A summarizes the conversion between these units.

1.1 Neutrino Physics

The story of the neutrino begins in 1896 with the chance discovery of radioactivity by Henri Becquerel [1]. In 1914, James Chadwick found that the energy spectrum of β-radiation was continuous, not discrete as was the case for α- and γ- radiation [2]. This result presented a fundamental problem: quantum mechanics dictates that the energy levels of the nucleus are quantized, so a continuous spectrum of β-radiation would be inconsistent with energy conservation.

In response to this apparent contradiction, Wolfgang Pauli proposed the existence of a light, neutral fermion which he called a “neutron” (this preceded the discovery of the neutron). In an open letter to attendees at the Gauverein meeting in Tübingen in December 1930, Pauli addresses the “Dear Radioactive Ladies and Gentlemen,” proposing a “desperate remedy to save . . . the law of conservation of energy.” By proposing this light, neutral fermion, “the continuous beta spectrum would then make sense with the assumption that in beta decay, in addition to the electron, a neutron [neutrino] is emitted such that the sum of the energies of neutron [neutrino] and electron is constant” [3]. Pauli remained apprehensive of his proposition, remarking that “I have done something very bad today by proposing a particle that cannot be detected; it is something that no theorist should ever do.” Obviously, attitudes among theoretical particle physicists have changed where unexplained signs of energy non-conservation are met with the proposal of new particles and the existence of undetected (and sometimes undetectable) particles are theorized with impunity.

In 1932, Chadwick discovered the neutron. As it became evident that the particle was not the “neutron” proposed by Pauli, a new name had to be adopted. Enrico Fermi coined the term neutrino (“little neutral one”) as a pun on the Italian word for neutron. In 1956, Frederick Reines and Clyde Cowan, Jr. performed the first successful neutrino detection experiment. The experiment was designed to detect antineutrinos from a nuclear reactor using a large tank of water. Energetic antineutrinos capture on protons in the water (inverse β-decay), producing a positron and a neutron,

$$\bar{\nu}_e + p \rightarrow n + e^+. \tag{1.1}$$

A liquid scintillator was used to observe the high energy photons that result when the positron quickly annihilates with an electron in the water. To improve the quality of the signal, $CdCl_2$ was added to the water. The cadmium nuclei capture the neutron, releasing a photon. This provides a consistency check where a neutrino capture induces photons from electron-positron annihilation followed by a photon produced when the neutron is captured (on a timescale determined by the mean free liftetime of the free neutron in the cadmium solution) [4].

Parity is conserved in the gravitational, electromagnetic, and strong interactions, and it was widely believed that parity was also conserved in weak interactions. If parity is conserved, then both left-handed and right-handed particles have the same interactions. (Particles of a given handedness are eigenstates of the chirality operator and handedness is a relativistic invariant. When particles are massless, then their chirality is equivalent to their helicity — the relationship between spin and momentum.) However, Tsung Dao Lee and Chen Ning Yang proposed that parity may be violated in weak interactions [5]. This conjecture was confirmed by C. S. Wu and her collaborators [6]. Goldhaber, Grodzins and Sunyar determined that parity is maximally violated; that is neutrinos are left-handed and antineutrinos are right-handed [7].

The Glashow-Weinberg-Salam standard model is the cornerstone of the current theoretical understanding of the weak interaction. AT its core is the $SU(2) \times U(1)$ gauge group, proposed by Sheldon Glashow to unify the electromagnetic and weak forces [8]. Weinberg [9] and Salam [10] built upon Glashow's electroweak model the theoretical foundations that successfully describe the weak interaction. They introduced the Higgs mechanism to the standard model which, whenever electroweak symmetry is broken, allows the gauge bosons that mediate the weak force to be massive. Charged current interactions (*e.g.*, β-decay) are mediated by the W^+ and W^- bosons. A natural consequence of the Glashow model was the existence of previously unobserved weak neutral currents which are mediated by the Z^0 boson. Gerardus 't Hooft and Martinus Veltman showed that this standard model was renormalizable [11], making the theory more attractive to theorists. The experimental discoveries of neutral current interaction in 1973 [12] and of the $W^\pm$ and Z^0 bosons in 1983 [13, 14] established the standard model as the prevailing theory in describing the weak and electromagnetic interactions.

The width of the decay of the Z^0 boson constrains the number of generations of active neutrinos. The width of the Z^0 decay (in energy) is proportional to its decay rate, both into particles that can be observed and into "invisible" particles (*i.e.*, neutrinos). Using Fermi's golden rule, the invisible decay rate (or the "invisible width" as it is commonly called) is proportional to the strength of the weak interaction and the number of neutrinos (with $m_\nu \lesssim m_{Z^0}/2$) that are coupled by the weak neutral current. The number of generations of active neutrinos was fixed at three from the results of Z^0 decay experiments performed at the Large Electron-Positron (LEP) collider at CERN [15].

This completed the standard model of the weak interaction. There are three generations of leptons (electrons, muons, and tauons and their associated neutrinos) corresponding to the three generations of quarks. The three generations of neutrinos are called the three active neutrino flavors — ν_e, ν_μ, and ν_τ. Charged current interactions — whose interaction vertices change down-type quarks to up-type quarks and charged leptons to their associated neutrinos (and vice versa) — are mediated by the W^- (W^+) boson, while neutral current interactions — whose interaction vertices do not change the type of particle — are mediated by the Z^0 boson.

The neutrinos were considered massless, as there was no evidence to the contrary, although there was the sticky situation that there is no symmetry that protects neutrinos from being massive (for example, gauge symmetry and general covariance protects photons from being massive). If neutrinos are massless, then left-handed neutrinos and right-handed antineutrinos, the chiral states that are participate in the weak interaction, are considered in the standard model while neglecting their parity-related counterparts (right-handed neutrinos and left-handed antineutrinos), which are not affected by the weak interaction.

Maki, Nakagawa, and Sakata suggested that neutrinos, like quarks, may oscillate between flavors. If neutrinos have different masses, then each neutrino flavor state may be a superposition of multiple mass states, which would result in one flavor oscillating into another [16]. This conjecture was verified (by accident) by the Homestake experiment conducted by Raymond Davis, Jr. and his collaborators in the Homestake Gold Mine at Lead, South Dakota. In the experiment, a 100,000 gallon tank of dry cleaning fluid, perchloroethylene, was placed 1,478 meters below ground in the mine. The inverse β-decay reaction

$$\nu_e + {}^{37}\mathrm{Cl} \rightarrow {}^{37}\mathrm{Ar} + e^-, \tag{1.2}$$

was utilized to detect neutrinos produced in the fusion reactions in the core of the sun (in particular, the β^+-decay of ^{8}B). The radioactive argon atoms were then counted to discern the number of neutrino reactions that took place in the experiment. The data implied that there was a large deficit of neutrinos coming from the sun. Approximately one-third as many neutrinos were detected as were predicted by the standard solar model [17, 18]. This is known as the solar neutrino problem. While this result was met with obvious skepticism, it has withstood increased scrutiny and more sophisticated experiments. Neutrinos change their flavor between the time they are produced in the core of the sun and the time they travel to Earth.

Further experimentation at the Sudbury Neutrino Observatory, along with other experiments, validated this interpretation of the solution to the solar neutrino problem. The Sudbury Neutrino Observatory (SNO) is a heavy water Cerenkov detector located in the Creighton mine in Sudbury, Ontario, Canada. A water Cerenkov detector detects neutrinos by detecting the charged leptons (often electrons and sometimes muons) created in neutrino interactions. These ultra-relativistic charged leptons travel faster than the speed of light in water (approximately $0.75c$), emitting a cone of Cerenkov radiation about its direction of motion.

In the SNO experiment, one kiloton of heavy water (D_2O) is used to detect solar neutrinos through charged current interactions ($\nu_e + d \rightarrow 2p + e^-$), neutral current interactions ($\nu_\alpha + d \rightarrow p + n + \nu_\alpha$), and elastic scattering interactions ($\nu_\alpha + e^- \rightarrow \nu_\alpha + e^-$) which incorporate both charged and neutral current interactions (for $\alpha = e$, μ, τ). By measuring both charged current and neutral current interactions, SNO determined the total flux of neutrinos (of all flavors) coming from the sun. The data confirmed the Homestake results that one-third of the expected flux of electron neutrinos were detected, and found that the total neutrino flux was consistent with the expected electron neutrino flux calculated from the standard solar model [19, 20].

Experimental measurements of neutrinos created in the atmosphere, in particular the ratio of muon neutrinos to electron neutrinos, has also provided evidence for neutrinos being converted from one flavor to another. Atmospheric neutrinos are created when high energy cosmic rays bombard the atmosphere, creating pions, whose main decay channel is into muons and muon neutrinos. In turn, the muons decay into electrons and both electron and muon neutrinos,

$$\begin{aligned} \pi^+ &\rightarrow \nu_\mu + \mu^+ \rightarrow \nu_\mu + \bar{\nu}_\mu + \nu_e + e^+ \\ \pi^- &\rightarrow \bar{\nu}_\mu + \mu^- \rightarrow \bar{\nu}_\mu + \nu_\mu + \bar{\nu}_e + e^-. \end{aligned} \tag{1.3}$$

The atmospheric neutrinos have energies of ~ 100 MeV to ~ 100 GeV, much higher energies than the solar neutrinos. By inspection of the reactions (1.3), the ratio of the neutrinos fluxes ought to satisfy

$$\frac{\phi_{\nu_\mu} + \phi_{\bar{\nu}_\mu}}{\phi_{\nu_e} + \phi_{\bar{\nu}_e}} \approx 2. \tag{1.4}$$

Water Cerenkov detectors are able to discern the difference between electron and muon neutrinos at these energies. Neutrino-nucleon collisions produce charged leptons of the same flavor as the neutrino. The charged lepton is then distinguished by the shape of its Cerenkov radiation. The first evidence of the ratio of muon neutrinos to electron neutrinos being different from the theoretical value came from the Kamioka Nucleon Decay Experiment (Kamiokande) located in the Kamioka mine in the Gifu prefecture of Japan, where this ratio was significantly smaller than two. This observation, combined with an angular variation of this ratio strongly supports the interpretation that quantum mechanical oscillations are responsible for muon neutrino disappearance [21].

An understanding of the solar neutrino problem and atmospheric neutrino oscillations have provided us a window into neutrino physics beyond the standard model where neutrino masses were not included. This points toward the idea that neutrinos have mass and that they have nonzero mixing between flavors. It is an exciting time in neutrino physics, as experiments on solar neutrinos, atmospheric neutrinos, and neutrinos produced in nuclear reactors and accelerators, have combined to constrain the parameters of the neutrino mixing matrix [just as the CKM matrix describes oscillations in the quark sector, the MNS (Maki-Nakagawa-Sakata) matrix describes neutrino oscillations] and the differences of the squares of the neutrino masses. While a lot of headway has been made in these experimental aspects, there remains a lot of work to be done, including further constraining the parameters in the mixing matrix and determining the absolute masses of the neutrinos.

1.1.1 The Weak Interaction

The weak interaction is aptly named, as it is about 10^{11} times weaker than electromagnetic interactions and about 10^{13} times weaker than strong interactions. However, the weak interaction plays an integral role in creating the universe that we live in. Unlike the other fundamental forces, the weak interaction is capable of changing protons to neutrons (and vice versa), enabling the primary mode of energy generation in the universe: the fusion of four protons to helium nuclei. The weak reactions are much slower than the electromagnetic and strong reactions in the reaction chain that culminates in nuclear fusion, so the weak reactions are the rate-limiting steps in the energy generation process. While the weak interaction may be weak, it holds a mighty role in determining the evolution of astrophysical objects.

The Glashow-Weinberg-Salam standard model has served as the theoretical basis for the understanding of the weak interaction. There are three generations of fermions, and each generation has two quarks, a charged lepton, and a neutrino (which is also a lepton) :

Quarks	up	charm	top
	down	strange	bottom
Leptons	e^-	μ^-	τ^-
	ν_e	ν_μ	ν_τ

The properties, other than mass, are very similar across generations. Up-type quarks (up, charm, top) have a charge of $+2/3\,e$, while down-type quarks (down, strange, bottom) have a charge of $-1/3\,e$. The charged leptons have a charge of $-e$ while the neutrinos are neutral. The mass of the particles increase with successive generations (when moving from left to right above). Quarks participate in all four fundamental forces, but at low energies are constrained to be in color singlets — bare quarks do not exist at low energy scales. Charged leptons, on the other hand, are not affected by the strong force but experience the other three forces, while neutrinos only participate in the weak and gravitational interactions.

The weak interaction is mediated by three gauge bosons, W^+, W^-, and Z^0. The mass of the $W^\pm$ bosons is $m_{W^\pm} = 80.398 \pm 0.025$ GeV and the mass of the Z^0 boson is $m_{Z^0} = 91.1876 \pm 0.0021$ GeV [22]. The large masses of the gauge bosons are responsible for both the weakness of the weak interaction and the fact that the weak interaction is a short-range force. This range of the force can be estimated from Heisenberg's Uncertainty Principle and the mass of the bosons to be $\sim 10^{-3}$ fermi (a fermi is approximately the size of a proton). So, the weak interaction is essentially a contact force.

Charged current interactions are mediated by the $W^{\pm}$ bosons. In a charged current interaction, down-type quarks are converted to up-type quarks or charged leptons are converted into their associated neutrino (or vice-versa), accompanied by the exchange of a W^{-} (or W^{+}) boson. Figure 1.1 shows examples of a number of charged current interactions. There is one complication when it comes to the charged current interaction with quarks. Quarks mix with other quarks of the same type in other generations. This mixing allows any up-type quark to have a charged current interaction with any down-type quark; the strength of this interaction modified by the Cabibo-Kobayashi-Masakawa (CKM) matrix. The CKM matrix is a unitary matrix that contains the observable effects of quark mixing (*i.e.*, quantum mechanical superposition) [23, 24]. As a result, the β-decay of a neutron (a neutron has quark content *udd*) is similar to the β-decay of a Λ particle (quark content *usd*), where both particles decay to a proton, electron, and electron antineutrino. The neutron decay has $d \rightarrow u$ and the Λ decay has $s \rightarrow u$; this is an example of a flavor changing charged current interaction in the quark sector.

Neutral current interactions are mediated by the Z^0 boson. As seen in Figure 1.2, the neutral current affects any particle with weak charge (that is, any particle that participates in the weak interaction) and does not change the particle. However, one may ask in a similar vein to the discussion of flavor changing charged currents, does quark mixing create flavor changing neutral currents? Can an up-type quark be converted into a different up-type quark through the neutral current? Glashow, Iliopoulos and Maiani showed that since the CKM matrix is unitary, there are no flavor changing neutral currents [25]. This is called the GIM mechanism. An interesting point is that the interaction vertices shown for the neutral current in Figure

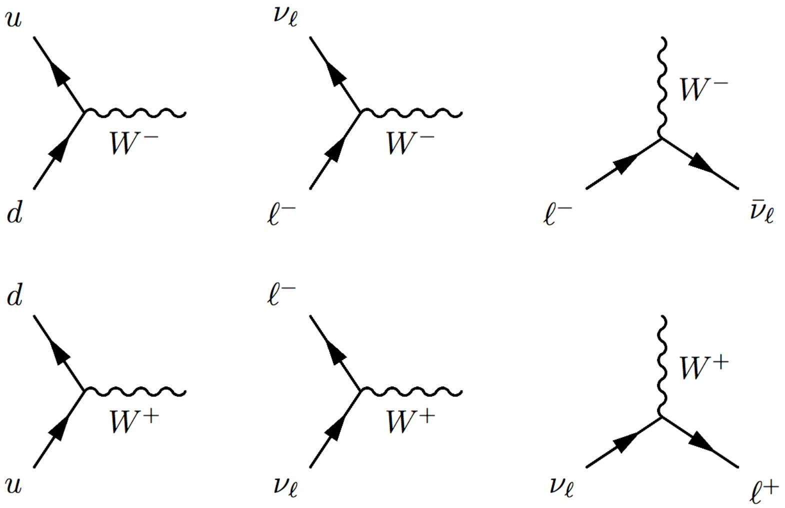

Figure 1.1: Examples of charged current, weak interaction vertices for both W^- (top) and W^+ (bottom). In the Feynman diagrams, $\ell = e$, μ, τ.

1.2 are the same as those in the electromagnetic interaction when replacing $Z^0 \to \gamma$ and working with particles that have electromagnetic charge. This is a consequence of the electroweak theory of Glashow, Weinberg and Salam, in which the Z^0 and γ are very closely related.

The strength of the weak interaction is described by the Fermi coupling constant, G_F, and is equal to

$$G_F = \frac{g^2}{4\sqrt{2}m_W^2}, \tag{1.5}$$

where $g \sim O(1)$ is the coupling constant of the $W^\pm$ bosons in the standard model (it is the weight of the vertices in Figure 1.1). Because the $W^\pm$ bosons are very massive, the Fermi coupling constant is small; the weak interaction is indeed weak. The decay of a muon, $\mu^- \to e^- + \nu_\mu + \bar{\nu}_e$, provides a means to determine the Fermi constant because the interaction of four leptons is more theoretically tractable than working with hadrons. The mean lifetime of a muon to decay is

$$\tau_\mu^{-1} = \frac{G_F^2 m_\mu^5}{192\pi^3} f(m_e/m_\mu), \tag{1.6}$$

where $f(x)$ is a well calculated function, $m_e/m_\mu \approx 0.004$, and corrections of the order

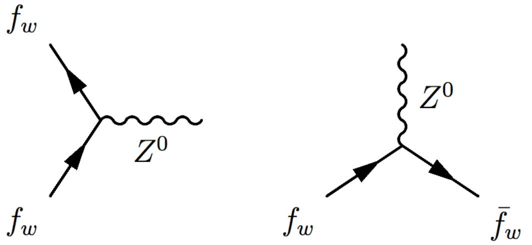

Figure 1.2: Examples of neutral current, weak interaction vertices. In the Feynman diagrams, f_w is any particle that interacts with the weak interaction.

$m_\mu^2/m_W^2 \sim 10^{-6}$ are neglected. Experiments have measured the Fermi constant to be [22]

$$G_F = 1.166\ 37 \pm 0.000\ 01 \times 10^{-11}\ \text{MeV}^{-2}. \tag{1.7}$$

Two important quantities in the discussion of the evolution of neutrinos in the early universe are the forward scattering potential and the scattering rate resulting from weak interactions with thermal populations of particles. For example, as a photon travels through a material, it attains a self-energy from its electromagnetic interactions with the electrons in the material. This alters the dispersion relation of the photons, acting as an index of refraction; the real part acts as an effective mass (due to the forward scattering potential) and the imaginary part reflects the scattering rate. Similarly, as a neutrino travels through a medium with weak charge, it gains a self-energy that can also act as an index of refraction [26]. Figure 1.3 shows the Feynman diagrams of the leading order contributions to the neutrino self energy.

The forward scattering potential for neutrino ν_α, $V(\nu_\alpha)$, can be separated into a number of additive categories, for neutrino scattering off:

- *neutrino background of a different flavor.* Evaluating the tadpole graph [Fig. 1.3(a)] for the neutral current forward scattering of ν_α off ν_β for $\beta \neq \alpha$ yields

  $$V_{\nu_\beta}(\nu_\alpha) = \pm\sqrt{2} G_F \left(n_{\nu_\beta} - n_{\bar{\nu}_\beta}\right), \tag{1.8}$$

  where the upper sign is for neutrinos and the lower sign is for antineutrinos.

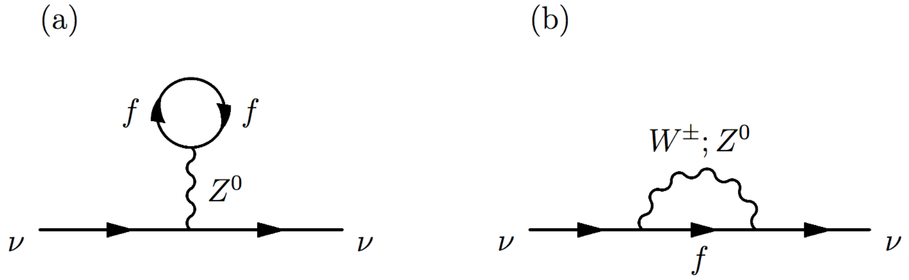

Figure 1.3: One loop thermal contributions to the neutrino self energy. (a) The tadpole graph includes neutral current scattering off any species in the early universe. (b) The bubble graph includes both neutral and charged current scattering off leptons with the same flavor as the neutrino.

- *neutrino background of the same flavor.* The forward scattering potential is calculated from both the tadpole and bubble graph [Fig. 1.3(b)]. In the tadpole graph, energy and momentum conservation constrains the four-momentum of the Z^0 boson to be zero, so that the propagator is simply $ig_{\mu\nu}/m_Z^2$. However, this is not the case with the bubble graph, so the full vector boson propagator is necessary. As long as the neutrino energy is small compared to the $W^{\pm}$ and Z^0 bosons, the propagator can be expanded in powers of m_Z^{-2} and the neutral current forward scattering potential is

$$V_{\nu_\alpha}(\nu_\alpha) = \pm 2\sqrt{2} G_F \left(n_{\nu_\alpha} - n_{\bar{\nu}_\alpha} \right) - \frac{8\sqrt{2} G_F p_\nu}{3 m_Z^2} \left(\langle E_{\nu_\alpha} \rangle n_{\nu_\alpha} + \langle E_{\bar{\nu}_\alpha} \rangle n_{\bar{\nu}_\alpha} \right). \quad (1.9)$$

- *background nucleons.* The neutral current forward scattering potential off neutrons and protons (and their antiparticles) is

$$V_{\mathrm{nuc}}(\nu_\alpha) = \mp \frac{G_F}{\sqrt{2}} \left(n_n - n_{\bar{n}} \right) \pm \frac{G_F}{\sqrt{2}} (1 - 4\sin^2\theta_W) \left(n_p - n_{\bar{p}} \right), \quad (1.10)$$

  where $\sin^2\theta_W = 0.231\ 19 \pm 0.000\ 14$ [22] is the Weinberg angle (or the weak angle) [9].

- *charged lepton background of a different flavor.* The neutral current forward scattering potential off charged leptons of a different flavor is

$$V_\beta(\nu_\alpha) = \mp\frac{G_F}{\sqrt{2}}(1 - 4\sin^2\theta_W)\,(n_{\beta^-} - n_{\beta^+})\,. \tag{1.11}$$

- *charged lepton background of the same flavor.* Forward scattering off charged leptons of the same flavor is a combination of both neutral and charged currents interactions,

$$V_\alpha(\nu_\alpha) = \pm\sqrt{2}G_F\,(n_{\alpha^-} - n_{\alpha^+}) - \frac{8\sqrt{2}G_F p_\nu}{3m_W^2}\,(\langle E_{\alpha^-}\rangle n_{\alpha^-} + \langle E_{\alpha^+}\rangle n_{\alpha^+})\,. \tag{1.12}$$

It is useful to write the forward scattering potential as $V = A + B + C$, where A is the neutrino-matter interaction term, B is the neutrino-neutrino interaction term, and C is called the "thermal" term, the lowest order correction to the A and B terms. In the early universe, charge neutrality implies that $n_{e^-} - n_{e^+} = n_p - n_{\bar{p}}$, and it is expected that $n_{\mu^-} - n_{\mu^+} \approx n_{\tau^-} - n_{\tau^+} \approx 0$. In this approximation, the A potential is

$$A(\nu_\alpha) = \sqrt{2}G_F\left[\delta_{\alpha e}(0.5 + 2\sin^2\theta_W)\,(n_{e^-} - n_{e^+}) - 0.5\,(n_n - n_{\bar{n}})\right], \tag{1.13}$$

and the B potential is

$$B(\nu_\alpha) = \sqrt{2}G_F\left[(n_{\nu_\alpha} - n_{\bar{\nu}_\alpha}) + \sum_{\beta=e,\mu,\tau}\left(n_{\nu_\beta} - n_{\bar{\nu}_\beta}\right)\right]. \tag{1.14}$$

The C potential is

$$C(\nu_\alpha) = -\frac{8\sqrt{2}G_F p_\nu}{3m_Z^2}\,(\rho_{\nu_\alpha} + \rho_{\bar{\nu}_\alpha}) - \frac{8\sqrt{2}G_F p_\nu}{3m_W^2}\,(\rho_{\alpha^-} + \rho_{\alpha^+})\,, \tag{1.15}$$

where ρ_i is the total energy density in species i. Assuming the background particles are in thermal equilibrium [see, *e.g.*, Equation (1.80)] and neglecting particle chemical potentials,

$$C(\nu_\alpha) = -\frac{14\pi}{45}\sin^2\theta_W\alpha^{-1}G_F^2 p_\nu T^4\left(\cos^2\theta_W + 2\right), \tag{1.16}$$

where $\alpha^{-1} = 137.035\ 999\ 679(94)$ [22] is the fine structure constant. The first term is relevant for all neutrinos, while the second term is only included when the charged lepton of the same flavor has an ultra-relativistic thermal population.

In general, there may be a flavor off-diagonal term in the neutrino-neutrino forward scattering potential which can be calculated from the bubble graph with an incoming neutrino of one flavor and outgoing neutrino of another flavor, interacting through the neutral current with $f \in \{\nu_1, \nu_2, \nu_3\}$. If the number densities of all three flavors of neutrinos are equal, then the off-diagonal forward scattering potential is GIM suppressed. Otherwise, the neutrino-neutrino off-diagonal forward scattering potential must be calculated and included self-consistently in any calculation [27, 28].

Similarly, the total scattering rate can be deduced from a number of additive categories, assuming all ultra-relativistic thermally populated particles share a common temperature and do not have significant particle-antiparticle asymmetries (no chemical potentials), for neutrino scattering off:

- *other neutrinos.* Assuming that all three neutrino flavors are in thermal equilibrium, the total neutrino-neutrino scattering rate is

  $$\Gamma_\nu(\nu_\alpha) \approx \frac{7\pi}{27} p_\nu G_F^2 T^4. \tag{1.17}$$

- *charged leptons and antileptons.* Any charged lepton that is ultra-relativistic and in thermal equilibrium in the early universe will contribute to the total scattering rate

  $$\Gamma_\beta(\nu_\alpha) \approx \left[\left(-(-1)^{\delta_{\alpha\beta}} 0.5 + \sin^2\theta_W\right)^2 + \sin^4\theta_W\right] \frac{7\pi}{27} p_\nu G_F^2 T^4, \tag{1.18}$$

  while any charged lepton that is no longer ultra-relativistic will contribute a negligible amount to the total scattering rate.

As will be discussed in the next section, chiral symmetry is restored in the early universe for $T > T^{\mathrm{c}}_{\mathrm{QCD}} \sim 170$ MeV, so at these high temperatures, the universe is filled with a quark-gluon plasma, instead of a photon-baryon plasma. For $T \lesssim T^{\mathrm{c}}_{\mathrm{QCD}}$, the baryons are non-relativistic and will have a minimal effect on the total scattering rate. However, for $T \gtrsim T^{\mathrm{c}}_{\mathrm{QCD}}$, free quarks will thermally populate the universe. The bare quark-neutrino interaction remains an active area of research [29, 30].

1.1.2 Neutrino Mixing and Sterile Neutrinos

In the Glashow-Weinberg-Salam standard model, particle masses are generated by the Higgs mechanism. Yukawa couplings between particles and the Higgs field result in particles having mass. However, there is no a priori reason that the Higgs ought to interact with the particle fields in the same manner as the weak interaction's gauge bosons. Thus, in general, it is expected that the weak eigenstates are not coincident with the mass eigenstates (eigenstates of the Higgs interaction).

In the quark sector, the CKM matrix describes this inconsistency between weak and mass eigenstates, and is responsible for flavor changing charged currents. Now, if neutrinos also have mass, then the weak states and the mass states may be related in a similar manner,

$$|\nu_\alpha\rangle = \sum_i U^*_{\alpha i}|\nu_i\rangle, \tag{1.19}$$

where ν_α are the weak (flavor) states, ν_i are mass states, $U_{\alpha i}$ are the elements of the Maki-Nakagawa-Sakata (MNS) unitary transformation, and the indices $\alpha = e,\ \mu,\ \tau$ and $i = 1, 2, 3$.

The MNS neutrino mixing matrix is a 3×3 unitary matrix, which can be parametrized by three mixing angles one phase. In terms of these three mixing angles (θ_{12}, θ_{23}, θ_{13}) and the CP-violating phase, δ, the mixing matrix may be written as

$$\begin{aligned} U &= \begin{pmatrix} 1 & 0 & 0 \\ 0 & c_{23} & s_{23} \\ 0 & -s_{23} & c_{23} \end{pmatrix} \begin{pmatrix} c_{13} & 0 & s_{13}e^{-i\delta} \\ 0 & 1 & 0 \\ -s_{13}e^{i\delta} & 0 & c_{13} \end{pmatrix} \begin{pmatrix} c_{12} & s_{12} & 0 \\ -s_{12} & c_{12} & 0 \\ 0 & 0 & 1 \end{pmatrix} \\ &= \begin{pmatrix} c_{12}c_{13} & s_{12}c_{13} & s_{13}e^{-i\delta} \\ -s_{12}c_{23} - c_{12}s_{23}s_{13}e^{i\delta} & c_{12}c_{23} - s_{12}s_{23}s_{13}e^{i\delta} & s_{23}c_{13} \\ s_{12}s_{23} - c_{12}c_{23}s_{13}e^{i\delta} & -c_{12}s_{23} - s_{12}c_{23}s_{13}e^{i\delta} & c_{23}c_{13} \end{pmatrix}, \end{aligned} \tag{1.20}$$

where $s_{ij} = \sin\theta_{ij}$ and $c_{ij} = \cos\theta_{ij}$.

What is the significance of the CP-violating phase? The CP-transformation takes particles into antiparticles and vice versa, so the CP-violating phase ought

Table 1.1: Experimental best-fit values for neutrino mass and mixing parameters using a global analysis of data including solar, atmospheric, reactor and accelerator experiments [31].

δm^2_{21}	$7.65^{+0.23}_{-0.20} \times 10^{-5}$ eV^2
$\lvert\delta m^2_{31}\rvert$	$2.40^{+0.12}_{-0.11} \times 10^{-3}$ eV^2
$\sin^2\theta_{12}$	$0.304^{+0.022}_{-0.016}$
$\sin^2\theta_{23}$	$0.50^{+0.07}_{-0.06}$
$\sin^2\theta_{13}$	< 0.040 (2σ limit)

to describe any differences between neutrinos and antineutrinos. Taking the CP-transformation of Equation (1.19) yields the mixing for antineutrinos

$$|\bar{\nu}_\alpha\rangle = \sum_i U_{\alpha i}|\bar{\nu}_i\rangle. \tag{1.21}$$

The difference between the two linear transformations is a complex conjugation. Looking at the dependence on δ of the MNS matrix, if δ is an integral multiple of π then CP is conserved, otherwise δ gives a measure of the violation of CP-symmetry.

Experiments using neutrino detectors in mines have been successful in constraining a number of neutrino mass and mixing parameters. Experimental measurements of the oscillations of neutrinos produced in the atmosphere, nuclear reactors, and particle accelerators along with measurements of neutrino flavor transformation of solar neutrinos have combined to measure two of the three mixing angles and constrain the third mixing angle, θ_{13}. These experiments have also measured the difference in the square of the mass eigenvalues, $\delta m^2_{ij} = m^2_i - m^2_j$. Table 1.1 summarizes the best-fit values of these neutrino mass and mixing parameters, analyzing the data from all of the neutrino experiments.

While significant progress has been made in determining the neutrino mass and mixing parameters, there remains a number of unanswered questions. The mixing angle θ_{13} is constrained to be small but has not been measured, and the CP-violating phase, δ, remains unconstrained since θ_{13} is small. While the two independent mass squared differences are measured, there is no measurement of the absolute mass scale

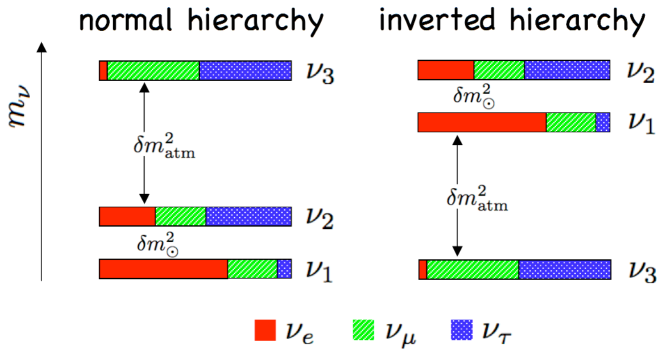

Figure 1.4: The neutrino mass hierarchy for the normal mass hierarchy on the left and the inverted mass hierarchy on the right. Also indicated are the approximate relationship between the mass and flavor states.

and no determination of the mass hierarchy (*i.e.*, the sign of δm^2_{31}). There are two scenarios when discussing the neutrino mass hierarchy as shown in Figure 1.4, the normal mass hierarchy where there are two light neutrinos and a heavier neutrino, and the inverted mass hierarchy where there are two heavy neutrinos and one lighter neutrino.

Terrestrial experiments continue to search for θ_{13}, with hopes of also uncovering the neutrino mass hierarchy and the CP-violating phase [32]. Other experiments are attempting to measure neutrinoless double β-decay or the end-point energy of the β-decay of tritium to deduce the absolute mass scale of the neutrinos [33, 34]. It is possible that astrophysics may be just as successful in uncovering the remaining parameters as any terrestrial experiment. The combined analysis of the cosmic microwave background radiation, the luminosity distance to type Ia supernovae, and baryon acoustic oscillations has provided an upper limit on the sum of the neutrino masses, $\sum m_\nu < 0.67$ eV [35], which is a more stringent constraint than any laboratory experiment. Finally, if a galactic supernova is observed by the neutrino detectors around the world, its temporal and energy spectrum could lead to a measurement of both θ_{13} and the neutrino mass hierarchy [36, 37].

The Liquid Scintillator Neutrino Detector experiment at Los Alamos National Laboratory, observed neutrino oscillations in a neutrino beam created by a particle accelerator. In 2000, the LSND collaboration released results that suggested $\delta m^2 \sim 1$ eV^2 [38]. If there were only three neutrino states, then only two independent mass squared differences would be expected. So, the introduction of a third independent mass squared difference would imply the existence of a fourth neutrino. Since the measurement of Z^0 decay has eliminated the possibility of a fourth active neutrino, the interpretation would be that this fourth neutrino would be a sterile neutrino. A sterile neutrino is a theoretical type of neutrino that has weaker than weak interactions. The results of the LSND experiment have since been refuted by the mini-BOONE experiment [39], but the idea of the existence of a sterile neutrino remains an attractive one to theorists.

If neutrinos were massless, then left-handed chirality states (those that the weak interaction acts upon) would be equivalent to left-handed helicity states (spin and momentum of the neutrino are anti-parallel). However, since neutrinos are massive, a left-handed chirality state is a linear superposition of left- and right-handed helicity states. For massive particles, chirality is a relativistic invariant while helicity is not. It is simple to see that helicity is not relativistically invariant. Suppose we have a particle with left-handed helicity, its spin and momentum are anti-parallel. Taking a suitable Lorentz boost will change the direction of the momentum while leaving the spin unchaged. A left-handed helicity state in one frame can be a right-handed helicity state in another frame.

What happens to the orthogonal combination of left- and right-handed helicity states? It has been argued that this naturally leads to the introduction of right-handed chirality states into the standard model. Many extensions to the standard model include a right-handed neutrino which, since the weak interaction current is left-handed, has no weak interactions. These sterile neutrinos would be irrelevant unless they coupled to the weak sector. The symmetries of the models allow sterile neutrinos to mix with active neutrinos through mass terms (Yukawa coupling to the Higgs field), while some models couple the sterile neutrinos to the active neutrinos by introducing scalar fields [40–43]. In this disssertation, active-sterile neutrino mixing is considered solely through a mass term.

If sterile neutrinos have vacuum mixing with active neutrinos, then sterile neutrinos will experience the weak interaction, albeit at a much weaker level. Consider active-sterile neutrino vacuum mixing with just one active and one sterile neutrino (hence, parametrized by a mixing angle θ), then the strength of the weak interaction is $\sim G_F^2 \sin^2\theta$. Measurements of the Z^0 decay width constrain $\sin^2\theta$ to be very small.

The sterile neutrino was first proposed by Pontecorvo in the discussion of mass in the neutrino sector [44]. Sterile neutrinos have been proposed to solve a number of outstanding problems in astrophysics. The emission of sterile neutrinos in a preferred direction during a supernova could be responsible for pulsar kicks, resulting in some pulsars having large peculiar velocities [41, 45]. Active-sterile neutrino oscillation may help to take energy out of the core of a supernova, reinvigorating the shock wave by depositing this energy in it [46, 47]. Some models of dark energy involve the decay of a sterile neutrino [48], while there are many models that suggest sterile neutrinos as a dark matter particle [49–51], including in Chapter 3 of this dissertation.

Since sterile neutrinos have nonzero weak interactions, they can be created in the early universe. One of the attractive qualities of sterile neutrino dark matter is that it is not as dark as it ought to be. A sterile neutrino may decay into a lighter neutrino and a photon. In the rest frame, this sends the photon with an energy of half the sterile neutrino mass. The decay rate for $\nu_s \rightarrow \nu_\alpha + \gamma$ is very small,

$$\Gamma \approx 6.8 \times 10^{-33}\ \mathrm{s}^{-1} \left(\frac{sin^2 2\theta}{10^{-10}}\right)\left(\frac{m_s}{1\ \mathrm{keV}}\right)^5, \tag{1.22}$$

and is highly sensitive to the mass of the sterile neutrino. However, if sterile neutrinos comprise the dark matter, then there are a lot of sterile neutrinos in the universe, so that their decay may be observable in a galaxy cluster where there is a lot of dark matter sitting in its potential well. This allows astrophysics to constrain sterile neutrino parameters that could not be probed in the terrestrial laboratory.

1.1.3 Neutrino Oscillations

The quantum mechanical consequence of neutrino mixing as in Equation (1.19) is that neutrino flavors will oscillate. For simplicity, we begin with 2 × 2 neutrino mixing, say between ν_μ and ν_τ. A 2×2 unitary transformation is parametrized by one mixing angle θ, so that the relationship between the flavor states and the mass states is

$$\begin{aligned}|\nu_\mu\rangle &= \cos\theta|\nu_1\rangle + \sin\theta|\nu_2\rangle \\ |\nu_\tau\rangle &= -\sin\theta|\nu_1\rangle + \cos\theta|\nu_2\rangle. \end{aligned} \tag{1.23}$$

In vacuum, the mass eigenstates satisfy

$$\hat{\mathcal{H}}_v|\nu_k\rangle = E_k|\nu_k\rangle, \tag{1.24}$$

for the vacuum Hamiltonian $\mathcal{H}_v$, where $E_k = \sqrt{p_\nu^2 + m_k^2}$ is the energy-momentum dispersion relation. If at $t = 0$, the neutrino is created in state $|\nu_\mu\rangle$, then using the time evolution operator, $\hat{\mathcal{U}}(t) = e^{-i\hat{\mathcal{H}}_v t}$, at a later the time the wavefunction of the neutrino is

$$|\nu(t)\rangle = \cos\theta\, e^{-iE_1 t}|\nu_1\rangle + \sin\theta\, e^{-iE_2 t}|\nu_2\rangle. \tag{1.25}$$

Assuming that the neutrino is ultra-relativistic, $p_\nu \gg m_k$, then

$$E_2 - E_1 \approx \frac{\delta m^2}{2E_\nu}, \tag{1.26}$$

where $p_\nu \approx E_\nu$ and $\delta m^2 = m_2^2 - m_1^2$.

The probability that the neutrino will be measured in state ν_τ at a time t, when the neutrino has traveled a distance $L \approx t$, is

$$\mathcal{P}_{\nu_\mu \to \nu_\tau}(L) = \sin^2 2\theta \sin^2\left(\frac{\delta m^2 L}{4E_\nu}\right) \equiv \sin^2 2\theta \sin^2\left(2\pi\frac{L}{\ell_v}\right), \tag{1.27}$$

where the vacuum neutrino oscillation length is

$$\ell_v = \frac{4\pi E_\nu}{\delta m^2} \approx 1000 \text{ km} \left(\frac{E_\nu}{1\text{GeV}}\right)\left(\frac{\delta m^2}{2.5 \times 10^{-3} \text{ eV}^2}\right)^{-1}. \tag{1.28}$$

On the other hand, the probability that the neutrino is measured in state ν_μ is the complement,

$$\mathcal{P}_{\nu_\mu \to \nu_\mu}(L) = 1 - \sin^2 2\theta \sin^2\left(\frac{\delta m^2 L}{4E_\nu}\right). \tag{1.29}$$

The atmospheric neutrino anomaly is the result of neutrino oscillations. Atmospheric neutrinos are created by cosmic rays hitting the atmosphere, creating pions, which in turn decay to ν_μ and ν_e in reactions (1.3). The result is that twice as many muon neutrinos and antineutrinos are created than electron neutrinos and antineutrinos. However, the measurement of this ratio was approximately 60% of the expected value [21]. Neutrinos are created in this process with energies $E_\nu \sim 100$ MeV to ~ 100 GeV, which correspond to oscillations lengths of $\ell_v \sim 100$ km to $\sim 100,000$ km when using $\delta m^2 \approx \delta m^2_{31}$. Atmospheric neutrinos travel anywhere from about 20 km for neutrinos created in the atmosphere at the zenith of the neutrino detector site to about $13,000$ km for neutrinos created in the atmosphere at the nadir, on the other side of the planet. Since the path length is of order the neutrino oscillation length, atmospheric neutrinos are well suited for probing neutrino oscillations with $\delta m^2 \sim \delta m^2_{31}$. This mass squared difference is often referred to as the atmospheric mass splitting, $\delta m^2_{\mathrm{atm}} = \delta m^2_{31}$.

In general, 3×3 neutrino mixing should be considered, as in Equation (1.19). The transition probability is

$$\begin{aligned}\mathcal{P}_{\nu_\alpha \to \nu_\beta} = \delta_{\alpha\beta} &- 4 \sum_{k>j} \Re\left[U^*_{\alpha k} U_{\beta k} U_{\alpha j} U^*_{\beta j}\right] \sin^2\left(\frac{\delta m^2_{kj} L}{4E_\nu}\right) \\ &+ 2 \sum_{k>j} \Im\left[U^*_{\alpha k} U_{\beta k} U_{\alpha j} U^*_{\beta j}\right] \sin\left(\frac{\delta m^2_{kj} L}{2E_\nu}\right). \qquad (1.30)\end{aligned}$$

The final term indicates that it is possible for neutrino oscillation experiments to determine the neutrino hierarchy (*i.e.*, the sign of δm^2_{31}).

1.1.4 The MSW Effect

In the previous section the evolution of the weak states in vacuum was discussed. However, whenever a neutrino travels through a medium with weak charge, its evolution is altered by forward scattering, just as a photon traveling through a medium with electric charge has its evolution altered by forward scattering. For simplicity, consider 2×2 neutrino mixing between ν_e and $\nu_x \approx (\nu_\mu + \nu_\tau)/\sqrt{2}$, and a forward scattering potential that has no off-diagonal terms. The total Hamiltonian is the sum of the vacuum Hamiltonian and the diagonal forward scattering potential $\hat{\mathcal{H}}_m$,

$$\hat{\mathcal{H}}_m|\nu_\alpha\rangle = V_\alpha|\nu_\alpha\rangle, \tag{1.31}$$

where $V_x \approx (V_\mu + V_\tau)/2$. Using the one-parameter 2×2 mixing scheme in Equation (1.23) with the substitutions $\mu \rightarrow e$ and $\tau \rightarrow x$, the Hamiltonian written in the $(\nu_e \;\; \nu_x)$ basis is

$$\begin{aligned}\hat{\mathcal{H}}_f = \left(E_\nu + \frac{m_1^2 + m_2^2}{4E_\nu} + \frac{V_e + V_x}{2}\right)\hat{\mathbf{I}} + \frac{\delta m^2}{4E_\nu}\begin{pmatrix} -\cos 2\theta & \sin 2\theta \\ \sin 2\theta & \cos 2\theta \end{pmatrix} \\ + \frac{\Delta V}{2}\begin{pmatrix} 1 & 0 \\ 0 & -1 \end{pmatrix},\end{aligned} \tag{1.32}$$

where $\Delta V \equiv V_e - V_x$, and $\hat{\mathbf{I}}$ is the identity matrix.

The Schrödinger equation can be written in the flavor basis after the flavor states are multiplied by a suitable phase factor to remove the trace of $\mathcal{H}_f$,

$$i\frac{\partial}{\partial t}\begin{pmatrix} \nu_e \\ \nu_x \end{pmatrix} = \left[\frac{\delta m^2}{4E_\nu}\begin{pmatrix} -\cos 2\theta & \sin 2\theta \\ \sin 2\theta & \cos 2\theta \end{pmatrix} + \frac{\Delta V}{2}\begin{pmatrix} 1 & 0 \\ 0 & -1 \end{pmatrix}\right]\begin{pmatrix} \nu_e \\ \nu_x \end{pmatrix}. \tag{1.33}$$

In the usual quantum mechanical practice, the Hamiltonian is diagonalized to determine the mass (energy) states. The one-parameter unitary transformation [*e.g.*, Equation (1.23)] with effective matter mixing angle θ_M,

$$\tan 2\theta_M = \tan 2\theta \left(1 - \frac{2E_\nu \Delta V}{\delta m^2 \cos 2\theta}\right)^{-1}, \tag{1.34}$$

diagonalizes the Hamiltonian in the mass basis,

$$i\frac{\partial}{\partial t}\begin{pmatrix} \nu_1^M \\ \nu_2^M \end{pmatrix} = \frac{\delta m^2_{\text{eff}}}{4E_\nu}\begin{pmatrix} -1 & 0 \\ 0 & 1 \end{pmatrix}\begin{pmatrix} \nu_1^M \\ \nu_2^M \end{pmatrix}, \tag{1.35}$$

where the effective mass squared difference is

$$\delta m^2_{\text{eff}} = \sqrt{\left(\delta m^2 \cos 2\theta - 2E_\nu \Delta V\right)^2 + \left(\delta m^2 \sin 2\theta\right)^2}, \tag{1.36}$$

with the tacet assumption that $\delta m^2 > 0$ (the mixing angle is fixed so that this assumption is realized) .

By analogy, the matter-affected neutrino oscillation probabilities are

$$\mathcal{P}_{\nu_e \to \nu_x} = \sin^2 2\theta_M \sin^2 \left(\frac{\delta m^2_{\text{eff}} L}{4E_\nu} \right), \tag{1.37}$$

and $\mathcal{P}_{\nu_e \to \nu_e} = 1 - \mathcal{P}_{\nu_e \to \nu_x}$. One important point to emphasize is that the oscillations are maximal when $\sin^2 2\theta_M = 1$, or $\delta m^2 \cos 2\theta = 2E_\nu \Delta V$. This resonance condition holds no matter how small the vacuum mixing angle is, and corresponds to a maximum in the oscillation length, $\ell_{M,\text{res}} = 4\pi E_\nu / (\delta m^2 \sin 2\theta)$.

As a neutrino travels through a medium, the forward scattering potential that it experiences changes in time $\Delta V \to \Delta V(t)$. Hence, the mass states that are found by diagonalizing the Hamiltonian are only instantaneous energy eigenstates, and the flavor states may be written in terms of these instantaneous energy eigenstates,

$$\begin{aligned} |\nu_e\rangle &= \cos\theta_M(t) |\nu_1^M(t)\rangle + \sin\theta_M(t) |\nu_2^M(t)\rangle \\ |\nu_x\rangle &= -\sin\theta_M(t) |\nu_1^M(t)\rangle + \cos\theta_M(t) |\nu_2^M(t)\rangle. \end{aligned} \tag{1.38}$$

The Schrödinger equation, written for a wavefunction in this instantaneous mass basis, $|\psi(t)\rangle = a_1(t)|\nu_1^M(t)\rangle + a_2(t)|\nu_2^M(t)\rangle$, is

$$i \frac{\partial}{\partial t} \begin{pmatrix} a_1 \\ a_2 \end{pmatrix} = \left[\frac{\delta m^2_{\text{eff}}}{4E_\nu} \begin{pmatrix} -1 & 0 \\ 0 & 1 \end{pmatrix} - \frac{d\theta_M(t)}{dt} \begin{pmatrix} 0 & i \\ -i & 0 \end{pmatrix} \right] \begin{pmatrix} a_1 \\ a_2 \end{pmatrix}. \tag{1.39}$$

If the off-diagonal terms in Equation (1.39) are small, then the evolution of the wave function is simple,

$$a_k(t) = a_k(0) \exp\left[-(-1)^k i \int_0^t \delta m^2_{\text{eff}}(\tau)/4E_\nu \, d\tau \right], \tag{1.40}$$

and the ν_e survival probability is

$$\begin{aligned} \mathcal{P}^{\text{ad}}_{\nu_e \to \nu_e}(t) = \frac{1}{2} &+ \frac{1}{2} \cos 2\theta_{M0} \cos 2\theta_M(t) \\ &+ \frac{1}{2} \sin 2\theta_{M0} \sin 2\theta_M(t) \cos\left(\int_0^t \frac{\delta m^2_{\text{eff}}(\tau)}{2E_\nu} \, d\tau \right), \end{aligned} \tag{1.41}$$

where $\theta_{M0} = \theta_M(t = 0)$. This is the solution in the adiabatic limit. That is, the off diagonal terms are small enough that the neutrino will remain in the same mass eigenstate that it was created in. In the survival probability, the lone phase, $\int \delta m^2_{\text{eff}}/2E_\nu \, d\tau$, is large so that small differences in neutrino energy result in large differences in the phase. Thus, in an energy interval in the far-field limit, the final term in Equation (1.41) averages to zero.

In astrophysical environments, neutrinos are typically created in a flavor state in a very dense environment, such as the core of a star or in the early universe, then stream toward lower densities. This means that $|\Delta V(t = 0)| \gg \delta m^2/E_\nu$. Thus, $\cos 2\theta_{M0} \approx -\text{sgn}\,[\Delta V]$. Typically, the forward scattering potential of electron neutrinos is larger than the forward scattering potential of other active neutrinos, especially in the core of a star, where the forward scattering potential is dominated by the number density of electrons. In this case, $\cos 2\theta_{M0} \approx -1$, and the asymptotic ν_e survival probability is

$$\mathcal{P}^{\text{ad}}_{\nu_e \to \nu_e} \approx \sin^2\theta. \tag{1.42}$$

The interpretation of this result is at the heart of adiabatic quantum mechanics. At $t = 0$, the neutrino is created in state ν_e in the dense environments described above with $\cos 2\theta_{M0} \approx -1$:

$$|\nu(t = 0)\rangle = |\nu_e\rangle \approx -|\nu_2^M(t = 0)\rangle. \tag{1.43}$$

As the neutrino travels, the off-diagonal terms of the Hamiltonian are small, so that the neutrino remains in its original state up to a phase, $|\nu(t)\rangle \approx e^{i\phi(t)}|\nu_2^M(t)\rangle$. This is the adiabatic approximation. Once the neutrino travels to where the forward scattering potential becomes negligible, the instantaneous mass states become the vacuum mass states and $|\nu(t \to \infty)\rangle \propto |\nu_2\rangle = \sin\theta|\nu_e\rangle + \cos\theta|\nu_x\rangle$. As a result, the ν_e survival probability is

$$\mathcal{P}^{\text{ad}}_{\nu_e \to \nu_e} = |\langle\nu_e|\nu(t \to \infty)\rangle|^2 \approx \sin^2\theta. \tag{1.44}$$

This adiabatic flavor transformation is known as the Mikhail-Smirnov-Wolfenstein (MSW) effect [52, 53].

Describing dimensionfull numbers as "small" is not useful, so the adiabaticity parameter is defined as the ratio of the diagonal terms to the off-diagonal terms of the Hamiltonian in Equation (1.39),

$$\gamma = \frac{\delta m^2_{\text{eff}}}{4E_\nu |d\theta_M/dt|} = \left(\frac{\delta m^2_{\text{eff}}}{2E_\nu}\right)^2 \frac{1}{\sin 2\theta_M |d(\Delta V)/dt|}. \tag{1.45}$$

When the adiabaticity parameter is large ($\gg 1$), the adiabatic solution presented above is successful in describing the neutrino flavor transformation dynamics. The adiabaticity parameter is minimized at the MSW resonance condition

$$2E_\nu \Delta V(t_{\text{res}}) = \delta m^2 \cos 2\theta, \tag{1.46}$$

where δm^2_{eff} is minimized and $\sin^2 2\theta_M$ is maximized. Thus, the minimal adiabaticity parameter is

$$\gamma_{\text{res}} = \frac{\delta m^2}{2E_\nu} \mathcal{D}_{\text{res}} \frac{\sin^2 2\theta}{\cos 2\theta}, \tag{1.47}$$

where $\mathcal{D} = |d \log(\Delta V)/dt|^{-1}$ is the density scale height.

There are two ways to heuristically understand the adiabaticity parameter. First, consider the physical width of the resonance, $\delta\ell$, as the distance the ultra-relativistic neutrino must travel in order to traverse the resonance. One way of describing this width is the physical width associated with the full width at half-maximum of the peaked function $\sin^2 2\theta_M(t)$,

$$\delta\ell \approx \left|\frac{d \log(\Delta V)}{dt}\right|^{-1} \frac{\delta(\Delta V)}{\Delta V} \approx 2\mathcal{D}_{\text{res}} \tan 2\theta. \tag{1.48}$$

The adiabaticity parameter at resonance is

$$\gamma_{\text{res}} \approx \pi \frac{\delta\ell}{\ell_{M,\text{res}}}, \tag{1.49}$$

the ratio of the width of the resonance to the neutrino oscillation length at resonance. This uses the basic idea of adiabaticity in quantum mechanics. If the quantum system is allowed to undergo many oscillations in the timescale at which the system is changing, then it will not transition into other energy states, although the energy eigenstates and eigenvalues may be changing in time. (Ref. [54] also discusses this relationship, however, note that there is a factor of two difference in the definition of the resonance width between this dissertation and Ref. [54]. However, this does not change the overall mathematics and the heuristic picture presented in both works.)

Another way to understand the adiabaticity parameter is to consider the difference in the energy eigenvalues at resonance, $\delta E_{\nu,\mathrm{res}} = \delta m^2 \sin 2\theta/(2E_\nu)$. Then, the adiabaticity parameter at resonance is

$$\gamma_{\mathrm{res}} \approx \delta\ell\, \delta E_{\nu,\mathrm{res}}/2. \tag{1.50}$$

This formulation of the adiabaticity parameter tempts one to think about the Heisenberg energy-time uncertainty relationship ($\Delta E\, \Delta t \gtrsim 1/2$). The neutrino remains in the resonance width for $\Delta t \sim \delta\ell$, so the quantum uncertainty in its energy is $\Delta E_H \sim 1/(2\delta\ell)$, and the adiabaticity parameter is $\gamma_{\mathrm{res}} \sim \delta E_{\nu,\mathrm{res}}/(4\Delta E_H)$. If the uncertainty in the energy is small compared to the energy gap between the two energy states, then transitions between energy states is suppressed, and the evolution is adiabatic.

When $\gamma_{\mathrm{res}} \lesssim 1$, the quantum mechanical evolution is not adiabatic and the evolution of both mass states, and the transitions between them, must be accounted for. The Parke formula follows the evolution of the neutrino in the instantaneous mass states, and performing the same average as above over large energy-dependent phases, the ν_e survival probability is

$$\mathcal{P}_{\nu_e\to\nu_e} = \frac{1}{2} + \left(\frac{1}{2} - P_c\right)\cos 2\theta_{M0}\cos 2\theta_M(t), \tag{1.51}$$

where P_c is the $\nu_1^M \rightleftharpoons \nu_2^M$ crossing probability at resonance [55]. As was the case above, in an astrophysical environment, when $\cos 2\theta_{M0} = -1$, the asymptotic ν_e survival probability is

$$\mathcal{P}_{\nu_e\to\nu_e} = (1 - P_c)\sin^2\theta + P_c\cos^2\theta. \tag{1.52}$$

What remains is to determine P_c, which ought to depend of γ_{res}. One common ansatz for the crossing probability is the Landau-Zener level crossing probability [56, 57],

$$P_{c,\mathrm{LZ}} = e^{-\pi\gamma_{\mathrm{res}}/2}. \tag{1.53}$$

The Landau-Zener crossing probability is predicated on the assumption that the forward scattering potential is linear, and extends indefinitely. While it is unphysical for a linear forward scattering potential to extends from $+\infty$ to $-\infty$, it remains a useful approximation since the forward scattering potential is often at least locally linear near the MSW resonance. Ref. [58] presents an analytic derivation of the Landau-Zener crossing probability and shows that when the evolution is non-adiabatic, corrections due to the finite size of the regime in question become significant. Work has been done to determine P_c for more general profiles of $\Delta V(t)$ and to consider the corrections to the Landau-Zener crossing probability in extreme non-adiabatic conditions [59].

In the sun, $\Delta V(t) = \sqrt{2}G_F n_e(t)$. When electron neutrinos are created in the core of the sun by the weak reactions in the nuclear fusion chain reaction, the high density of electrons in the core means that ν_e is most closely associated with ν_2^M. The charged current interactions between electrons and electron neutrinos (which are absent with μ or τ neutrinos) add to the effective mass of the ν_e so that it is effectively the heavier mass state. As the neutrinos freely stream from the core of the sun toward Earth, they experience an MSW resonance and ν_2^M transforms into ν_1^M with probability P_c. Thus, when the neutrinos reach earth, a fraction P_c of them are in mass state ν_1^M and $(1 - P_c)$ are in mass state ν_2^M, so that the total fraction of neutrinos measured as electron neutrinos is $P_c \cos^2\theta + (1 - P_c)\sin^2\theta < 1$. This deficit is the solar neutrino problem, which can be theoretically explained by considering the MSW effect and experimentally confirmed by detecting all the neutrino flavors that the initial ν_e were transformed into.

There is one sticking point in the discussion of neutrino mixing presented here. For oscillations in and out of matter, the Schrödinger equation was used with a relativistic kinetic energy. The Schrödinger equation is used in non-relativistic quantum mechanics, but the neutrinos are ultra-relativistic. It is ironic that since neutrinos are so very ultra-relativistic, the Schrödinger equation is effective in describing the evolution. Neutrino oscillations and the MSW effect are the result of quantum interference and hence depends on the evolution of the phase of the quantum states.

Treating neutrinos relativistically using the Dirac equation yields the same results as presented above [60].

1.1.5 The Quantum Kinetic Equations

Until now the coherent quantum mechanical evolution of neutrino states has been discussed. However, in some environments the density and temperature are large enough that neutrinos may scatter off a background of particles (and other neutrinos) making the decoherent evolution of neutrino states an interesting field to study. Astrophysical environments when the decoherent evolution of neutrinos is important include the dense cores of supernovae and the hot, dense plasma of the early universe.

The quantum kinetic equations (QKEs) are a set of nonlinear, integro-partial differential equations that describe the evolution of the single particle density matrix,

$$\rho = \sum_{\alpha\beta} \rho_{\alpha\beta} |\nu_\alpha\rangle\langle\nu_\beta|, \tag{1.54}$$

where the sum is over all relevant flavor states in the problem. The evolution of the N-particle density matrix, $\rho^{(N)} = \prod_i \otimes \rho_i$, is governed by the S matrix,

$$\rho^{(N)}(t_0 + \Delta t) = \hat{S}(\Delta t) \rho^{(N)}(t_0) \hat{S}^\dagger(\Delta t). \tag{1.55}$$

The QKEs are a mean field theory, so a single density operator is assumed to describe the evolution of each neutrino state, and the degrees of freedom of all but one neutrino are integrated out [61, 62]. The density operator is a Hermitian operator, so it can be described as the real linear combination of the generators of $SU(N)$, for N neutrinos, and the identity,

$$\rho = P_0 \left(\hat{\mathbf{I}}_N + \mathbf{P} \cdot \boldsymbol{\sigma}_N \right), \tag{1.56}$$

where $\boldsymbol{\sigma}_N$ are the $N^2 - 1$ generators of $SU(N)$ (for $N = 2$ they are the Pauli matrices and $N = 3$ they are the Gell-Mann matrices), P_0 is an overall normalization factor proportional to the total number of neutrinos, and $\mathbf{P}$ is a polarization vector that describes the occupation number of the neutrinos and the coherences between them.

There are two distinct components of the polarization vector: $\mathbf{P}_{\parallel}$, which describes the terms on the diagonal, corresponding to the occupation numbers (for $N = 2$, this is the $\hat{x}_3$ direction, while for $N = 3$, this is the $\hat{x}_3$ and $\hat{x}_8$ directions), and the directions perpendicular to this, $\mathbf{P}_{\perp}$, which describe the off-diagonal terms, corresponding to the quantum coherences.

In general, the quantum kinetic equations have three components that describe the evolution of $\mathbf{P}$: a term that deals with the coherent neutrino mixing and matter enhanced effects, a term that repopulates the occupation probabilities, and a term that dampens quantum coherences as a result of inelastic scattering. Generically, the QKEs look like

$$\frac{d\mathbf{P}}{dt} = \mathbf{V} \times \mathbf{P} + (\text{repopulating } \mathbf{P}_{\parallel}) - (\text{damping } \mathbf{P}_{\perp}),$$

where the generalization of the cross product to N-dimensions is $(\mathbf{V} \times \mathbf{P})_i = f_{ijk} V_j P_k$, where f_{ijk} are the structure constants of $SU(N)$, can be used to describe neutrino oscillations and the MSW effect in the coherent limit.

Chapter 3 discusses solutions of the quantum kinetic equations with two neutrinos in the early universe. While the assumptions of homogeneity and isotropy in the early universe and of near thermal equilibrium among active species can simplify the calculation of the relevant elements of the QKEs [63], the solution of the QKEs remains a computationally intensive process. There are a number of pitfalls when solving the QKEs to describe neutrino evolution in an environment where decoherence affects the quantum dynamics. First, the number of independent nonlinear integro-partial differential equations scale as N^2, so dealing with more than two neutrinos becomes overwhelming. Perhaps the biggest deterrent to solving the QKEs is that neutrino oscillations create high-frequency oscillations which make numerical solutions difficult and time consuming. One strategy that has been used to circumvent these problems is to approach the problem with a Boltzmann-like equation for the distribution functions (or equivalently the occupation numbers) [50, 63].

In Chapter 3, two neutrino mixing between an active neutrino and a sterile neutrino is considered, exploring how decoherence can serve to populate the sterile neutrino states by scattering out of active neutrino states. It is common to use a Boltzmann-like equation to explore this process,

$$\frac{Df_s(E,t)}{Dt} = \Gamma(\nu_\alpha \to \nu_s)\left(f_\alpha(E,t) - f_s(E,t)\right), \tag{1.57}$$

where D/Dt is the usual convective derivative and $\Gamma(\nu_\alpha \to \nu_s)$ is the scattering rate of ν_α to ν_s. Jpw can one understand this scattering rate? A weak interaction fixes the neutrino in active state ν_α. The neutrino then travels approximately its mean free path before interacting again with a background particle. As the neutrino travels without inelastically scattering, it oscillates between ν_α and ν_s. When the neutrino once again interacts, it now has a probability of being in state ν_s, because of neutrino oscillations. The neutrino state either scatters from ν_α into ν_s or remains as ν_α, but its oscillations begin anew.

Naively, it would seem that a higher scattering rate would result in a higher production rate of ν_s from ν_α. However, the scattering rate of $\nu_\alpha \to \nu_s$ is proportional to $\Gamma_\alpha \sin^2(2\pi\tau/\ell_M)$, where Γ_α is the scattering rate of ν_α with the background particles, and $\tau \lesssim 1/\Gamma_\alpha$ is the time between scatterings. So, as the scattering rate becomes large compared to the in-matter oscillation length, the $\nu_\alpha \to \nu_s$ scattering rate is proportional to Γ_α^{-1}. This is the quantum Zeno effect. When dealing with a quantum system with discrete energy levels, observing the system too often will suppress transitions between the energy levels [64].

Careful analysis of this problem has shown that this picture can provide a consistent picture of $\nu_\alpha \to \nu_s$ scattering if the “measurement rate” is one half of the total scattering rate. The effective $\nu_\alpha \to \nu_s$ scattering rate is

$$\Gamma(\nu_\alpha \to \nu_s) \approx \frac{\Gamma_\alpha}{2}\langle \mathcal{P}_{\nu_\alpha \to \nu_s}\rangle, \tag{1.58}$$

where $\langle \mathcal{P}_{\nu_\alpha \to \nu_s}\rangle$ is the ensemble-averaged probability that the neutrino collapses into the sterile state,

$$\langle \mathcal{P}_{\nu_\alpha \to \nu_s}\rangle = \left\langle \sin^2 2\theta_M(t) \sin^2 \frac{2\pi\tau}{\ell_M} \right\rangle, \tag{1.59}$$

where t is the absolute time scale, and τ is the time since the neutrino state was last observed. If the rate at which neutrinos are observed is $\Gamma_\alpha/2$, then the probability that a neutrino is unobserved after a time interval τ is $e^{-\Gamma_\alpha \tau/2}$. Assuming that $\sin^2 2\theta_M$ does not change significantly on a time scale Γ_α^{-1}, then

$$\langle \mathcal{P}_{\nu_\alpha \to \nu_s} \rangle = \sin^2 2\theta_M \left\langle \sin^2 \frac{2\pi\tau}{\ell_M} \right\rangle = \sin^2 2\theta_M(t) \frac{\int_0^{\tau' \gg \Gamma_\alpha^{-1}} e^{-\Gamma_\alpha(t)\tau/2} \sin^2 \frac{2\pi\tau}{\ell_M(t)}\, d\tau}{\int_0^{\tau' \gg \Gamma_\alpha^{-1}} e^{-\Gamma_\alpha(t)\tau/2}\, d\tau}. \tag{1.60}$$

If the total scattering rate and the neutrino oscillation length in medium also do not appreciably change on timescales of Γ_α^{-1}, then the $\nu_\alpha \to \nu_s$ scattering rate is

$$\Gamma(\nu_\alpha \to \nu_s) \approx \frac{\Gamma_\alpha}{4} \sin^2 2\theta_M \frac{1}{1 + \frac{1}{64\pi^2}\Gamma_\alpha^2 \ell_M^2}. \tag{1.61}$$

This is referred to as the quantum Zeno ansatz [65]. It must be noted that the scattering rate presented here differs in form the scattering rate presented in Equation (3.20). The difference manifests itself in a factor of 4π in the definition of the neutrino oscillation length. The form presented here remains consistent with the rest of the introduction. In Chapter 3, the quantum Zeno ansatz is compared to a solution of the quantum kinetic equations and it is found that the quantum Zeno ansatz is a successful approximation of the decoherent evolution of the neutrino states. Figure 3.7 compares the two solutions. As expected, the quantum Zeno ansatz works better far away from resonances ($\sin^2 2\theta_M$ and ℓ_M are peaked functions at these resonances) than near to the resonances. This is consistent with the arguments made in deriving the quantum Zeno ansatz.

The quantum Zeno ansatz provides a computationally attractive alternative to the quantum kinetic equations. The quantum Zeno ansatz follows the distribution functions which do not suffer from the oscillatory behavior in the density matrix. Quantum coherences, which are responsible for the $\nu_\alpha \to \nu_s$ scatterings, are treated in the scattering rate in a very simple manner without following the details of the quantum mechanics. By working with distribution functions instead of density operators, the number of independent evolution equations scales like N instead of N^2. While the quantum Zeno ansatz remains a nonlinear, integro-partial differential equation (in general, the matter mixing angle and oscillation length depends on integrals of the distribution functions), it is significantly less computationally demanding in determining the evolution of neutrinos in environments where decoherence dominates the quantum mechanical evolution [51].

1.2 Cosmology

Cosmology is the study of the origin and evolution of the universe. Within the past decade, the astrophysical community has conducted high-precision observations that have advanced our knowledge of the history of the universe by leaps and bounds. By combining these observations — including the anisotropies in the Cosmic Microwave Background (CMB), the fluxes from type Ia supernovae, the distribution of matter on all scales (from clusters of galaxies to the Lyman-α forest) — with large-scale computer simulations, cosmologists have been able to elucidate a self-consistent picture of the contents of the universe and its evolution.

The topics in this dissertation span a large fraction of the 13.72 ± 0.12 Gyr [35] history of the universe. Chapter 3 discusses sterile neutrino production within the first microsecond of the lifetime of the universe, Chapter 2 discusses active-sterile neutrino transformation within the first minute of the lifetime of the universe, and Chapter 5 discusses the evolution of neutrinos freely streaming through spacetime from the time they decouple from thermal equilibrium, 1 second into the lifetime of the universe, to the present epoch nearly 14 Gyr later.

1.2.1 The FLRW metric

One of the central principles in cosmology is the cosmological principle: on large scales ($\gtrsim$ 100 Mpc), the universe is homogeneous and isotropic. As a result, there exists a preferred frame where space-like hypersurfaces with constant time are homogeneous and isotropic. The conditions of homogeneity and isotropy imply that the metric (often written in the form of the spacetime interval) takes the form

$$ds^2 = -dt^2 + g_{ij}(t, \mathbf{x}) dx^i dx^j, \tag{1.62}$$

where the Einstein summation convention is used and the standard notation where Roman indices apply to only spacelike dimensions, while Greek indices include all spacelike and timelike dimensions.

If each t = const hypersurface is maximally symmetric, then the cosmological principle is satisfied for all t. A spacelike manifold is both homogeneous and isotropic if and only if it is maximally symmetric [66]. Homogeneity and isotropy implies that the spatial metric, g_{ij}, may depend on time only as an overall multiplicative factor. Isotropy implies that the the spatial metric is spherically symmetric about each point. As a result, the spacetime interval can be written in the form

$$ds^2 = -dt^2 + S^2(t)\left[B(r)dr^2 + r^2 d\Omega^2\right], \tag{1.63}$$

where $d\Omega^2 = d\theta^2 + \sin^2\theta\, d\phi^2$.

A maximally symmetric space is defined by its curvature, κ. The Riemann curvature tensor for such a space must be a function of only the curvature and the metric, and must possess all the symmetries related to the interchange of indices,

$$R_{ijkl} = \kappa\left(g_{ik}g_{jl} - g_{il}g_{jk}\right). \tag{1.64}$$

Comparing this expression with the three-dimensional Riemann curvature tensor derived from the spacelike component of Equation (1.63), results in the metric:

$$ds^2 = -dt^2 + S^2(t)\left(\frac{dr^2}{1-\kappa r^2} + r^2 d\Omega^2\right).$$

It is conventional to rescale $S(t) \rightarrow a(t) = S(t)/\sqrt{|\kappa|}$ for $\kappa \neq 0$, where $a(t)$ is known as the scale factor, resulting in the Friedmann-Lemaître-Robertson-Walker (FLRW) metric [67–70],

$$ds^2 = -dt^2 + a^2(t)\left(\frac{dr^2}{1-kr^2} + r^2 d\Omega^2\right), \tag{1.65}$$

where

$$k = \begin{cases} +1 & \text{positive curvature, closed universe} \\ 0 & \text{zero curvature, flat universe} \\ -1 & \text{negative curvature, open universe} \end{cases}.$$

Geodesics in the FLRW metric have constant spatial coordinates, that is $\mathbf{x} = (r, \theta, \phi) = \text{const}$. As a result, these spatial coordinates are called comoving coordinates. A fiducial observer has fixed comoving coordinates and observes the universe to be homogeneous and isotropic. (Observers on Earth are not fiducial observers because of peculiar velocities due to, for example, the Earth's orbit about the Sun, the galactic center, and the center of the Local Group.) The time coordinate, t, is a "universal time" and is the proper time measured by each fiducial observer. The assumptions of homogeneity and isotropy have given us a family of preferred reference frames and a notion of simultaneity between these frames (*i*.e. the ability to define a universal time).

The scale factor, $a(t)$, describes the "size" of the universe. Consider two fiducial observers who have fixed comoving coordinates. The proper distance between these two observers is proportional to the scale factor at the time the measurement is made. Observationally, the universe is expanding, so we expect $da/dt > 0$ at the current epoch.

1.2.2 Dynamics on the FLRW metric

The symmetries (or equivalently Killing vectors) of the FLRW metric imply that the spacelike (three-)momentum ($\mathbf{p}$) of particles traveling upon geodesics is inversely proportional to the scale factor,

$$\mathbf{p} \propto \frac{1}{a(t)}. \tag{1.66}$$

In cosmology, this result is most often used in describing photons traveling through the expanding universe. A photon's wavelength is inversely proportional to its momentum. If a photon has a wavelength of λ_i at time t_i ($i = 1, 2$), then

$$\frac{\lambda_1}{\lambda_2} = \frac{a(t_1)}{a(t_2)}. \tag{1.67}$$

This implies that in an expanding universe, if $t_1 < t_2$, then $\lambda_1 < \lambda_2$. That is, photons become "red-shifted" as they travel through the universe. In astrophysics, it is convenient to define the redshift, $z(t)$, in relation to this effect,

$$1 + z(t) = \frac{a(t_0)}{a(t)}, \tag{1.68}$$

where t_0 is the time of the present epoch. For an ultra-relativistic particle, energy is proportional to momentum, so its energy also redshifts. However, it is important to remember that it is the particle momentum, not energy, that redshifts. In Chapter 5, the implications of the redshifting of neutrinos is explored.

What remains is to determine the evolution of the scale factor. To do this, the contents of the homogeneous and isotropic universe are modeled as a perfect fluid with energy momentum tensor

$$T^{\mu\nu} = (\rho + \mathcal{P})u^\mu u^\nu + \mathcal{P}g^{\mu\nu}, \tag{1.69}$$

where u^μ is the four-velocity of the bulk fluid flow, ρ is the energy density of the fluid, and $\mathcal{P}$ is the pressure. Homogeneity and isotropy require that both ρ and $\mathcal{P}$ only depend on time. The solution to the Einstein field equations (with the “cosmological constant”) yields the Friedmann equations [67]:

$$H^2(t) \equiv \left(\frac{\dot{a}}{a}\right)^2(t) = \frac{8\pi}{3m_{pl}^2}\left[\rho(t) + \frac{\Lambda m_{pl}^2}{8\pi}\right] - \frac{k}{a^2(t)} \tag{1.70}$$

$$\frac{\ddot{a}}{a}(t) = -\frac{4\pi}{3m_{pl}^2}\left[\left(\rho(t) + \frac{\Lambda m_{pl}^2}{8\pi}\right) + 3\left(\mathcal{P}(t) - \frac{\Lambda m_{pl}^2}{8\pi}\right)\right], \tag{1.71}$$

where $H \equiv \dot{a}/a$ is the Hubble parameter. The Hubble constant, H_0, is the value of the Hubble parameter at the current epoch.

It is common practice to describe the cosmological constant as a form of dark energy, an unseen (thus, “dark”), constant energy density that fills all of space. The equation of state (pressure as a function of energy density) of this form of dark energy is

$$\mathcal{P}_\Lambda = -\rho_\Lambda = -\frac{\Lambda m_{pl}^2}{8\pi}. \tag{1.72}$$

While the prospect of a negative pressure is counter-intuitive, it is merely a statement that as the universe adiabatically expands, the total amount of dark energy in a comoving volume increases ($\mathcal{P} = -\partial E/\partial V$). Current data suggests that at the present epoch, dark energy makes up approximately 73% of the energy density in the universe. Although current data is consistent with the cosmological constant as the dark energy, there remains a plethora of viable theories regarding the content of dark energy [35].

The evolution of the energy density and pressure follows from the general relativistic analog of energy and momentum conservation: the stress energy tensor is divergenceless (${T^{\mu\nu}}_{;\nu} = 0$, the ";" corresponds to the covariant derivative). It follows that

$$\frac{d\rho(t)}{dt} = -3\frac{\dot{a}}{a}(t)\left[\rho(t) + \mathcal{P}(t)\right]. \tag{1.73}$$

It is often convenient to work in terms of the scale factor a as a timelike variable. $a(t)$ is typically a monotonically increasing function of time (the sign of da/dt from Equation (1.70) is chosen to agree with observations of the expanding universe), so the inversion, $t(a)$, may be performed, allowing the history of the universe to be described in terms of scale factor instead of time. If $k = +1$ (a positive spatial curvature, closed universe), there exists an epoch when $da/dt < 0$, representing an era of contraction of the universe. This is not the case in the history of the universe, so this complication is avoided.

Given the equation of state, $\mathcal{P}(\rho)$, of the contents of the universe, Equation (1.73) can be solved to determine the evolution of the energy density as a function of the scale factor, $\rho(a)$. It is conventional to classify the contents of the universe in three categories: matter (non-relativistic particles), radiation (ultra-relativistic particles), and dark energy (cosmological constant or some other exotic particles). Some particles (*e*.g., neutrinos) may be created as radiation but as their momenta redshift, become matter at a later epoch.

Non-relativistic matter includes both baryons and dark matter. Although dark matter has not been directly detected, its gravitational effects have been observed for decades. First proposed by Zwicky in 1933 to compensate for unseen mass in galaxy clusters [71], the composition of dark matter remains a hot topic in both theoretical and experimental astroparticle physics. Current data suggests that there is five times as much non-baryonic dark matter in the universe as baryonic matter. Matter particles have very little pressure, that is $\mathcal{P}_m \ll \rho_m$, thus it follows that $\rho_m \propto a^{-3}$. This is consistent with the notion that the energy density of matter is proportional to its number density which, in turn, is inversely proportional to the proper volume of a comoving region. If the energy density of the universe is dominated by non-relativistic matter, the Friedmann equation [Equation (1.70)] tells us that the time evolution of the scale factor is $a(t) \propto t^{2/3}$.

The radiative energy density consists of ultra-relativistic particles. At the current epoch, the cosmic microwave background radiation dominates this energy density, but in the early universe many other species were also ultra-relativistic. In a homogeneous and isotropic gas of ultra-relativistic particles, the equation of state is $\mathcal{P}_r = \rho_r/3$, so $\rho_r \propto a^{-4}$. This is also consistent with the number density of ultra-relativistic particles being proportional to a^{-3} along with the redshifting of the energy of ultra-relativistic particles as the universe expands. If the energy density of the universe is dominated by radiation, the time evolution of the scale factor is $a(t) \propto t^{1/2}$.

Finally, if the dark energy is a result of the cosmological constant (or a vacuum energy), then its equation of state is $\mathcal{P}_\Lambda = -\rho_\Lambda$. It follows that ρ_Λ is constant, as was described above. If the energy density of the universe is dominated by the cosmological constant, the time evolution of the scale factor is $a(t) \propto e^{Ht}$. However, if there are other components of the dark energy, then its equation of state would be different and hence its energy density will evolve with scale factor. While current results are consistent with a cosmological constant, further observations strive to discern between the cosmological constant and a number of other models of dark energy.

1.2.3 Thermal properties of the early universe

In the early universe, the scale factor is much smaller than it is at the current epoch. Since the momentum (and hence the energy in the case of radiation) of a

Table 1.2: The contents of the universe, including the evolution of the energy density in each component with scale factor and the evolution of the scale factor with time if the energy density of the universe is dominated by a single component. Also included is the fraction of the total energy density that each component comprises at the current epoch [35]. Missing from this table are the neutrinos which at early times behave as radiation but at late times may behave like matter. The fraction of the total energy density in neutrinos is constrained to be between 0.05 % and 0.7 % [35, 72].

	Evolution	Contents	Fraction
Matter	$\rho_m \propto a^{-3}$ $a(t) \propto t^{2/3}$	Baryons Dark Matter	4.6 % 23 %
Radiation	$\rho_r \propto a^{-4}$ $a(t) \propto t^{1/2}$	CMB	0.002 %
Dark Energy	$\rho_\Lambda = \text{const}$ $a(t) \propto e^{Ht}$	Cosmological constant/ Vacuum energy (?)	73 %

particle is inversely proportional to the scale factor, the energy in the radiation field is much larger than it is today. Considering the evolution of the energy density with scale factor of the different components summarized in Table 1.2, it follows that there is an era in the early universe when $\rho_r \gg \rho_m \gg \rho_\Lambda$. This is known as the radiation dominated era and is of principle interest in Chapters 2 and 3 in this dissertation. The radiation dominated era spans the first 50,000 years (approximately) of the lifespan of the universe.

The high energy density in radiation and a high number density of baryons results in a fully ionized universe. (This era of ionization extends into the matter dominated era for $\rho_r \gtrsim \rho_m/3$.) In this photon-baryon plasma, the interaction rate is large compared to the expansion rate of the universe. Thus, the plasma may be considered to be in thermal equilibrium. [Since the FLRW metric does not have a timelike Killing vector (*i.e.*, "energy" is not a conserved quantity in an expanding universe), the contents of the universe are not strictly in thermal equilibrium; rather the plasma in the early universe undertakes a series of local thermodynamic equilibria, connected by the adiabatic expansion of the universe. In a homogeneous and isotropic universe, net heat exchange cannot occur between a comoving volume and its environment. The expansion of the universe is adiabatic unless there are non-equilibrium dissipative processes that generate entropy.]

A particle is in local thermodynamic equilibrium if its scattering rate ($\Gamma = n\langle\sigma v\rangle$) is large compared to the expansion rate of the universe ($H = \dot{a}/a$). In a homogeneous and isotropic medium, the number density of a species in thermal equilibrium (hereafter, "thermal equilibrium" will denote local thermodynamic equilibrium), dn_i, in an energy interval dE_i is equal to the product of the density of states and the thermally averaged occupation number,

$$dn_i = \left[g_i \frac{p^2}{2\pi^2} \left(\frac{dE_i}{dp} \right)^{-1} dE_i \right] \cdot \left[\exp\left(\frac{E_i - \mu_i}{T_i} \right) \pm 1 \right]^{-1}, \tag{1.74}$$

where $p = |\mathbf{p}|$ is the magnitude of the spacelike momentum, $E_i(p)$ is the energy-momentum dispersion relation, g_i is the number of internal degrees of freedom (often related to the spin by $g_i = 2s_i + 1$, but there are notable exceptions: photons have $g_\gamma = 2$ as a massless gauge boson, and neutrinos of a given flavor have $g_{\nu_\alpha} = 1$ since the weak interaction only couples to left-handed neutrinos), μ_i is the chemical potential, T_i is the temperature, and the $(+)$ is applicable for fermions and the $(-)$ is for bosons. For a massive particle, $E_i(p) = \sqrt{p^2 + m_i^2}$, and this distribution can be written in familiar form,

$$dn_i = \frac{g_i}{2\pi^2(\hbar^3 c^2)} \frac{p\, E_i\, dE_i}{e^{(E_i - \mu_i)/k_B T_i} \pm 1}, \tag{1.75}$$

where the physical constants are reintroduced for illustrative purposes.

In general, each thermal species in the early universe may have a separate temperature. However, if the scattering rate of two species upon each other (*i*.e. the inelastic scattering rate, the rate at which the two species can efficiently share energy with each other) is large compared to the expansion rate of the universe, then they will share a common temperature. Furthermore, if species are in chemical equilibrium — for the chemical reaction between thermal species, $A + B \leftrightharpoons C + D$, the forward and reverse reaction rates are large compared to the expansion rate of the universe, $\lambda_{AB\to CD} = \lambda_{CD\to AB} \gg H$ — then their chemical potentials satisfy

$$\mu_A + \mu_B = \mu_C + \mu_D. \tag{1.76}$$

The chemical potential is zero for particles that can be created or destroyed in arbitrary numbers, such as the photon or Z^0. Thus, any particle-antiparticle pair that annihilates into and is repopulated by these particles have equal and opposite chemical potentials for both the particle (μ_i) and antiparticle ($\mu_{\bar{\imath}}$), $\mu_i = -\mu_{\bar{\imath}}$.

Thermodynamics of the radiation dominated era are of primary importance in this dissertation. Hence, the dynamics of the universe are governed by ultra-relativistic particles ($m_i \ll T_i$). This dissertation is concerned with thermal populations of gauge bosons (photon, gluon, $W^\pm$, and Z^0) which have zero chemical potentials, and a large array of fermions (quarks and charged and neutral leptons, and their antiparticles) which, in general, may have a chemical potential with $\mu_i = -\mu_{\bar{\imath}}$ for particle-antiparticle pairs.

For ultra-relativistic bosons,

$$n_i = \frac{\zeta(3)}{\pi^2}\, g_i T_i^3 \tag{1.77}$$

$$\rho_i = \frac{\pi^2}{30}\, g_i T_i^4. \tag{1.78}$$

While, for ultra-relativistic fermions,

$$n_i = \frac{3\zeta(3)}{4\pi^2} \cdot \frac{F_2(\eta_i)}{F_2(0)}\, g_i T_i^3 \tag{1.79}$$

$$\rho_i = \frac{7\pi^2}{240} \cdot \frac{F_3(\eta_i)}{F_3(0)}\, g_i T_i^4. \tag{1.80}$$

In the above equations, $\zeta(3) \approx 1.202\ 06$ is the Riemann zeta function of argument 3, $\eta_i \equiv \mu_i/T_i$ is the degeneracy parameter, and

$$F_k(\eta) \equiv \int_0^\infty \frac{x^k\, dx}{e^{x-\eta} + 1}, \tag{1.81}$$

is a function that is useful when dealing with thermal distributions of fermions. Finally, since $\mu_\imath = -\mu_{\bar{\imath}}$ (if the particle-antiparticle pair is in chemical equilibrium, the pair will also be in thermal equilibrium and thus share a common temperature), it is also useful to compute

$$n_i - n_{\bar{\imath}} = \frac{1}{6}\, g_i T_i^3 \left(\eta_i + \frac{1}{\pi^2} \eta_i^3 \right) \tag{1.82}$$

$$\rho_i + \rho_{\bar{\imath}} = \frac{7\pi^2}{120}\, g_i T_i^4 \left(1 + \frac{30}{7\pi^2} \eta_i^2 + \frac{15}{7\pi^4} \eta_i^4 \right). \tag{1.83}$$

In using the Friedmann equation, Equation (1.70), to describe the expansion rate of the universe, it is important to compute the total energy density $\rho = \sum_i \rho_i$. The total energy density can be written in terms of the photon temperature,

$$\rho = \frac{\pi^2}{30}\, g\, T_\gamma^4, \tag{1.84}$$

where g is the effective statistical weight in ultra-relativistic particles, which is calculated as a weighted sum of the bosonic (g_b) and fermionic (g_f) degrees of freedom,

$$g = \sum_{\text{bosons}} g_b \left(\frac{T_b}{T_\gamma} \right)^4 + \frac{7}{8} \sum_{\text{fermions}} g_f \left(\frac{T_f}{T_\gamma} \right)^4, \tag{1.85}$$

allowing each species to have a different temperature (in practice, the high densities in the early universe and the strength of the electromagnetic interaction result in most of the relativistic species in the early universe having the same temperature as the photons; notable exceptions include exotic particles produced out of equilibrium and neutrinos after they decouple from the plasma). In writing this, corrections of order η^2 are neglected. The degeneracy parameters, η_i, are expected to be small because the relative asymmetries of particles an antiparticles ($\sim \eta_i$) are small. Measured baryon asymmetries imply that $|\eta_{e^\pm}| \sim 10^{-9}$ [35] and measurements of primordial abundances imply that $|\eta_\nu| \lesssim 0.1$ [54].

Using the equation of state for ultra-relativistic particles ($\mathcal{P}_r = \rho_r/3$), the total proper entropy density can be written in a similar form

$$s = \frac{2\pi^2}{45}\, g_s\, T_\gamma^3, \tag{1.86}$$

where g_s is the effective entropic statistical weight in ultra-relativistic particles, which is calculated as a similar weighted sum of the bosonic and fermionic degrees of freedom,

$$g_s = \sum_{\text{bosons}} g_b \left(\frac{T_b}{T_\gamma}\right)^3 + \frac{7}{8} \sum_{\text{fermions}} g_f \left(\frac{T_f}{T_\gamma}\right)^3 . \tag{1.87}$$

The only difference between the expressions for g and g_s is the dependence on the temperature of the individual species. Since it is common for each species to have the same temperature, the two expressions are often blended into one statistical weight, as is done in Chapter 3.

Since the expansion of the universe is adiabatic, the total entropy in a comoving volume ($\propto g_s a^3 T_\gamma^3$) is conserved. As a result, the relationship between the temperature of the plasma and the scale factor of the universe is

$$T_\gamma \propto g_s^{-1/3} a^{-1}. \tag{1.88}$$

When considering the adiabatic expansion of a gas of ultra-relativistic particles, the adiabatic invariant, $V^{1/3}T = \text{const}$, implies that $T_\gamma \propto a^{-1}$. What causes the discrepancy between these two behaviors? The difference lies in the physical mechanisms that cause g_s to evolve in time. There are two main causes for a changing g_s: phase transitions and particle-antiparticle pair annihilation.

In a cosmological phase transition, the energy scale of the universe ($\sim T_\gamma$) is reduced to a point where spontaneous symmetry breaking results in a loss of degrees of freedom in the plasma of the early universe. One example is the QCD transition (*a.k.a.* the quark-hadron transition) which occurs at a temperature ~ 170 MeV [73]. The QCD transition is precipitated by the breaking of chiral symmetry, forcing free quarks and gluons to be bound into color singlets (*i.*e., hadrons: baryons and mesons). The result is that a large fraction of the degrees of freedom prior to the transition in quarks ($g_f = 12n_q$, where n_q is the number of relativistic quarks; immediately prior to the QCD transition $n_q = 2$ or 3, depending on if the strange quark is relativistic) and gluons ($g_b = 16$) are lost. In this phase transition, latent heat is released, serving to heat up the plasma of the universe.

In the early universe, particle-antiparticle pairs are in equilibrium — their production rate is equilibrated with their annihilation rate. When the temperature of the plasma falls to the point where the number density of photons with the threshold energy to create the particle-antiparticle pair becomes exponentially suppressed (*i*.e., $m_i \gtrsim T_\gamma$), the production rate of the particle-antiparticle pair will fall off exponentially. This will result in a reduced number density of the particle and antiparticle in the equilibrated plasma. The entropy that was once in these particle and antiparticle populations is transferred to the thermally coupled components in the plasma, resulting in heating the plasma.

These concerns are no longer relevant for particles once they fall out of thermal equilibrium with the rest of the universe. Once these particles' scattering rate becomes smaller than the expansion rate of the universe, they are effectively decoupled from the plasma of the universe. If, in addition, the annihilation rate of the species (or any other rate the destroys but does not repopulate the species) is small compared to the expansion rate of the universe, then the particle species will freely fall through spacetime with its momentum redshifting and its number density proportional to a^{-3}.

If a species decouples from the plasma of the universe at a scale factor a^D (corresponding to a temperature T_i^D), then at a later epoch the number density of particles in a momentum interval dp is

$$dn_i = \frac{g_i}{2\pi^2}\frac{p^2\,dp}{e^{(E_i-\mu_i)/T_i^D} \pm 1}, \tag{1.89}$$

where $E_i = E_i[p(a/a^D)]$ is the energy-momentum dispersion relation corrected for the redshifting of the momentum, and notice that this expression is in terms of momentum in contrast with Equation (1.75); it can be argued that working with momenta instead of energy is a natural way to describe decoupled particles because the momentum of decouple particles redshift, not their energy.

If the decoupled species is ultra-relativistic (*e*.g., photons, which decouple from the plasma at $T_\gamma \sim 0.2$ eV), then the number density of the decoupled particles is

$$n_i = \frac{g_i}{2\pi^2}T_i^3(a)\int_0^\infty \frac{x^2\,dx}{e^{x-\mu_i/T_i(a)} \pm 1}, \tag{1.90}$$

where the "temperature" $T_i(a) = T_i^D(a^D/a)$. The result is that the temperature of this distribution of decoupled particles is proportional to a^{-1}, as is the case for a thermally coupled particle while the number of degrees of freedom remain unchanged. While this "temperature" is not strictly a temperature in a thermodynamic sense [the decoupled particle distribution is not a result of a thermal equilibrium at temperature $T_i(a)$], it is a "color temperature" — a parameter that describes the energy distribution of the decoupled particles as in Equation (1.75). Another result is that the degeneracy parameter, $\eta_i = \mu_i/T_i(a)$, is constant for decoupled particles. This is true because the number density of the decoupled particles must be proportional to a^{-3}.

The story becomes slightly more complicated if the decoupled particle has a rest mass. As the universe expands, its momentum redshifts and there is a point where the particle's kinematics becomes non-relativistic. In this case, the "temperature" of the distribution can still be regarded as being proportional to a^{-1} when describing a momentum distribution (not the typical energy distribution). This point is discussed in Chapter 5.

1.2.4 A thermal history of the universe

The expansion of the universe was first observed by Edwin Hubble in the 1920's as he observed that the apparent recessional velocity (redshift) of distant galaxies was proportional to the distance to these galaxies [74]. In the FLRW metric, neglecting peculiar velocities, two galaxies have fixed comoving coordinates so the proper distance between these two galaxies is proportional to the scale factor. As the universe expands, the proper distance between the two galaxies increases, which in the rest frame of one galaxy appears to be a recessional velocity. The measured redshift is a result of the expansion of the universe, not the result of the Doppler effect due to a recessional velocity.

If this expansion is extrapolated backward in time, the scale factor decreases and the energy density of the universe increases. As described above, the high energy density of photons and high number density of baryons results in the ionization of the universe. At this phase transition between an ionized plasma and neutral baryons (commonly referred to as "recombination"), the CMB is created. The CMB last interacted with the matter in the universe at this "surface of last scattering." The existence of the CMB and its thermal spectrum are among the triumphs of the Big Bang theory in describing the evolution of the universe.

Continuing the extrapolation backward, the plasma of the universe reaches a high enough temperature (and thus high enough density) that thermal seas of neutrinos and antineutrinos of all flavors are in thermal equilibrium. This is the furthest point to which there is evidence that this extrapolation makes some sense. Although the analogous cosmic neutrino background cannot be detected, the effects of the thermal seas of neutrinos are imprinted in the primordial abundances of the elements as a result of Big Bang Nucleosynthesis (BBN). The observations of the primordial helium and deuterium abundances are consistent with thermal seas of neutrinos in the early universe.

However, as theorists, we can continue the extrapolation to higher temperatures and densities, including those that cannot be probed in terrestrial laboratories. This thought experiment may be continued until the scale factor tends to zero, thus the size of the universe goes to zero and the density and temperature diverge. This singularity is regarded as the "beginning" of the universe and is referred to as the "Big Bang." The first 10^{-43} seconds of the lifetime of the universe is beyond the realm of current (well-accepted) physical theories. It is believed that this is the era where quantum gravity is important in describing the physics of the universe.

The next significant event is inflation, thought to occur approximately 10^{-34} seconds (a temperature on the order of 10^{19} MeV) after the Big Bang. The era of inflation was the brainchild of Alan Guth in 1980, who proposed it to solve a number of problems with the Big Bang theory. While cosmology based on the FLRW metric is largely successful in describing the observable universe, a number of questions remain unanswered: why does the universe appear to be largely flat, homogeneous, and isotropic even though distant parts of the universe were never causally connected? what is the origin of the inhomogeneities that evolved into large scale structure in the universe? and where are the exotic particles, such as magnetic monopoles, that many theories predict should have been created in the early universe?

The idea, originally proposed by Guth [75] and modified by Linde [76] and Albrecht and Steinhardt [77], is that a type of vacuum energy dominates the energy density during inflation, resulting in an exponential growth of the scale factor of the universe. In all, the universe undergoes at least 60 *e*-foldings in expansion. During this expansion, the proper distance between two fiducial observers increases at a rate faster than the speed of light; the space between them expands, no particle (nor information) travels at a speed faster than the speed of light. This "super-luminal" expansion allows regions of the universe that would otherwise appear to have never been in causal contact to have been in causal contact in the distant (pre-inflation) past. The prodigious universal expansion dilutes the number density of exotic particles and serves to reduce the curvature of the universe. Inflation puts the "Bang" in the Big Bang.

Since the CMB and BBN imply that the universe was once hot and dense (post-inflation), the period of inflation was followed by a period of reheating, where a significant amount of entropy was created in the universe. Typically, reheating is assumed to return the universe to its pre-inflation temperature, but studies of the CMB and primordial light element abundances (from BBN) suggest that the minimum reheating temperature of the universe is around 4 MeV (although this does not suggest a prescription for baryogenesis) [78].

The current theory of inflation involves a scalar field, the inflaton, that undergoes a phase transition in the early universe. At which point, the inflaton "slowly rolls" from a false vacuum toward the actual vacuum (exponential expansion). During this expansion, quantum fluctuations in the inflaton field produce the seeds of the density fluctuations that will eventually form large scale structure in the universe. Once the inflaton field reaches the vacuum, its "potential energy" is dissipated through particle creation (entropy generation / reheating) (see, *e*.g., Ref. [79] for details). While encompassing a very brief timescale ($\sim 10^{-32}$ seconds), inflation is a key concept in understanding the universe and its evolution. Tests of the inflationary theory include probing the CMB and large scale structure for the power spectrum of the density perturbations created during inflation, searching for polarization of the CMB resulting from gravitational waves due to inflation, and the direct search for a primordial gravitational wave background from the inflationary era.

After the inflationary era, the universe adiabatically expands and, as discussed above, the temperature of the plasma decreases. As the temperature decreases, a number of phase transitions occur and thermonuclear reactions freeze out of equilibrium. One of the first phase transitions is the electro-weak transition which occurs when the universe is at a temperature $T^c_{\mathrm{EW}} \sim 100$ GeV [80], which corresponds to approximately 25 picoseconds after the Big Bang. (There are possibly other phase transitions that precede this one, for example, spontaneous symmetry breaking between the strong and electro-weak forces, but these are at energy scales much higher than are testable in terrestrial experiments.) At this transition, the intermediate vector gauge bosons (W^+, W^- and Z^0) become massive as the electro-weak symmetry ($SU(2) \times U(1)$) is broken [81]. Before the transition, the electro-weak symmetry protects the intermediate vector gauge bosons from acquiring mass. As a result, the weak force is long-range and is unified with the electromagnetic force. After the transition, the now massive bosons quickly become non-relativistic and decay.

As the temperature of the plasma continues to decrease, the number density of photons with the threshold energy to repopulate particle-antiparticle pairs decreases. Once $T_\gamma \lesssim m_i$, the particle-antiparticle production rate is exponentially suppressed (when $T_\gamma \lesssim m_i$, the production rate is roughly proportional to $n_\gamma^2 e^{-2m_i/T_\gamma}$). While thermal and chemical equilibrium continue to obtain, the particle-antiparticle annihilation rate ($\propto n_i n_{\bar{\imath}}$) is equal to the production rate, and as a result the number density of the particle and the antiparticle become exponentially suppressed. This result can also be derived from the particle distribution function, Equation (1.75), in the non-relativistic limit. Eventually, the temperature of the plasma becomes low enough that the annihilation (and production) rate becomes small compared to the expansion rate of the universe so the number densities will be proportional to a^{-3}.

Perhaps the most interesting and well studied phase transition in the early universe is the QCD transition which occurs when the temperature drops to $T^c_{\rm QCD} \sim 170$ MeV. At this transition, chiral symmetry is spontaneously broken, forcing the asymptotically free quarks and gluons that populate the plasma being bound into baryons (three quarks) and mesons (quark-antiquark bound pair). Before the QCD transition, $g_s \approx 61.75$, which includes gluons and the three lightest quarks; after the QCD transition, $g_s \approx 17.25$, as the gluon and quark degrees of freedom annihilate as they are confined in relativistic pions ($m_\pi \sim 140$ MeV) and other non-relativistic hadrons. The nature of this transition remains an active area of research [73, 82, 83], and may affect the production of a dark matter candidate sterile neutrino [51, 84].

After the QCD transition, the universe continues to adiabatically expand and the temperature of the photon-hadron plasma continues to decrease. Soon after the phase transition, the pions and muons become non-relativistic and, as described above, annihilate with their antiparticles. At this point in time ($T_\gamma \lesssim 100$ MeV), the photon-baryon plasma of the universe is comprised of thermal populations of ultra-relativistic electrons, neutrinos and their antiparticles, along with significantly fewer protons and neutrons and virtually nothing else that once existed in the hot quark-gluon plasma.

The thermal seas of active neutrinos are thermally coupled to the baryons and electrons in the plasma through weak scattering (in turn, these fermions are thermally coupled to the photons through electromagnetic scattering, resulting in the neutrinos and photons being thermally coupled). The neutrinos will decouple from the rest of the plasma when the temperature and density has decreased to a point where the weak scattering rate is small compared to the expansion rate. This point where the neutrinos decouple can be estimated; the weak scattering rate is

$$\Gamma_w = n\langle\sigma v\rangle \sim G_F^2 T_\gamma^5, \tag{1.91}$$

since the number density of particles with weak charge, $n \sim T_\gamma^3$, and the thermally averaged scattering cross section, $\langle\sigma\rangle \sim G_F^2 T_\gamma^2$. Comparing the scattering rate to the expansion rate, $H \sim T_\gamma^2/m_{pl}$, results in

$$\frac{\Gamma_w}{H} \sim \left(\frac{T_\gamma}{1\ \mathrm{MeV}}\right)^3. \tag{1.92}$$

The neutrinos decouple when $T_\gamma \sim 1$ MeV. A detailed analysis of neutrino scattering off of electrons and positrons in the plasma yields a neutrino decoupling temperature of $T^D_{\nu_e} \approx 1.8$ MeV for electron neutrinos and $T^D_{\nu_\mu,\nu_\tau} \approx 3.1$ MeV for μ and τ neutrinos [85]. Electron neutrinos decouple at a lower temperature than the other active neutrinos because they have a higher scattering rate. At this stage of the early universe there is a thermal population of electrons but not muons nor tauons, so electron neutrinos have an "extra" charged current scattering while the others do not.

Since the mass of the electron is $m_e = 0.511$ MeV, the electrons and positrons will become non-relativistic after the neutrinos decouple and will annihilate with each other. When the electrons and positrons annihilate, the entropy that was once in their (ultra-relativistic) thermal populations is transferred to the thermally coupled components of the plasma. So to first order, as the electrons and positrons annihilate, the temperature of the photon-baryon plasma will increase while the "temperature" of the neutrinos continues to be proportional to a^{-1}. The result is that after the electrons and positrons have annihilated, the neutrino and photon temperatures are related by

$$T_\nu = \left(\frac{4}{11}\right)^{1/3} T_\gamma. \tag{1.93}$$

However, since both neutrino decoupling and electron-positron annihilation are not instantaneous events, there is some overlap between the two. Since the cross section of neutrino interaction with matter is proportional to the square of its energy, higher energy neutrinos remain coupled with the plasma to a lower temperature than lower energy neutrinos. As a result, the annihilation reaction $e^+e^- \to \nu\bar{\nu}$ serves to heat the neutrinos, at least those with high energies (*i.e.*, the rate of this reaction is not insignificantly small compared to the expansion rate). This results in a distorted neutrino spectrum of neutrinos at high energies (more significant for electron neutrinos than μ or τ neutrinos because of higher cross sections due to charged current scattering) and since some entropy is deposited into the populations of active neutrinos, the photon-baryon plasma is reheated to a slightly lesser extent than if the neutrinos were unaffected [85, 86].

In this era, neutrinos play an integral role in big bang nucleosynthesis. At early times ($T_\gamma \gtrsim 1$ MeV), the photon-baryon plasma is in nuclear statistical equilibrium (NSE). In NSE, the processes that create a given nucleus is in chemical equilibrium with processes that destroy it, so the abundances of nuclei in NSE are prescribed by the Saha equation,

$$X_{(A,Z)} \approx \frac{g_{(A,Z)}}{2} \left(\frac{2\sqrt{2}\zeta(3)}{\sqrt{\pi}} \right)^{A-1} A^{5/2} \left(\frac{T}{m_N} \right)^{3(A-1)/2} \eta^{A-1} X_p^Z X_n^{A-Z} e^{B_{(A,Z)}/T}, \quad (1.94)$$

where X_i is the mass fraction of species i, (A, Z) is a nucleus with mass number A and atomic number Z, $g_{(A,Z)}$ is the effective statistical weight of the nucleus, $m_N \approx m_p$ is the nucleon mass, η is the baryon-to-photon ratio, and $B_{(A,Z)}$ is the binding energy of the nucleus:

$$B_{(A,Z)} = Zm_p + (A - Z)m_n - m_{(A,Z)}. \quad (1.95)$$

Since $T_\gamma \ll m_p$ and the baryon-antibaryon asymmetry is small compared to the number density of photons, the baryon-to-photon ratio is very small. Measurements of the CMB imply that $\eta \approx 6 \times 10^{-10}$ at the time the CMB decouples which corresponds to $\eta \approx 3 \times 10^{-10}$ at the beginning of the BBN epoch since electron-positron annihilation increased the number density of photons relative to baryons. The small baryon-to-photon ratio means that the entropy-per-baryon is very large ($s/n_b \sim \eta^{-1}$). The highly entropic environment of the early universe favors the existence of nuclei with small atomic numbers over those with large atomic numbers

For $T \gtrsim 1$ MeV, the baryon content of the universe is contained in either free protons or neutrons. The ratio of neutrons to protons is set by the chemical equilibrium of three weak reactions

$$\begin{aligned} \nu_e + n &\rightleftharpoons p + e^- \\ \bar{\nu}_e + p &\rightleftharpoons n + e^+ \\ n &\rightleftharpoons p + e^- + \bar{\nu}_e. \end{aligned} \tag{1.96}$$

If the neutrinos have a Fermi-Dirac spectrum with chemical potential μ_{ν_e} and temperature T_γ, while chemical equilibrium obtains, the neutron-to-proton ratio is

$$\frac{n}{p} \approx e^{-\delta_{np}/T_\gamma} e^{-(\mu_{\nu_e} - \mu_e)/T_\gamma}, \tag{1.97}$$

where $\delta_{np} \equiv m_n - m_p = 1.293$ MeV is the neutron-proton mass difference [54]. As discussed in the previous section, the small baryon-to-photon ratio and assuming charge neutrality implies that $|\mu_e/T_\gamma| \sim 10^{-9}$, while the limits on the neutrino chemical potentials are much less stringent, $|\mu_{\nu_e}/T_\gamma| \lesssim 0.1$.

The neutrinos and baryons remain in chemical equilibrium until the reaction rates become small compared to the expansion rate which occurs when $T_\gamma \approx 0.7$ MeV. This occurs at a lower temperature (and thus at a later time) than when the neutrinos thermally decouple from the photon-baryon plasma. The neutrinos affect the baryon content even when it has come to the point where it cannot efficiently share energy with the plasma. At this point, the neutron-to-proton ratio is $n/p \approx (1/6)e^{-\eta^D_{\nu_e}}$, where $\eta^D_{\nu_e}$ is the degeneracy parameter (chemical potential divided by temperature) when the neutrinos chemically decouple from the baryons. This value of the neutron-to-proton ratio would be frozen in at this point, if not for the fact that free neutrons decay into a proton, electron, and antineutrino with a mean lifetime of 885.7 ± 0.8 s [22]. As a result, the neutron-to-proton ratio continues to decline.

As the universe continues to expand, the plasma cools and the baryon density decreases, so that the reaction rates that create light nuclei slow down to the point where NSE is lost. For example, at $T_\gamma \approx 0.6$ MeV, ^{4}He falls out of NSE because the reactions that create the nucleus becomes slow compared to the expansion rate. The reaction chain that creates ^{4}He nuclei begins with deuterium, an elements whose relatively small binding energy ($B_D = 2.224$ MeV [87]) results in a small equilibrium concentration in NSE. This “deuterium bottleneck” is responsible for all of the other light elements falling out of NSE because the reaction chains that create each of those nuclei begin with the formation of deuterium and the baryon densities are low enough that three-body reactions are not significant.

One could imagine that once the temperature of the photon-baryon plasma has cooled below the binding energy of deuterium, it would become energetically favorable for deuterium to form. However, since there are $\sim 10^9$ photons per baryon, the formation of deuterium is suppressed. By examination of the Saha equation, deuterium production becomes significant around $T_\gamma \sim 70$ keV [85]. However, once a significant fraction of deuterium is created, reactions that use deuterium to create heavier nuclei become significant, and deuterium falls out of NSE.

Once the deuterium bottleneck is subverted, nearly every neutron in the photon-baryon plasma is captured into a ^{4}He nucleus since it is the most tightly bound nucleus among the light elements. When the calculation is done, in the standard model (with thermal distributions of neutrinos and $\eta_\nu \ll 1$) the neutron-to-proton ratio is approximately 1/7 at this point in time, resulting in a mass fraction of ^{4}He of approximately 25%. The early universe would be solely comprised of protons and ^{4}He if not for the fact that the eventual paucity of non-^{4}He nuclei causes the rate at which ^{4}He forms to become small compared to the expansion rate and the abundances of the elements are “frozen in.” Nuclei heavier than ^{7}Li are not created during BBN because there are no stable nuclei with $A = 5$ or 8, a low baryon density suppresses three-body reactions (such as the triple-α reaction to form ^{12}C), and coulomb repulsion becomes significant as the temperature decreases.

Big Bang Nucleosynthesis calculations have been carried out that time evolve the abundances of nuclei in an expanding universe, following a reaction network of nuclides. Using the baryon-to-photon ratio measured in observations of the CMB, the ^{4}He mass fraction is $Y_p = 0.2429$, and the deuterium abundance relative to hydrogen is D/H $= 2.543 \times 10^{-5}$ [88]. These values agree, within errors, with the observationally inferred primordial abundances. However, the uncertainty in the observationally determined primordial abundance is quite large. The primordial ^{4}He mass fraction is likely between 23% and 26% [89–91], while the statistical uncertainty in D/H is between 15% and 30% [92].

Historically, primordial light element abundances have been used to infer a measurement of the baryon density in the universe. A comparison of the observationally-inferred primordial abundances of ^{4}He and D with calculated BBN abundances can be used to determine the baryon-to-photon ratio (η). A larger value of η means that deuterium would begin to form at an earlier time (from the Saha equation, $X_D \propto \eta$) so the deuterium bottleneck is resolved when the neutron-to-proton ratio is slightly higher, resulting in a larger ^{4}He yield. Since the neutron-to-proton ratio is solely affected by neutron decay at this time, the ^{4}He abundance weakly increases with increasing η. However, a larger value of η would keep processes that convert deuterium into ^{4}He in chemical equilibrium longer. The result is that D/H is strongly dependent, decreasing function of η. This strong dependence allows measurements of D/H to provide a high precision measurement of η, at least when we assume the standard model of BBN (zero neutrino chemical potentials and no exotic physics).

The derived value of η using primordial elemental abundances is in good agreement with the CMB-derived value [92–95]. While the fractional uncertainty in the ^{4}He abundance may be smaller than that in the measurement of D/H, systematic errors in inferring the ^{4}He abundance from the observations [91] along with the weak dependence of the abundance on η may doom it as a probe of the baryon content of the universe. However, the D/H ratio as measured by isotope-shifted hydrogen absorption lines along the line of sight to high redshift QSO's may improve the statistical uncertainties as newer telescopes provide many more QSO lines of sight [88].

It would be interesting if the uncertainty in the D/H measurement, and hence on the BBN-inferred value of η, could rival the uncertainties in inferring η from the CMB. In this scenario, precision measurement of primordial abundances can serve as a probe of non-standard physics in the early universe [88]. Comparing observed primordial abundances with those predicted by BBN calculations can prove to be a novel method toward studying new physics in the early universe. Discrepancies between theory and observation can lead to a better understanding of nuclear reaction rates or of weak or exotic physics. Chapter 2 discusses changes in the ^{4}He abundance with the introduction of a light sterile neutrino and lepton numbers in the active neutrinos. Ref. [88] looks at this scenario and its effects on the primordial abundances of deuterium, ^{4}He, and ^{7}Li, while Ref. [87] discusses the potential effects on the BBN calculations of an arbitrary neutrino distribution function.

Big Bang Nucleosynthesis light element abundances may be a useful probe into weak physics, and possibly exotic physics, in the early universe. BBN abundance yields are sensitive to the expansion rate of the universe during the BBN epoch and the evolution of the neutron-to-proton ratio. In this vein, the neutrino distribution functions are pertinent to both concerns. For example, if there was a net lepton number in the neutrino sector (that is, asymmetry between the neutrino and antineutrino number densities for a given active flavor), then the neutrinos would have Fermi-Dirac distribution functions with non-zero chemical potentials. The non-zero chemical potentials will increase the energy density of neutrinos in the early universe, and in turn increase the expansion rate of the universe, resulting in the weak rates freezing out of equilibrium at an earlier epoch, with a higher neutron-to-proton ratio. However, if there is a positive chemical potential, there is an excess of neutrinos over antineutrinos, boosting the reaction $n + \nu_e \rightarrow p + e^-$, which reduces the neutron-to-proton ratio. The effect on the expansion rate is of order $(\mu/T_\gamma)^2$ while the effect on the weak reaction rates is of order (μ/T_γ), so the primordial abundance of ^{4}He, deuterium, and ^{7}Li ought to decrease with increasing lepton numbers (or equivalently increasing chemical potentials) [88]. This analysis may be done with respect to the current observational measurements of the primordial light element abundances to place an upper bound on the degeneracy parameter (chemical potential divided by temperature) for neutrinos in the early universe, $|\eta_\nu| \lesssim 0.1$ [54].

By the time the photon-baryon plasma has cooled to $T_\gamma \sim 10$ keV, the BBN rates have fallen below the expansion rate and the abundances of the light elements are set. This corresponds to the first three hours in the lifespan of the universe. The photon-baryon plasma contains approximately a 3:1 ratio by mass of hydrogen to helium nuclei, enough electrons to ensure net charge neutrality, and approximately

10^9 photons per baryon. As the universe continues to adiabatically expand, the temperature of the plasma continues to decrease, and the temperature of the neutrinos, although they are chemically and thermally decoupled from the photon-baryon plasma, continues to decrease as well and is approximately 70% of the temperature of the plasma. Very little of interest occurs in the next $\sim 100,000$ years. Figure 1.5 shows the temporal evolution of a number of quantities of interest in the early universe.

When the plasma has cooled to $T_\gamma \approx 0.77$ eV, the energy density in radiation is equal to the energy density in matter. The radiation dominated era has ended, and the matter dominated era has commenced. Once again, one would expect that since the ionization energy of hydrogen is 13.6 eV that by this time, neutral atoms would have formed as electrons are captured by nuclei. However, just as above, the large number of photons per baryon means that the electrons will remain free until the photons have cooled to a temperature significantly less than the ionization energy. Energetic photons in the exponential tail of the distribution are sufficient to maintain ionization equilibrium. Analysis of the Saha equation (applied to the ionization equilibrium $p + e^- \rightleftharpoons \mathrm{H} + \gamma$) along with observations of the CMB determine that when $T_\gamma \approx 0.26$ eV, the photon-baryon plasma has sufficiently cooled so the protons and electrons have "recombined" (although there were not combined in the first place) to form hydrogen atoms. At this phase transition, where the number density of free electrons has been drastically decreased, the photons (which were kept in thermal equilibrium through scattering off free electrons) decouple from the baryons. So, at "recombination," the photons cease to interact with the baryons. These photons comprise the CMB and have not significantly interacted (electromagnetically) with matter since it has left this "surface of last scattering."

Observations of the CMB have improved the understanding of the evolution of the universe. The CMB was first discovered by Arno Penzias and Robert Wilson in 1965 [96]. It is a nearly isotropic background radiation with a "temperature" of 2.725 K. The era of conducting precision cosmology began in earnest with the results of the COsmic Background Explorer (COBE) satellite in the 1990's that discovered

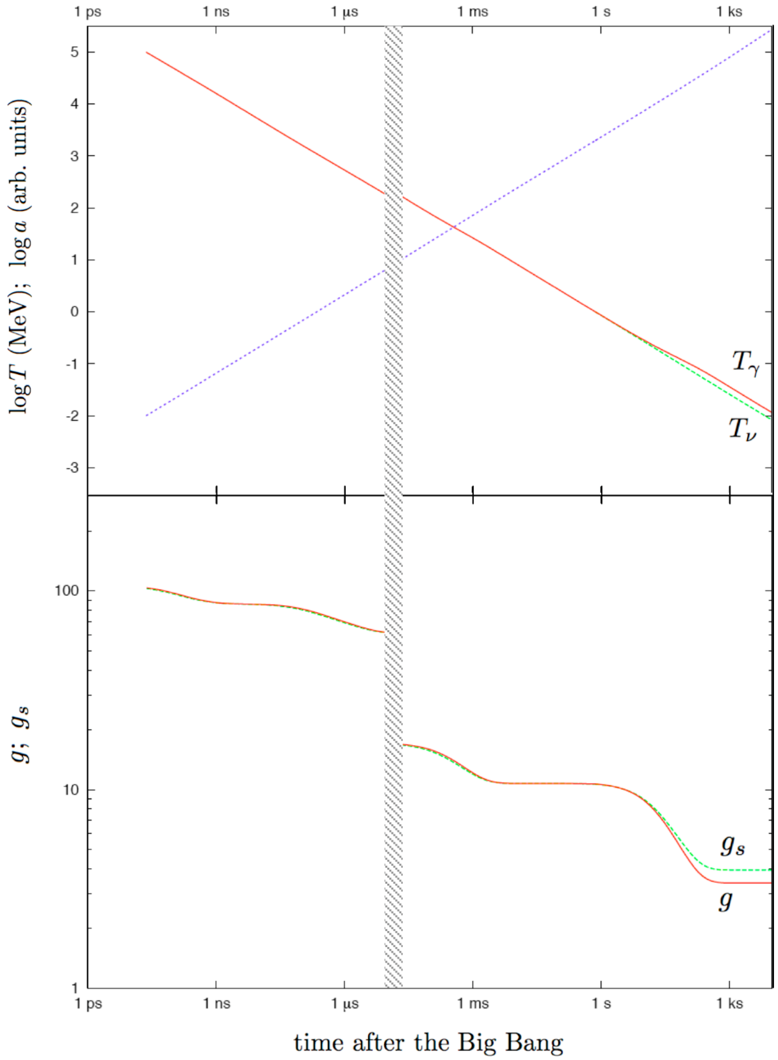

Figure 1.5: The time evolution of a number of important quantities in the early universe. The top panel shows the evolution of the temperature of the photon-baryon plasma (solid), T_γ, and the evolution of the scale factor (short dashed). The long-dashed curve that slightly deviates from T_γ at late times is the neutrino temperature, T_ν. The bottom panel shows the two effective statistical weights in ultra-relativistic particles as described in the previous section. The solid curve is for g, the statistical weight associated with energy and the dashed curve is for g_s which is associated with entropy. The shaded region is the QCD phase transition.

Table 1.3: Cosmological parameters derived from *WMAP* five-year data, baryon acoustic oscillation data, and supernovae data.

Cold Dark Matter closure fraction	Ω_c	0.228 ± 0.013
Baryonic closure fraction	Ω_b	0.0456 ± 0.0015
Dark Energy closure fraction	Ω_Λ	0.726 ± 0.015
Baryon to Photon ratio	η	$(6.202 \pm 0.016) \times 10^{-10}$
Hubble Constant	h	0.705 ± 0.013
Age of the Universe (Gyr)	t_0	13.72 ± 0.12

anisotropies (about 1 part in 10^5) in the temperature of the CMB [97]. Since then, a number of ground-, balloon-, and satellite-based studies have improved the precision of the measurements of these anisotropies in the CMB.

The state-of-the-art in CMB measurements have come from the Wilkinson Microwave Anisotropy Probe (WMAP), whose five-year data has recently been analyzed [35]. Combined with luminosity distance measurements to Type Ia supernovae and measurements of baryon acoustic oscillations, measurements of the spatial correlations of the part-in-10^5 anisotropies of the CMB allow for precision cosmology in measuring the energy content and evolution of the universe. Table 1.3 outlines a few key results from the analysis of the five-year data from WMAP. The closure fraction of a variety of components of the universe is reported as a fraction of the critical density,

$$\rho_{\rm crit} \equiv \frac{3m_{pl}^2 H_0^2}{8\pi} = 8.096 \times 10^{-35}\, h^2 \ {\rm MeV}^4 = 10.54\, h^2 \ {\rm keV\,cm^{-3}}, \tag{1.98}$$

where the Hubble constant is parameterized by h, which is the Hubble constant in units of 100 $\rm km\,s^{-1}\,Mpc^{-1}$,

$$h = \frac{H_0}{100 \ {\rm km\,s^{-1}\,Mpc^{-1}}} \ . \tag{1.99}$$

The closure fraction at the current epoch, Ω_i, of a species i is the ratio of its energy density to the critical energy density, $\Omega_i \equiv \rho_i/\rho_{\rm crit}$. If $\sum_i \Omega_i = 1$, then the universe is flat. That is, every constant time hypersurface is flat, the spacelike metric may be characterized globally by a Euclidean metric. Observations from the WMAP satellite are consistent with a flat universe, $\sum \Omega_i = 1.0050 \pm 0.0060$ [35].

Bibliography

[1] H. Becquerel, Comptes Rendus **122**, 420 (1896).

[2] J. Chadwick, Verhandlungen der Deutschen Physikalische Gesellschaft **16**, 383 (1914).

[3] K. Riesselmann, Symmetry **4**, (2), C3 (2007).

[4] F. Reines and C. L. Cowan, Jr., Nature **178**, 446 (1956).

[5] T. D. Lee and C. N. Yang, Physical Review **104**, 254 (1956).

[6] C. S. Wu, E. Ambler, R. W. Hayward, D. D. Hoppes and R. P. Hudson, Physical Review **105**, 1413 (1957).

[7] M. Goldhaber, L. Grodzins and A. W. Sunyar, Physical Review **109**, 1015 (1958).

[8] S. L. Glashow, Nuclear Physics **22**, 579 (1960).

[9] S. Weinberg, Physical Review Letters **19**, 1264 (1967).

[10] A. Salam, in *Proceedings of the 8th Nobel Symposium on Elementary Particle Theory, Relativistic Groups and Analyticity*, edited by N. Svartholm, p. 367, Stockholm, 1968, Almqvist and Wikell.

[11] G. 't Hooft and M. Veltman, Nuclear Physics B **44**, 189 (1972).

[12] F. Hasert, H. Faissner, W. Krenz, J. V. Krogh, D. Lanske, J. Morfin, K. Schultze, H. Weerts, G. Bertrand-Coremans, J. Lemonne, J. Sacton, W. V. Doninck, P. Vilain, C. Baltay, D. Cundy, D. Haidt, M. Jaffre, P. Musset, A. Pullia, S. Natali, J. Pattison, D. Perkins, A. Rousset, W. Venus, H. Wachsmuth, V. Brisson, B. Degrange, M. Haguenauer, L. Kluberg, U. Nguyen-Khac, P. Petiau, E. Bellotti, S. Bonetti, D. Cavalli, C. Conta, E. Fiorini, M. Rollier, B. Aubert, L. Chounet, P. Heusse, A. Lagarrigue, A. Lutz, J. Vialle, F. Bullock, M. Esten,

T. Jones, J. McKenzie, A. Michette, G. Myatt, J. Pinfold and W. Scott, Physics Letters B **46**, 121 (1973).

[13] G. Arnison, A. Astbury, B. Aubert, C. Bacci, G. Bauer, A. Bzaguet, R. Bck, T. J. V. Bowcock, M. Calvetti, T. Carroll, P. Catz, P. Cennini, S. Centro, F. Ceradini, S. Cittolin, D. Cline, C. Cochet, J. Colas, M. Corden, D. Dallman, M. DeBeer, M. D. Negra, M. Demoulin, D. Denegri, A. D. Ciaccio, D. DiBitonto, L. Dobrzynski, J. D. Dowell, M. Edwards, K. Eggert, E. Eisenhandler, N. Ellis, P. Erhard, H. Faissner, G. Fontaine, R. Frey, R. Frhwirth, J. Garvey, S. Geer, C. Ghesquire, P. Ghez, K. L. Giboni, W. R. Gibson, Y. Giraud-Hraud, A. Givernaud, A. Gonidec, G. Grayer, P. Gutierrez, T. Hansl-Kozanecka, W. J. Haynes, L. O. Hertzberger, C. Hodges, D. Hoffmann, H. Hoffmann, D. J. Holthuizen, R. J. Homer, A. Honma, W. Jank, G. Jorat, P. I. P. Kalmus, V. Karimki, R. Keeler, I. Kenyon, A. Kernan, R. Kinnunen, H. Kowalski, W. Kozanecki, D. Kryn, F. Lacava, J. P. Laugier, J. P. Lees, H. Lehmann, K. Leuchs, A. Lvque, E. Linglin, E. Locci, M. Loret, J. J. Malosse, T. Markiewicz, G. Maurin, T. McMahon, J. P. Mendiburu, M. N. Minard, M. Moricca, H. Muirhead, F. Muller, A. K. Nandi, L. Naumann, A. Norton, A. Orkin-Lecourtois, L. Paoluzi, G. Petrucci, G. P. Mortari, M. Pimi, A. Placci, E. Radermacher, J. Ransdell, H. Reithler, J. P. Revol, J. Rich, M. Rijssenbeek, C. Roberts, J. Rohlf, P. Rossi, C. Rubbia, B. Sadoulet, G. Sajot, G. Salvi, J. Salvini, J. Sass, A. Saudraix, A. Savoy-Navarro, D. Schinzel, W. Scott, T. P. Shah, M. Spiro, J. Strauss, K. Sumorok, F. Szoncso, D. Smith, C. Tao, G. Thompson, J. Timmer, E. Tscheslog, J. Tuominiemi, S. V. der Meer, J. P. Vialle, J. Vrana, V. Vuillemin, H. D. Wahl, P. Watkins, J. Wilson, Y. G. Xie, M. Yvert and E. Zurfluh, Physics Letters B **122**, 103 (1983).

[14] G. Arnison, A. Astbury, B. Aubert, C. Bacci, G. Bauer, A. Bzaguet, R. Bck, T. J. V. Bowcock, M. Calvetti, P. Catz, P. Cennini, S. Centro, F. Ceradini, S. Cittolin, D. Cline, C. Cochet, J. Colas, M. Corden, D. Dallman, D. Dau, M. DeBeer, M. D. Negra, M. Demoulin, D. Denegri, A. D. Ciaccio, D. Dibitonto, L. Dobrzynski, J. D. Dowell, K. Eggert, E. Eisenhandler, N. Ellis, P. Erhard, H. Faissner, M. Fincke, G. Fontaine, R. Frey, R. Frhwirth, J. Garvey, S. Geer, C. Ghesquire, P. Ghez, K. Giboni, W. R. Gibson, Y. Giraud-Hraud, A. Givernaud, A. Gonidec, G. Grayer, T. Hansl-Kozaaecka, W. J. Haynes, L. O. Hertzberger, C. Hodges, D. Hoffmann, H. Hoffmann, D. J. Holthuizen, R. J. Homer, A. Honma, W. Jank, G. Jorat, P. I. P. Kalmus, V. Karimki, R. Keeler, I. Kenyon, A. Kernan, R. Kinnunen, W. Kozanecki, D. Kryn, F. Lacava, J. P. Laugier, J. P. Lees, H. Lehmann, R. Leuchs, A. Lvque, D. Linglin, E. Locci, J. J. Malosse, T. Markiewicz, G. Maurin, T. McMahon, J. P. Mendiburu, M. N. Minard, M. Mohammadi, M. Moricca, K. Morgan, H. Muirhead, F. Muller, A. K.

Nandi, L. Naumann, A. Norton, A. Orkin-Lecourtois, L. Paoluzi, F. Pauss, G. P. Mortari, E. Pietarinen, M. Pimi, A. Placci, J. P. Porte, E. Radermacher, J. Ransdell, H. Reithler, J. P. Revol, J. Rich, M. Rijssenbeek, C. Roberts, J. Rohlf, P. Rossi, C. Rubbia, B. Sadoulet, G. Sajot, G. Salvi, G. Salvini, J. Sass, J. Saudraix, A. Savoy-Navarro, D. Schinzel, W. Scott, T. P. Shah, M. Spiro, J. Strauss, J. Streets, K. Sumorok, F. Szoncso, D. Smith, C. Tao, G. Thompson, J. Timmer, E. Tscheslog, J. Touminiemi, B. V. Eijk, J. P. Vialle, J. Vrana, V. Vuillemin, H. D. Wahl, P. Watkins, J. Wilson, C. Wulz, G. Y. Xie, M. Yvert and E. Zurfluh, Physics Letters B **126**, 398 (1983).

[15] ALEPH Collaboration, DELPHI Collaboration, L3 Collaboration, OPAL Collaboration, SLD Collaboration, LEP Electroweak Working Group and SLD Electroweak and Heavy Flavour Groups, Physics Reports **427**, 257 (2006).

[16] Z. Maki, M. Nakagawa and S. Sakata, Progress of Theoretical Physics **28**, 870 (1962).

[17] R. Davis, Jr., D. S. Harmer and K. C. Hoffman, Physical Review Letters **20**, 1205 (1968).

[18] J. N. Bahcall, N. A. Bahcall and G. Shaviv, Physical Review Letters **20**, 1209 (1968).

[19] B. Aharmim, S. N. Ahmed, A. E. Anthony, E. W. Beier, A. Bellerive, M. Bergevin, S. D. Biller, J. Boger, M. G. Boulay, M. G. Bowler, T. V. Bullard, Y. D. Chan, M. Chen, X. Chen, B. T. Cleveland, G. A. Cox, C. A. Currat, X. Dai, F. Dalnoki-Veress, H. Deng, P. J. Doe, R. S. Dosanjh, G. Doucas, C. A. Duba, F. A. Duncan, M. Dunford and J. A. Dunmore, Physical Review C **72**, 055502 (2005).

[20] J. N. Bahcall, A. M. Serenelli and S. Basu, Astrophysical Journal **621**, L85 (2005).

[21] S. Hatakeyama, T. Hara, Y. Fukuda, T. Hayakawa, K. Inoue, K. Ishihara, H. Ishino, S. Joukou, T. Kajita, S. Kasuga, Y. Koshio, T. Kumita, K. Matsumoto, M. Nakahata, K. Nakamura, K. Okumura, A. Sakai, M. Shiozawa, J. Suzuki, Y. Suzuki, T. Tomoeda, Y. Totsuka, K. S. Hirata, K. Kihara, Y. Oyama, M. Koshiba and K. Nishijima, Physical Review Letters **81**, 2016 (1998).

[22] C. Amsler, M. Doser, M. Antonelli, D. Asner, K. Babu, H. Baer, H. Band, R. Barnett, E. Bergren, J. Beringer, G. Bernardi, W. Bertl, H. Bichsel, O. Biebel, P. Bloch, E. Blucher, S. Blusk, R. Cahn, M. Carena, C. Caso, A. Ceccucci,

D. Chakraborty, M.-C. Chen, R. Chivukula, G. Cowan, O. Dahl, G. D'Ambrosio, T. Damour, A. de Gouva, T. DeGrand, B. Dobrescu, M. Drees, D. Edwards, S. Eidelman, V. Elvira, J. Erler, V. Ezhela, J. Feng, W. Fetscher, B. Fields, B. Foster, T. Gaisser, L. Garren, H.-J. Gerber, G. Gerbier, T. Gherghetta, G. Giudice, M. Goodman, C. Grab, A. Gritsan, J.-F. Grivaz, D. Groom, M. Grnewald, A. Gurtu, T. Gutsche, H. Haber, K. Hagiwara, C. Hagmann, K. Hayes, J. Hernndez-Rey, K. Hikasa, I. Hinchliffe, A. Hcker, J. Huston, P. Igo-Kemenes, J. Jackson, K. Johnson, T. Junk, D. Karlen, B. Kayser, D. Kirkby, S. Klein, I. Knowles, C. Kolda, R. Kowalewski, P. Kreitz, B. Krusche, Y. Kuyanov, Y. Kwon, O. Lahav, P. Langacker, A. Liddle, Z. Ligeti, C.-J. Lin, T. Liss, L. Littenberg, J. Liu, K. Lugovsky, S. Lugovsky, H. Mahlke, M. Mangano, T. Mannel, A. Manohar, W. Marciano, A. Martin, A. Masoni, D. Milstead, R. Miquel, K. Mnig, H. Murayama, K. Nakamura, M. Narain, P. Nason, S. Navas, P. Nevski, Y. Nir, K. Olive, L. Pape, C. Patrignani, J. Peacock, A. Piepke, G. Punzi, A. Quadt, S. Raby, G. Raffelt, B. Ratcliff, B. Renk, P. Richardson, S. Roesler, S. Rolli, A. Romaniouk, L. Rosenberg, J. Rosner, C. Sachrajda, Y. Sakai, S. Sarkar, F. Sauli, O. Schneider, D. Scott, W. Seligman, M. Shaevitz, T. Sjstrand, J. Smith, G. Smoot, S. Spanier, H. Spieler, A. Stahl, T. Stanev, S. Stone, T. Sumiyoshi, M. Tanabashi, J. Terning, M. Titov, N. Tkachenko, N. Trnqvist, D. Tovey, G. Trilling, T. Trippe, G. Valencia, K. van Bibber, M. Vincter, P. Vogel, D. Ward, T. Watari, B. Webber, G. Weiglein, J. Wells, M. Whalley, A. Wheeler, C. Wohl, L. Wolfenstein, J. Womersley, C. Woody, R. Workman, A. Yamamoto, W.-M. Yao, O. Zenin, J. Zhang, R.-Y. Zhu, P. Zyla, G. Harper, V. Lugovsky and P. Schaffner, Physics Letters B **667**, 1 (2008).

[23] N. Cabibo, Physical Review Letters **10**, 531 (1963).

[24] M. Kobayashi and T. Masakawa, Progress of Theoretical Physics **49**, 652 (1972).

[25] S. L. Glashow, J. Iliopoulos and L. Maiani, Physical Review D **2**, 1285 (1970).

[26] D. Nötzold and G. Raffelt, Nuclear Physics B **307**, 924 (1988).

[27] Y.-Z. Qian and G. Fuller, Physical Review D **51**, 1479 (1995).

[28] A. D. Dolgov, S. H. Hansen, S. Pastor, S. T. Petcov, G. G. Raffelt and D. V. Semikoz, Nuclear Physics B **632**, 363 (2002).

[29] D. Boyanovsky and C. M. Ho, Journal of High Energy Physics **07**, 30 (2007).

[30] D. Boyanovsky and C. M. Ho, Physical Review D **76**, 085011 (2007).

[31] T. Schwetz, M. Tórtola and J. W. F. Valle, New Journal of Physics **10**, 113011 (2008).

[32] M. Goodman, arXiv:0706.0512.

[33] C. Arnaboldi, D. R. Artusa, F. T. A. III, M. Balata, I. Bandac, M. Barucci, J. W. Beeman, F. Bellini, C. Brofferio, C. Bucci, S. Capelli, L. Carbone, S. Cebrian, M. Clemenza, O. Cremonesi, R. J. Creswick, A. de Waard, S. D. Domizio, M. J. Dolinski, H. A. Farach, E. Fiorini, G. Frossati, A. Giachero, A. Giuliani, P. Gorla, E. Guardincerri, T. D. Gutierrez, E. E. Haller, R. H. Maruyama, R. J. McDonald, S. Nisi, C. Nones, E. B. Norman, A. Nucciotti, E. Olivieri, M. Pallavicini, E. Palmieri, E. Pasca, M. Pavan, M. Pedretti, G. Pessina, S. Pirro, E. Previtali, L. Risegari, C. Rosenfeld, S. Sangiorgio, M. Sisti, A. R. Smith, L. Torres, G. Ventura and M. Vignati, Physical Review C **78**, 035502 (2008).

[34] E. W. Otten and C. Weinheimer, Reports on Progress in Physics **71**, 086201 (2008).

[35] E. Komatsu, J. Dunkley, M. R. Nolta, C. L. Bennett, B. Gold, G. Hinshaw, N. Jarosik, D. Larson, M. Limon, L. Page, D. N. Spergel, M. Halpern, R. S. Hill, A. Kogut, S. S. Meyer, G. S. Tucker, J. L. Weiland, E. Wollack and E. L. Wright, Astrophysical Journal Supplement Series **180**, 330 (2009).

[36] H. Duan, G. M. Fuller, J. Carlson and Y.-Z. Qian, Physical Review Letters **99**, 241802 (2007).

[37] C. Lunardini and A. Y. Smirnov, Journal of Cosmology and Astroparticle Physics **0306**, 009 (2007).

[38] K. Eitel, New Journal of Physics **2**, 1 (2000).

[39] A. A. Aguilar-Arevalo, C. E. Anderson, S. J. Brice, B. C. Brown, L. Bugel, J. M. Conrad, Z. Djurcic, B. T. Fleming, R. Ford, F. G. Garcia, G. T. Garvey, J. Gonzales, J. Grange, C. Green, J. A. Green, R. Imlay, R. A. Johnson, G. Karagiorgi, T. Katori, T. Kobilarcik, S. K. Linden, W. C. Louis, K. B. M. Mahn, W. Marsh, C. Mauger, V. T. McGary, W. Metcalf, G. B. Mills, C. D. Moore, J. Mousseau, R. H. Nelson, P. Nienaber, J. A. Nowak, B. Osmanov, Z. Pavlovic, D. Perevalov, C. C. Polly, H. Ray, B. P. Roe, A. D. Russell, M. H. Shaevitz, M. Sorel, J. Spitz, I. Stancu, R. J. Stefanski, R. Tayloe, M. Tzanov, R. G. Van de Water, M. O. Wascko, D. H. White, M. J. Wilking, G. P. Zeller and E. D. Zimmerman, arXiv:0904.1958.

[40] M. Shaposhnikov and I. Tkachev, Physics Letters B **639**, 414 (2006).

[41] A. Kusenko, Physical Review Letters **97**, 241301 (2006).

[42] K. Kadota, Physical Review D **77**, 063509 (2008).

[43] K. Petraki and A. Kusenko, Physical Review D **77**, 065014 (2008).

[44] B. Pontecorvo, Soviet Physics Journal of Experimental and Theoretical Physics **26**, 984 (1968).

[45] A. Kusenko and G. Segré, Physics Letters B **396**, 197 (1997).

[46] J. Hidaka and G. M. Fuller, Physical Review D **74**, 125015 (2006).

[47] J. Hidaka and G. M. Fuller, Physical Review D **76**, 083516 (2007).

[48] J. R. Wilson, G. J. Mathews and G. M. Fuller, Physical Review D **75**, 043521 (2007).

[49] S. Dodelson and L. M. Widrow, Physical Review Letters **72**, 17 (1994).

[50] K. Abazajian, G. M. Fuller and M. Patel, Physical Review D **64**, 023501 (2001).

[51] C. T. Kishimoto and G. M. Fuller, Physical Review D **78**, 023524 (2008).

[52] S. P. Mikheyev and A. Y. Smirnov, Yadernaya Fizika **42**, 1441 (1985).

[53] L. Wolfenstein, Physical Review D **17**, 2369 (1978).

[54] K. Abazajian, N. F. Bell, G. M. Fuller and Y. Y. Y. Wong, Physical Review D **72**, 063004 (2005).

[55] S. J. Parke, Physical Review Letters **57**, 1275 (1986).

[56] L. D. Landau, Physikalische Zeitschrift der Sowjetunion **2**, 46 (1932).

[57] C. Zener, Proceedings of the Royal Society of London Series A **137**, 696 (1932).

[58] W. C. Haxton, Physical Review D **35**, 2352 (1987).

[59] T. K. Kuo and J. Pantaleone, Physical Review D **39**, 1930 (1989).

[60] A. Halprin, Physical Review D **34**, 3462 (1986).

[61] B. H. J. McKellar and M. J. Thomson, Physical Review D **49**, 2710 (1994).

[62] G. Sigl and G. Raffelt, Nuclear Physics B **406**, 423 (1993).

[63] N. F. Bell, R. R. Volkas and Y. Y. Y. Wong, Physical Review D **59**, 113001 (1999).

[64] B. Misra and E. C. G. Sudarshan, Journal of Mathematical Physics **18**, 756 (1977).

[65] R. Foot and R. R. Volkas, Physical Review D **55**, 5147 (1997).

[66] S. Weinberg, *Gravitation and Cosmology: Principles and Applications of the General Theory of Relativity* (Wiley, New York, 1972).

[67] A. Friedman, Zeitschrift für Physik A **10**, 377 (1922).

[68] G. Lemaître, Monthly Notices of the Royal Astronomical Society **91**, 483 (1931).

[69] H. P. Robertson, Astrophysical Journal **82**, 284 (1935).

[70] A. G. Walker, Proceedings of the London Mathematical Society 2 **42**, 90 (1937).

[71] F. Zwicky, Helvetica Physica Acta **6**, 110 (1933).

[72] G. M. Fuller and C. T. Kishimoto, arXiv:0811.4370.

[73] C. Bernard, T. Burch, C. DeTar, J. Osborn, S. Gottlieb, E. B. Gregory, D. Toussaint, U. M. Heller and R. Sugar, Physical Review D **71**, 034504 (2005).

[74] E. Hubble, Proceedings of the National Academy of Sciences of the United States of America **15**, 168 (1929).

[75] A. H. Guth, Physical Review D **23**, 347 (1981).

[76] A. D. Linde, Physics Letters B **108**, 389 (1982).

[77] A. Albrecht and P. J. Steinhardt, Physical Review Letters **48**, 1220 (1982).

[78] S. Hannestad, Physical Review D **70**, 043506 (2004).

[79] E. W. Kolb and M. S. Turner, *The Early Universe* (Addison-Wesley, 1990).

[80] M. Laine and K. Rummukainen, Nuclear Physics B **535**, 423 (1998).

[81] B. Bergerhoff and C. Wetterich, hep-ph/9611462.

[82] D. Boyanovsky, H. J. de Vega and D. J. Schwarz, Annual Review of Nuclear and Particle Science **56**, 441 (2006).

[83] A. Bessa, E. S. Fraga and B. W. Mintz, Physical Review D **79**, 034012 (2009).

[84] K. N. Abazajian and G. M. Fuller, Physical Review D **66**, 023526 (2002).

[85] A. D. Dolgov, Physics Reports **370**, 333 (2002).

[86] G. Mangano, G. Miele, S. Pastor, T. Pinto, O. Pisanti and P. D. Serpico, Nuclear Physics B **729**, 221 (2005).

[87] C. J. Smith, G. M. Fuller and M. S. Smith, arXiv:0812.1253.

[88] C. J. Smith, G. M. Fuller, C. T. Kishimoto and K. N. Abazajian, Physical Review D **74**, 085008 (2006).

[89] K. A. Olive, G. Steigman and E. D. Skillman, Astrophysical Journal **483**, 788 (1997).

[90] Y. I. Izotov and T. X. Thuan, Astrophysical Journal **602**, 200 (2004).

[91] K. A. Olive and E. D. Skillman, Astrophysical Journal **617**, 29 (2004).

[92] D. Kirkman, D. Tytler, N. Suzuki, J. M. O'Meara and D. Lubin, Astrophysical Journal Supplement Series **149**, 1 (2003).

[93] J. M. O'Meara, D. Tytler, D. Kirkman, N. Suzuki, J. X. Prochaska, D. Lubin and A. M. Wolfe, Astrophysical Journal **552**, 718 (2001).

[94] S. Burles, K. M. Nollett and M. S. Turner, Astrophysical Journal **552**, L1 (2001).

[95] R. H. Cyburt, B. D. Field and K. A. Olive, Physics Letters B **567**, 227 (2003).

[96] A. A. Penzias and R. W. Wilson, Astrophysical Journal **165**, 419 (1965).

[97] C. L. Bennett, A. J. Banday, K. M. Górski, G. Hinshaw, P. Jackson, P. Keegstra, A. Kogut, G. F. Smoot, D. T. Wilkinson and E. L. Wright, Astrophysical Journal **464**, L1 (1996).

Chapter 2

Coherent Active-Sterile Neutrino Flavor Transformation in the Early Universe

2.1 Abstract

We solve the problem of coherent Mikheyev-Smirnov-Wolfenstein (MSW) resonant active-to-sterile neutrino flavor conversion driven by an initial lepton number in the early universe. We find incomplete destruction of lepton number in this process and a sterile neutrino energy distribution with a distinctive cusp and high energy tail. These features imply alteration of the non-zero lepton number primordial nucleosynthesis paradigm when there exist sterile neutrinos with rest masses $m_{\rm s} \sim 1\,{\rm eV}$. This could result in better light element probes of (constraints on) these particles.

2.2 Introduction

Recent advances in observational cosmology and in experimental neutrino physics promise a well constrained picture for the evolution of the early universe. The existence of a light sterile neutrino (ν_s) presents an immediate problem: how do sterile neutrinos affect primordial seas of active neutrinos ν_α or $\bar{\nu}_\alpha$ ($\alpha = e, \mu, \tau$) and consequentially affect the standard big bang paradigm? In this chapter we study the lepton number-driven transformation of active neutrinos to sterile neutrinos in the epoch of the early universe after weak decoupling, when neutrinos propagate coherently. This process could leave both the active neutrinos and sterile neutrinos with distorted, non-thermal energy spectra [1].

A non-thermal ν_e or $\bar{\nu}_e$ spectrum could lead to significant modification in the relationship between lepton number and Big Bang Nucleosynthesis (BBN) ^{4}He abundance yield [1, 2]. Concomitantly, a distorted ν_s distribution function changes closure mass constraints on light sterile neutrinos [1, 3], allowing rest masses and vacuum mixing angles for these species in the range ($0.4\,\mathrm{eV} < m_\mathrm{s} < 5\,\mathrm{eV}$) suggested by the LSND experiment [4, 5] and probed by the mini-BooNE experiment [6]. While the results of the mini-BooNE experiment has since refuted the LSND results [7], there remains a significant unconstrained parameter space in this mass range.

Section 2.3 describes a mechanism for populating ν_s states through lepton number-driven coherent $\nu_\alpha \rightarrow \nu_e$ transformation. Section 2.4 outlines the effects of a lepton number and the distorted ν_e spectrum on BBN predictions of the primordial ^{4}He abundance.

2.3 Resonance Sweep in the Early Universe

Active neutrinos propagating in the homogeneous early universe experience a potential stemming from forward scattering

$$V = 2\sqrt{2}\zeta(3)\pi^{-2}G_F T^3 \mathcal{L}_\alpha - r_\alpha G_F^2 E_\nu T^4, \tag{2.1}$$

where T is the photon/plasma temperature, E_ν is the neutrino energy, r_α is a numerical coefficient which depends on the number of relativistic charged lepton degrees of freedom and can be found in Refs. [1, 8], G_F is the Fermi constant, and

$\zeta\,(3) \approx 1.202\,06$. Here the potential lepton number is

$$\mathcal{L}_\alpha \equiv 2L_{\nu_\alpha} + \sum_{\beta\neq\alpha} L_{\nu_\beta}, \tag{2.2}$$

where the individual lepton numbers are given in terms of the neutrino, antineutrino, and photon proper number densities by $L_{\nu_\alpha} \equiv (n_{\nu_\alpha} - n_{\bar{\nu}_\alpha})/n_\gamma$. Current observational bounds on these are $|L_{\nu_\alpha}| < 0.1$ [9–11], and could be slightly weaker if there are additional sources of energy density in the early universe [12, 13]. We have neglected contributions to V from neutrino-baryon/electron scattering since we consider relatively large lepton numbers with $\mathcal{L} \gg \eta$, where the baryon-to-photon ratio is $\eta \equiv n_\mathrm{b}/n_\gamma$ (see Refs. [1, 8]). The second term in V is negligible for the temperatures characteristic of the post weak decoupling era, $T < 3\,\mathrm{MeV}$.

The scattering-induced de-coherence production [14–19] of seas of ν_s and $\bar{\nu}_s$, with rest mass $m_\mathrm{s} \sim 1\,\mathrm{eV}$, could be avoided if theses species are massless for $T > 3\,\mathrm{MeV}$, inflation has a low reheat temperature [20], or there exists a preexisting lepton number $|L_{\nu_\alpha}| > 10^{-3}$ [1, 21]. However, a lepton number could subsequently, after weak decoupling, drive [1] coherent medium-enhanced MSW [22, 23] resonant conversion $\nu_\alpha \longrightarrow \nu_s$ or $\bar{\nu}_\alpha \longrightarrow \bar{\nu}_s$, depending on the sign of the lepton number. (Resonant de-coherence production of sterile neutrinos with $m_\mathrm{s} \sim 1\,\mathrm{keV}$ with accompanying ν_s spectral distortion was considered in Refs. [8, 24].) The MSW condition for the resonant scaled neutrino energy $\epsilon = E_\nu^\mathrm{res}/T$ is $\delta m^2 \cos 2\theta = 2\epsilon T V$, or

$$\epsilon\mathcal{L} = \left(\frac{\delta m^2 \cos 2\theta}{4\sqrt{2}\zeta(3)\pi^{-2}G_F}\right) T^{-4}, \tag{2.3}$$

where $\delta m^2 \equiv m_2^2 - m_1^2$ is the difference of the squares of the vacuum neutrino mass eigenvalues. For illustrative purposes, we consider 2×2 vacuum mixing with a one-parameter (vacuum mixing angle θ) unitary transformation between weak interaction eigenstates $|\nu_\alpha\rangle$, $|\nu_s\rangle$, and energy/mass eigenstates:

$$\begin{aligned} |\nu_\alpha\rangle &= \cos\theta|\nu_1\rangle + \sin\theta|\nu_2\rangle; \\ |\nu_s\rangle &= -\sin\theta|\nu_1\rangle + \cos\theta|\nu_2\rangle. \end{aligned} \tag{2.4}$$

As the universe expands, the temperature falls, causing the resonance to sweep from low to higher values of the scaled neutrino energy, ϵ. This resonance sweep converts active neutrinos into sterile neutrinos, reducing $\mathcal{L}$, which accelerates the resonance sweep rate. Since the resonant value of the neutrino scaled energy increases monotonically with time, we can use ϵ as a time-like variable in describing the evolution of the neutrino distribution functions.

The evolution of $\mathcal{L}$ is dictated by the resonance sweep rate and the dimensionless adiabaticity parameter. The adiabaticity parameter, γ, is proportional to the ratio of the width of the MSW resonance, $\delta t = |1/V dV/dt|^{-1} \tan 2\theta$, and the neutrino oscillation length at resonance, $L_{\text{osc}} = 4\pi E_\nu/(\delta m^2 \sin 2\theta)$. Combining the expansion rate of the universe in the radiation dominated epoch with the conservation of co-moving entropy density and the forward scattering potential V, the adiabaticity parameter is

$$\gamma \approx \frac{\sqrt{5}\zeta^{3/4}(3)}{2^{1/8}\pi^3} \frac{(\delta m^2)^{1/4} m_{pl} G_F^{3/4}}{g^{1/2}} \frac{\sin^2 2\theta}{\cos^{7/4} 2\theta} \mathcal{L}^{3/4} \epsilon^{-1/4} \left| 1 + \frac{\dot{g}/g}{3H} - \frac{\dot{\mathcal{L}}/\mathcal{L}}{3H} \right|^{-1}, \tag{2.5}$$

where m_{pl} is the Planck mass, g is the total statistical weight for relativistic species in the early universe, and

$$H \approx \left(\frac{4\pi^3}{45} \right)^{1/2} g^{1/2} \frac{T^2}{m_{pl}} \tag{2.6}$$

is the local Hubble expansion rate. If the onset of resonant flavor conversion occurs in the epoch between weak decoupling and weak freeze out, then initially $\gamma \gg 1$ for the active-sterile mixing parameters of interest [1]. However, when the fractional time rate of change of $\mathcal{L}$ becomes larger than the expansion rate of the universe, the evolution of the system can be non-adiabatic with $\gamma < 1$.

Large values of γ result when many oscillation lengths fit within the resonance width. In this case there will be a small probability of jumping from the high mass eigenstate to the low mass eigenstate. In turn, this implies efficient flavor transformation at the MSW resonance. Alternatively, a small value of γ means that the resonance width is much smaller than an oscillation length, and the neutrino jumps between the two mass eigenstates, resulting in virtually no flavor transformation. To describe intermediate cases we use the Landau-Zener jump probability, $P_{\mathrm{LZ}} = \exp(-\pi\gamma/2)$ [25, 26], which gives the likelihood for a neutrino at resonance to make the jump between mass eigenstates. It is valid in the limit where the change in V across the resonance width δt can be regarded as linear. This is a good approximation in part because the resonance width is small compared to the causal horizon length for the values of θ and the conditions in the early universe considered here.

It follows that the evolution of the potential lepton number as the resonant scaled neutrino energy sweeps from 0 to ϵ is

$$\mathcal{L}(\epsilon) = \mathcal{L}^{\mathrm{initial}} - \frac{1}{2\zeta(3)}\left(\frac{T_\nu}{T}\right)^3 \int_0^\epsilon \frac{x^2(1-e^{-\pi\gamma(x)/2})}{e^{x-\eta_{\nu_\alpha}}+1}dx, \tag{2.7}$$

where T_ν is the temperature of the active neutrino distribution function with degeneracy parameter $\eta_{\nu_\alpha} \equiv \mu_{\nu_\alpha}/T_\nu$, and where μ_{ν_α} is the ν_α chemical potential.

The evolution of the active neutrino spectrum is dictated by three conspiring factors: the MSW resonance condition (Eq. 2.3), the adiabaticity parameter (Eq. 2.5), and the evolution of potential lepton numbers through active-sterile conversion (Eq. 2.7). We solve Eqs. (2.3), (2.5) and (2.7) simultaneously and self-consistently to obtain γ and $\mathcal{L}$ as continuous functions across the entire range of ϵ.

Resonant conversion of active neutrinos to sterile neutrinos begins at $\epsilon \ll 1$. The resonance sweeps to higher values of ϵ as the temperature of the universe drops. When $\dot{\mathcal{L}}/\mathcal{L} \ll H$, we have $\gamma \gg 1$, and adiabatic conversion of active neutrinos to sterile neutrinos ensues. However, this trend cannot continue. Note that the right hand side of equation (2.3) is a monotonically increasing function of time, while the left hand side is a peaked function if one assumes continued adiabatic conversion of neutrino flavors. At this peak, this assumption fails. Taking the time derivative of the resonance condition, Eq. (2.3), shows that the sweep rate is $\dot{\epsilon} \propto T^{-5}\dot{T}(d(\epsilon\mathcal{L})/d\epsilon)^{-1}$. At the peak, $d(\epsilon\mathcal{L})/d\epsilon = 0$, causing the sweep rate to diverge. Taking the time derivative of both sides of Eq. (2.7) and assuming that T_ν/T is constant, we conclude that $\dot{\mathcal{L}} \propto \dot{\epsilon}$. With this relation, it follows from equation (2.5) that the MSW resonance is no longer adiabatic. We define $\epsilon_{\max}$ as the particular value of ϵ at this peak,

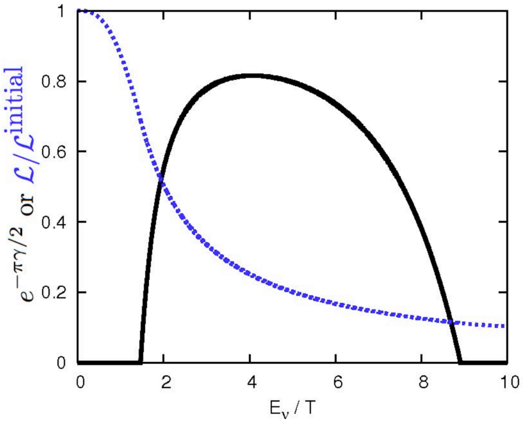

Figure 2.1: Landau-Zener jump probability $e^{-\pi\gamma/2}$ (solid curve) and potential lepton number given as a fraction of its initial value (dashed curve) are shown as a function of MSW scaled resonance energy E_ν/T. Here we assume $\delta m^2 = 1\,\mathrm{eV}^2$, $\sin^2 2\theta = 10^{-3}$, and initial individual lepton numbers $L_{\nu_\mu} = L_{\nu_\tau} = 0.15$ and $L_{\nu_e} = 0.0343$.

implicitly specified by

$$\frac{1}{2\zeta(3)}\frac{\epsilon_{\rm max}^3}{e^{\epsilon_{\rm max}-\eta_{\nu_\alpha}}+1} = \mathcal{L}^{\rm initial} - \frac{1}{2\zeta(3)}\left(\frac{T_\nu}{T}\right)^3 \int_0^{\epsilon_{\rm max}} \frac{x^2}{e^{x-\eta_{\nu_\alpha}}+1}dx. \tag{2.8}$$

Our complete continuous solution for γ shows that neutrino flavor evolution / transformation is adiabatic for $\epsilon < \epsilon_{\rm max}$, but becomes (quickly) progressively less adiabatic for $\epsilon > \epsilon_{\rm max}$. For $\epsilon \geq \epsilon_{\rm max}$, our solution yields a large, but finite resonance sweep rate, and concomitant large fractional lepton number destruction rate, $\dot{\mathcal{L}}/\mathcal{L} \gg H$, leading to $\gamma \lesssim 1$. This behavior continues through the heart of the active neutrino distribution until the resonance sweep rate decreases to a point where $\gamma \gg 1$ again. This last transition back to adiabatic evolution occurs at $\epsilon = \epsilon_f \sim \mathcal{O}(10)$, approximately where $\mathcal{L}(\epsilon_f) = 1/(2\zeta(3))\epsilon_f^3/(e^{\epsilon_f-\eta_{\nu_\alpha}}+1)$. (Note that this is the same condition as for $\epsilon_{\rm max}$.) Resonance sweep continues to higher ϵ, adiabatically converting active neutrinos to sterile neutrinos.

The evolution of the Landau-Zener jump probability $e^{-\pi\gamma/2}$ and the history of the potential lepton number as a fraction of its initial value are both shown in Figure 2.1 for the particular case where $\delta m^2 = 1\,\mathrm{eV}^2$, $\sin^2 2\theta = 10^{-3}$, and where we

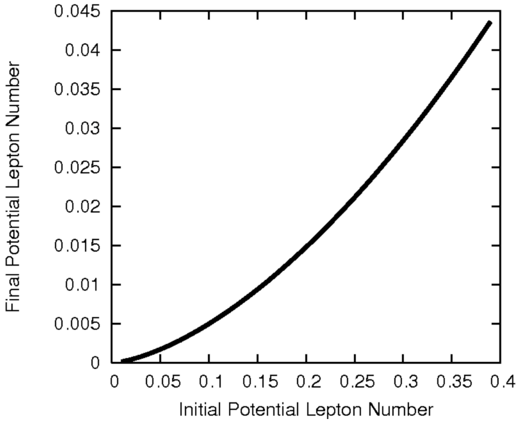

Figure 2.2: Final potential lepton number as a function of its initial value is shown for the case where all individual initial lepton numbers are equal $L_{\nu_e} = L_{\nu_\mu} = L_{\nu_\tau}$ and the active-sterile vacuum mixing parameters are as in Fig. 2.1

assume initial lepton numbers near their conventional upper limits, $L_{\nu_\mu} = L_{\nu_\tau} = 0.15$ and $L_{\nu_e} = 0.0343$. For this particular case $\epsilon_{\max} = 1.46$, and Figure 2.1 shows the rather abrupt (but continuous) change to non-adiabatic evolution for $\epsilon \approx \epsilon_{\max}$. In this example, the final transition back to adiabatic evolution occurs at $\epsilon_f \approx 8.9$. Altogether, more than 90% of the initial potential lepton number is destroyed for this case. We find that the fractional depletion of potential lepton number is $\sim 90\%$ across a wide range of initial values of this parameter. This, in turn, suggests that this new solution will result in little change in existing closure mass constraints on light sterile neutrinos [1]. Figure 2.2 shows the final potential lepton number as a function of its initial value for the same active-sterile vacuum mixing parameters but for the case where all initial individual lepton numbers are equal.

Figure 2.3 shows the original ν_e Fermi-Dirac energy distribution,

$$f(E_\nu/T_\nu) = \frac{1}{T_\nu^2 F_2(\eta_\nu)} \frac{E_\nu^2}{e^{E_\nu/T_\nu - \eta_\nu} + 1}, \tag{2.9}$$

where $F_2(\eta_\nu) \equiv \int_0^\infty x^2/(e^{x-\eta_\nu}+1)dx$, and final ν_e and the ν_s energy distribution functions resulting from $\nu_e \rightarrow \nu_s$ resonance sweep for the example parameters of Fig. 2.1. Forced, adiabatic resonance sweep to $\epsilon_{\text{c.o.}}$ would result in complete depletion of

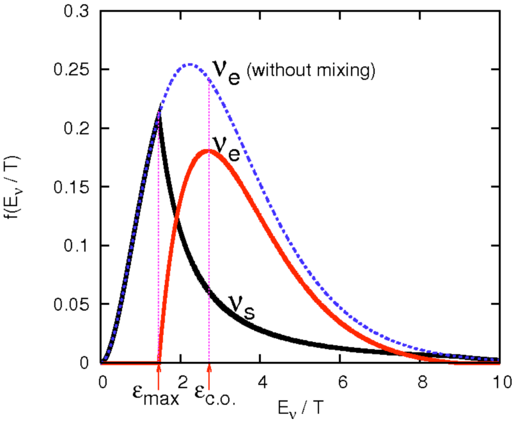

Figure 2.3: Shown are the original ν_e distribution function (dashed curve), the final ν_e distribution function (lighter solid curve), and final ν_s distribution function (heavier solid curve) all as functions of scaled neutrino energy E_ν/T for a $\nu_e \rightarrow \nu_s$ resonant, coherent flavor conversion process with $\delta m^2 = 1\,\mathrm{eV}^2$, $\sin^2 2\theta = 10^{-3}$, and individual lepton numbers as in Fig. 2.1. Vertical dotted lines indicate ϵ_{max} and $\epsilon_{\mathrm{c.o.}}$.

the initial potential lepton number. ϵ_{max} and $\epsilon_{\mathrm{c.o.}}$ are shown for this case in Fig. 2.3. Forced, adiabatic resonance sweep would result in a final ν_e spectrum identical to the initial one except cut-off (hence, "c.o."), with zero population, for $E_\nu/T \leq \epsilon_{\mathrm{c.o.}}$. The ν_s distribution in this case would be simply the complement. By contrast, with the full resonance sweep solution presented here we see that the actual final ν_e spectrum has a population deficit relative to the original distribution, even for $E_\nu/T > \epsilon_{\mathrm{c.o.}}$. Likewise, the actual final ν_s spectrum will now have a tail extending to higher E_ν/T. Including simultaneous active-sterile and active-active neutrino flavor transformation in a full 4×4 scheme will modify this result, but we can expect some general features of our solution to remain. In particular, although neutrino flavor evolution will start out adiabatic, the transition to non-adiabatic evolution could be altered by, *e.g.*, active-active neutrino mixing partially "filling-in" depleted ν_e population [1].

It is useful to have an analytic expression for the ν_e distribution function as a function of temperature T. For $T > T_{\mathrm{max}}$, where T_{max} is defined by Eqn. (2.3) with

$\epsilon = \epsilon_{\max}$ and $\mathcal{L} = \mathcal{L}(\epsilon_{\max})$,

$$f_{\nu_e}(\epsilon) = \begin{cases} 0 & \epsilon \leq \epsilon_{\text{res}}(T) \\ f_\nu(\epsilon) & \epsilon > \epsilon_{\text{res}}(T) \end{cases} , \tag{2.10}$$

where $\epsilon_{\text{res}}(T)$ is the solution of Eqn. (2.3). For $T < T_{\max}$,

$$f_{\nu_e}(\epsilon) \approx \begin{cases} 0 & \epsilon \leq \epsilon_{\max} \\ f_\nu(\epsilon) - \frac{2\zeta(3)}{F_2(\eta_\nu)} \left(\frac{T}{T_\nu}\right)^3 \frac{\epsilon_{\max}\mathcal{L}_{\max}}{\epsilon^2} & \epsilon_{\max} < \epsilon < \epsilon_f \\ 0 & \epsilon_f < \epsilon < \epsilon_{\text{res}}(T) \\ f_{\nu_e}(\epsilon) & \epsilon > \epsilon_{\text{res}}(T) \end{cases} . \tag{2.11}$$

At early times (or equivalently, large T), the resonance sweeps through the ν_e energy distribution efficiently converting $\nu_e \rightarrow \nu_s$. Once $T = T_{\max}$, the resonance sweeps nearly instantaneously through the heart of the ν_e energy distribution, converting $\nu_e \rightarrow \nu_s$, albeit at a reduced efficiency $(1 - e^{-\pi\gamma/2})$. The sweep then continues at large values of ϵ, efficiently converting $\nu_e \rightarrow \nu_s$.

2.4 Big Bang Nucleosynthesis Concerns

The BBN ^{4}He yield can depend sensitively on the shape of the ν_e energy distribution function [1, 27, 28]. This is because the neutron-to-proton ratio n/p is a crucial determinant of the ^{4}He abundance and, in turn, this ratio is set by the competition among the charged current weak neutron/proton interconversion processes:

$$\begin{aligned} \nu_e + n &\rightleftharpoons p + e^-; \\ \bar{\nu}_e + p &\rightleftharpoons n + e^+; \\ n &\rightleftharpoons p + e^- + \bar{\nu}_e. \end{aligned} \tag{2.12}$$

The net rate for the forward direction in the first of these processes will be reduced if ν_e-population is removed via $\nu_e \rightarrow \nu_s$, resulting in a larger n/p and, hence, a larger ^{4}He yield. Likewise, a negative potential lepton number-driven $\bar{\nu}_e \rightarrow \bar{\nu}_s$ scenario

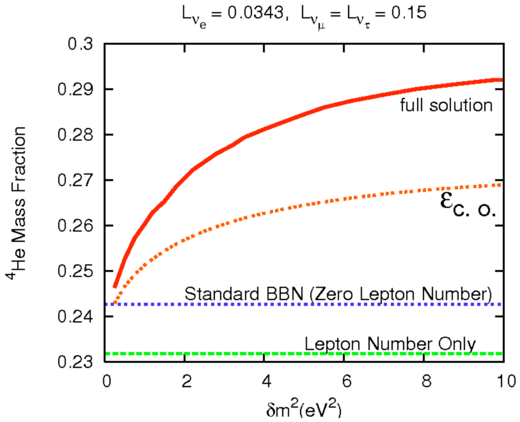

Figure 2.4: Primordial nucleosynthesis (BBN) ^{4}He abundance yield as a function of δm^2 for the $\nu_e \rightarrow \nu_s$ channel and the indicated initial individual lepton numbers (same as in Fig. 2.1). Standard BBN (zero lepton numbers, no sterile neutrinos) is the heavy dashed horizontal line. The case for BBN with the indicated lepton number, but no active-sterile mixing is the light dashed horizontal line. The case for forced, adiabatic resonance sweep to $\epsilon_{\text{c.o.}}$ is the light dotted line. The full non-adiabatic solution is given by the heavy solid line.

could result in $\bar{\nu}_e$ spectral depletion which will result in a smaller n/p and, hence, less ^{4}He. Removing ν_e ($\bar{\nu}_e$) population at higher E_ν/T values in the energy distribution function accentuates these effects because the cross section for the ν_e ($\bar{\nu}_e$) capture process scales as E_ν^2 and because the Fermi-Dirac spectral peak, where neutrino populations are large, corresponds to values of neutrino energy satisfying $E_\nu/T > \epsilon_{\text{c.o.}}$ for the potential lepton numbers $\mathcal{L}$ of interest here. As a consequence, our full resonance sweep scenario can result in significant alteration in ^{4}He yield over the forced, adiabatic scenario.

We have computed the BBN ^{4}He abundance yield with a version of the Kawano-Wagoner-Fowler-Hoyle code [29, 30] modified to allow for dynamic alteration/distortion in the neutrino energy distribution functions. The results of these calculations for the initial lepton numbers adopted in the example of Fig. 2.1 are shown in Figure 2.4. The standard (zero lepton number, no sterile neutrinos) BBN ^{4}He abundance yield mass fraction is $\approx 24\%$ when we adopt neutron lifetime $\tau_n = 887.8\,\text{s}$ and

$\eta = 6.1102 \times 10^{-10}$. The adopted value of η corresponds to the central value of the cosmic microwave background radiation acoustic peak-determined WMAP 3-year data, $\eta = (6.11 \pm 0.22) \times 10^{-10}$ [31]. The observational error in η corresponds to a $\pm 0.03\%$ range in the calculated ^{4}He abundance yield.

Alternatively, the case with the example lepton numbers but with no active-sterile neutrino mixing gives a healthy ^{4}He yield suppression. However, once the spectral distortion is included the ^{4}He yield is larger than in standard BBN. Given that the observationally-inferred helium abundance is between $23\% - 26\%$ [32] (and possibly more precisely determined [33, 34]), we see that the dramatically larger ^{4}He yield in the cases with ν_e spectral distortion may allow for new constraints on a combination of lepton number and sterile neutrino masses. Our resonance sweep solution gives a larger ^{4}He yield than in previous models of active-sterile neutrino transformation which employ, *e.g.*, forced, adiabatic resonance sweep to $\epsilon_{\text{c.o.}}$ [1]. This shows the sensitivity of BBN abundance yields to sterile neutrino-induced active neutrino spectral distortion. This effect eventually may allow light element probes/constraints on the sterile neutrino sector which complement those of mini-BooNE and may extend to sterile neutrino mass/mixing parameters currently inaccessible experimentally.

We would like to thank K. Abazajian, N. Bell, M. Smith, and especially M. Patel for insightful discussions. This work was supported in part by NSF Grant PHY-04-00359 at UCSD. C.T.K. would like to acknowledge a fellowship from the ARCS Foundation, Inc.

Chapter 2, in part, is a reprint of material previously published as C. T. Kishimoto, G. M. Fuller, and C. J. Smith, “Coherent Active-Sterile Neutrino Flavor Transformation in the Early Universe”, *Physical Review Letters* **97**, 141301 (2006). I was the primary investigator and author of this paper.

Bibliography

[1] K. Abazajian, N. F. Bell, G. M. Fuller and Y. Y. Y. Wong, Physical Review D **72**, 063004 (2005).

[2] G. Mangano, G. Miele, S. Pastor, T. Pinto, O. Pisanti and P. D. Serpico, Nuclear Physics B **729**, 221 (2005).

[3] S. Dodelson, A. Melchiorri and A. Slosar, Physical Review Letters **97**, 041301 (2006).

[4] K. Eitel, New Journal of Physics **2**, 1 (2000).

[5] C. Athanassopoulos, L. B. Auerbach, D. A. Bauer, R. D. Bolton, B. Boyd, R. L. Burman, D. O. Caldwell, I. Cohen, B. D. Dieterle, J. B. Donahue, A. M. Eisner, A. Fazely, F. J. Federspiel, G. T. Garvey, M. Gray, W. Metcalf, R. A. Reeder, V. Sandberg, M. Schillaci, D. Smith, I. Stancu, W. Strossman, M. K. Sulliban, G. J. VanDalen, W. Vernon, Y. Wang, D. H. White, D. Whitehouse, D. Works, Y. Xiao and S. Yellin, Physical Review Letters **75**, 2650 (1995).

[6] G. McGregor, The miniboone experiment: Status and plans, in *Particle Physics and Cosmology: Third Tropical Workshop on Particle Physics and Cosmology - Neutrinos, Branes, and Cosmology*, edited by J. F. Nieves and C. N. Leung, AIP Conference Proceedings No. 655, p. 58, New York, 2003, AIP.

[7] A. A. Aguilar-Arevalo, A. O. Bazarko, S. J. Brice, B. C. Brown, L. Bugel, J. Cao, L. Coney, J. M. Conrad, D. C. Cox, A. Curioni, Z. Djurcic, D. A. Finley, B. T. Fleming, R. Ford, F. G. Garcia, G. T. Garvey, C. Green, J. A. Green, T. L. Hart, E. Hawker, R. Imlay, R. A. Johnson, P. Kasper, T. Katori, T. Kobilarcik, I. Kourbanis, S. Koutsoliotas, E. M. Laird, J. M. Link, Y. Liu, Y. Lie, W. C. Louis, K. B. M. Mahn, W. Marsh, P. S. Martin, G. McGregor, W. Metcalf, P. D. Meyers, F. Mills, G. B. Mills, J. Monroe, C. D. Moore, R. H. Nelson, P. Nienaber, S. Ouedraogo, R. B. Patterson, D. Perevalov, C. C. Polly, E. Prebys, J. L. Raaf, H. Ray, B. P. Roe, A. D. Russell, V. Sandberg, R. Schirato, D. Schmitz, M. H. Shaevitz, F. C. Shoemaker, D. Smith, M. Sorel, P. Spentzouris, I. Stancu, R. J.

Stefanski, M. Sung, H. A. Tanaka, R. Tayloe, M. Tzanov, R. Van de Water, M. O. Wascko, D. H. White, M. J. Wilking, H. J. Yang, G. P. Zeller and E. D. Zimmerman, Physical Review Letters **97**, 231801 (2007).

[8] K. Abazajian, G. M. Fuller and M. Patel, Physical Review D **64**, 023501 (2001).

[9] A. D. Dolgov, S. H. Hansen, S. Pastor, S. T. Petcov, G. G. Raffelt and D. V. Semikoz, Nuclear Physics B **632**, 363 (2002).

[10] K. N. Abazajian, J. F. Beacom and N. F. Bell, Physical Review D **66**, 013008 (2002).

[11] Y. Y. Y. Wong, Physical Review D **66**, 025015 (2002).

[12] V. Barger, J. P. Kneller, P. Langacker, D. Marfatia and G. Steigman, Physics Letters B **569**, 123 (2003).

[13] J. P. Kneller, R. J. Scherrer, G. Steigman and T. P. Walker, Physical Review D **64**, 123506 (2001).

[14] A. D. Dolgov, Yadernaya Fizika **33**, 1309 (1981).

[15] B. H. J. McKellar and M. J. Thomson, Physical Review D **49**, 2710 (1994).

[16] R. Foot and R. R. Volkas, Physical Review D **55**, 5147 (1997).

[17] P. Di Bari, P. Lipari and M. Lusignoli, International Journal of Modern Physics **A15**, 2289 (2000).

[18] R. R. Volkas and Y. Y. Y. Wong, Physical Review D **62**, 093024 (2000).

[19] K. S. M. Lee, R. R. Volkas and Y. Y. Y. Wong, Physical Review D **62**, 093025 (2000).

[20] G. Gelmini, S. Palomares-Ruiz and S. Pascoli, Physical Review Letters **93**, 081302 (2004).

[21] R. Foot and R. R. Volkas, Physical Review Letters **75**, 4350 (1995).

[22] S. P. Mikheyev and A. Y. Smirnov, Yadernaya Fizika **42**, 1441 (1985).

[23] L. Wolfenstein, Physical Review D **17**, 2369 (1978).

[24] X. Shi and G. M. Fuller, Physical Review Letters **82**, 2832 (1999).

[25] L. D. Landau, Physikalische Zeitschrift der Sowjetunion **2**, 46 (1932).

[26] C. Zener, Proceedings of the Royal Society of London Series A **137**, 696 (1932).

[27] D. P. Kirilova, Astroparticle Physics **19**, 409 (2003).

[28] K. Abazajian, X. Shi and G. M. Fuller, astro-ph/9909320.

[29] M. S. Smith, L. H. Kawano and R. A. Malaney, Astrophysical Journal Supplement Series **85**, 219 (1993).

[30] R. V. Wagoner, W. A. Fowler and F. Hoyle, Astrophysical Journal **148**, 3 (1967).

[31] D. N. Spergel, R. Bean, O. Doré, M. R. Nolta, C. L. Bennett, J. Dunkley, G. Hinshaw, N. Jarosik, E. Komatsu, L. Page, H. V. Peiris, L. Verde, M. Halpern, R. S. Hill, A. Kogut, M. Limon, S. S. Meyer, N. Odegard, G. S. Tucker, J. L. Weiland, E. Wollack and E. L. Wright, Astrophysical Journal Supplement Series **170**, 377 (2007).

[32] K. A. Olive and E. D. Skillman, Astrophysical Journal **617**, 29 (2004).

[33] K. A. Olive, E. Skillman and G. Steigman, Astrophysical Journal **483**, 788 (1997).

[34] Y. I. Izotov and T. X. Thuan, Astrophysical Journal **602**, 200 (2004).

Chapter 3

Lepton Number-Driven Sterile Neutrino Production in the Early Universe

3.1 Abstract

We examine medium-enhanced, neutrino scattering-induced decoherent production of dark matter candidate sterile neutrinos in the early universe. In cases with a significant net lepton number we find two resonances, where the effective in-medium mixing angles are large. We calculate the lepton number depletion-driven evolution of these resonances. We describe the dependence of this evolution on lepton numbers, sterile neutrino rest mass, and the active-sterile vacuum mixing angle. We find that this resonance evolution can result in relic sterile neutrino energy spectra with a generic form which is sharply peaked in energy. We compare our complete quantum kinetic equation treatment with the widely-used quantum Zeno ansatz.

3.2 Introduction

In this paper we examine the physics which determines the relic densities and fossil energy spectra of neutrinos in the very early universe. The existence of new kinds of electroweak singlet "sterile" neutrinos, ν_s, with subweak interactions remains a controversial possibility. The experimental establishment of nonzero neutrino rest masses fuels legitimate speculation on this issue.

Moreover, this issue could be important because sterile neutrinos with rest masses $m_s \sim 1\,\mathrm{keV}$ are interesting dark matter candidates. The minimalist model for this dark matter scenario is where sterile neutrinos are coupled to active species via mass terms that give vacuum mixing. In turn, the simplest model along these lines is where active neutrino scattering-induced decoherence gives rise to a relic density of sterile neutrinos [1].

These simple models, however, are challenged. Vacuum active-sterile neutrino mixing, which is necessary to produce the sterile neutrinos from an initially purely active neutrino population, also enables a non-GIM suppressed radiative decay channel ($\nu_s \rightarrow \nu_{e,\mu,\tau} + \gamma$) for sterile neutrinos. As a consequence, the best constraints and probes of this sector of particle physics come from the modern x-ray observatories [2–11]. These constraints arguably eliminate the simplest models for decoherence-produced sterile neutrino dark matter.

However, there remain processes for sterile neutrino production which can produce the correct relic density for dark matter yet evade all current bounds. These viable models include, for example, sterile neutrino production associated with inflation [12], Higgs decay [13–15], and lepton number-driven medium enhancement [3, 16].

The concept of lepton number is a slippery one if sterile neutrinos exist and mix in vacuum with active species. In essence, lepton number can be created [17, 18] or destroyed [19, 20] by active-sterile neutrino interconversion. The current observational bounds [19, 21–27] on the electron, muon, and tau lepton numbers of the universe are relatively poor, at least on the scale of these quantities required to affect active-sterile neutrino conversion. Therefore, it may be important to examine in detail how lepton number influences scattering-induced decoherent production of sterile neutrinos in the early universe. This is the objective of this paper.

In what follows we investigate how the coupled interplay of sterile neutrino production, lepton number depletion, and the expansion of the universe determine the relic sterile neutrino densities and energy spectra. In Sec. 3.3 we describe in-medium active-sterile resonances and how these influence decoherent sterile neutrino production. In this section we also discuss the relationship between the quantum kinetic equations and the quantum Zeno approximation. In Sec. 3.4 we discuss the approach we employ to solve for lepton number and ν_{s} spectral evolution. In Sec. 3.5 we discuss results. Conclusions are given in Sec. 3.6.

3.3 Sterile Neutrino Production in the Early Universe

There is a long history to the general problem of the production of sterile neutrinos ν_s from an initial population of purely active neutrinos ν_α $(\alpha = e, \mu, \tau)$ [1, 3, 16, 17, 28–30]. In low density environments in supernovae and the early universe, the dominant ν_s production channel will be the coherent Mikheyev-Smirnov-Wolfenstein (MSW) process [31, 32]. However, neutrino propagation may not be coherent in the higher density regions of core collapse supernovae and the pre-neutrino-decoupling epoch in the early universe. In these environments, scattering-induced decoherence is the principal way in which sterile neutrinos are produced. Here we concentrate on the decoherent production channel since this will dominate the production of dark matter candidate sterile neutrinos.

3.3.1 The Quantum Kinetic Equations

The evolution of a system of active and sterile neutrinos can be formulated in terms of the density operator for a neutrino with given scaled momentum $\epsilon \equiv p_\nu/T$, with p_ν the neutrino momentum and T the temperature in the early universe. (Here we use natural units in which $\hbar = c = k_{\rm B} = 1$.) The density operator for scaled momentum ϵ is

$$\rho(\epsilon, t) = \sum_{i,j} \rho_{ij}(\epsilon, t) |\nu_i\rangle\langle\nu_j|, \tag{3.1}$$

where the summation is performed over neutrino flavor states, *e.g.*, $|\nu_i\rangle$ with $i = e, \mu, \tau, s$ and $\rho_{ij}(\epsilon, t)$ are the corresponding density operator matrix elements which are momentum and time dependent. Here we take the temperature $T(t)$ to be a function of the Friedman-Lemaître-Robertson-Walker time coordinate t, defined by the solution of the zero-curvature Friedman equation

$$\left(\frac{\dot{a}}{a}\right)^2 = \frac{8\pi\rho(t)}{3m_{\rm PL}^2}, \tag{3.2}$$

where $a(t)$ is the scale factor, $\rho(t)$ is the total energy density of the universe, and $m_{\rm PL}$ is the Planck mass.

For illustrative purposes, we consider 2×2 vacuum mixing between an active and sterile neutrino with a one parameter (vacuum mixing angle θ) unitary transformation between the weak eigenstates $|\nu_\alpha\rangle$ ($\alpha = e, \mu, \tau$), $|\nu_s\rangle$ and the energy-mass eigenstates $|\nu_1\rangle$, $|\nu_2\rangle$:

$$\begin{aligned} |\nu_\alpha\rangle &= \cos\theta|\nu_1\rangle + \sin\theta|\nu_2\rangle; \\ |\nu_s\rangle &= -\sin\theta|\nu_1\rangle + \cos\theta|\nu_2\rangle. \end{aligned} \tag{3.3}$$

In this 2×2 formalism, it is convenient to decompose the density operator as

$$\rho(\epsilon, t) = \frac{1}{2} P_0(\epsilon, t) \left[1 + \mathbf{P}(\epsilon, t) \cdot \boldsymbol{\sigma}\right], \tag{3.4}$$

where $\boldsymbol{\sigma}$ is the Pauli spin operator, $P_0(\epsilon, t)$ is a normalization factor proportional to the total number of neutrinos (active and sterile) with scaled momentum ϵ, and $\mathbf{P}(\epsilon, t)$ acts as a polarization vector in weak isospin space.

The diagonal matrix elements of the density operator,

$$f_\alpha(\epsilon, t) \equiv \rho_{\alpha\alpha}(\epsilon, t) = \frac{1}{2} P_0(\epsilon, t) \left[1 + P_z(\epsilon, t)\right] \tag{3.5}$$

$$f_s(\epsilon, t) \equiv \rho_{ss}(\epsilon, t) = \frac{1}{2} P_0(\epsilon, t) \left[1 - P_z(\epsilon, t)\right], \tag{3.6}$$

are proportional to the number density distributions of the neutrino species. The density operators are normalized so that the neutrino number densities are given as products of the above matrix elements and the zero chemical potential Fermi-Dirac distribution:

$$\begin{aligned} n_\alpha(\epsilon,t) &= f_\alpha(\epsilon,t)\frac{T^3(t)}{2\pi^2}\frac{\epsilon^2}{e^\epsilon+1}; & (3.7)\\ n_s(\epsilon,t) &= f_s(\epsilon,t)\frac{T^3(t)}{2\pi^2}\frac{\epsilon^2}{e^\epsilon+1}. & (3.8)\end{aligned}$$

The quantum kinetic equations can be derived [33, 34] from the time evolution of the density operator. In a homogeneous and isotropic universe, these equations can be given in terms of the time evolution of the functions $P_0(\epsilon,t)$ and $\mathbf{P}(\epsilon,t)$ as defined in Eq. (3.4),

$$\begin{aligned} \frac{\partial}{\partial t}\mathbf{P}(\epsilon,t) &= \mathbf{V}(\epsilon,t)\times\mathbf{P}(\epsilon,t)\\ &\quad +[1-P_z(\epsilon,t)]\left[\frac{\partial}{\partial t}\ln P_0(\epsilon,t)\right]\hat{z}\\ &\quad -\left[D(\epsilon,t)+\frac{\partial}{\partial t}\ln P_0(\epsilon,t)\right]\mathbf{P}_\perp(\epsilon,t) & (3.9)\\ \frac{\partial}{\partial t}P_0(\epsilon,t) &= R(\epsilon,t), & (3.10)\end{aligned}$$

where $\mathbf{P}_\perp = P_x\hat{x}+P_y\hat{y}$, and the functions $\mathbf{V}, D$, and R are defined below.

The vector $\mathbf{V}(\epsilon,t)$ corresponds to the coherent quantum mechanical evolution of the neutrino states in the early universe, and is given by

$$\mathbf{V}(\epsilon,t)=\frac{\delta m^2}{2\epsilon T(t)}\left(\sin 2\theta\,\hat{x}-\cos 2\theta\,\hat{z}\right)+V_\alpha(\epsilon,t)\hat{z}, \tag{3.11}$$

where $\delta m^2 = m_2^2 - m_1^2$ is the difference of the squares of the vacuum neutrino mass eigenvalues. The first term represents vacuum neutrino oscillations, while the second term introduces matter effects through the forward scattering potential [35, 36]

$$V_\alpha(\epsilon,t)=\frac{2\sqrt{2}\zeta(3)}{\pi^2}G_F\mathcal{L}_\alpha(t)T^3(t)-r_\alpha G_F^2\epsilon T^5(t), \tag{3.12}$$

where $\zeta(3)\approx 1.20206$, G_F is the Fermi constant, and r_α is a dimensionless coefficient which depends on the number of charged lepton degrees of freedom and can be found in Refs. [3, 19]. The potential lepton number is

$$\mathcal{L}_\alpha(t) \equiv 2L_\alpha(t) + \sum_{\beta\neq\alpha} L_\beta(t). \tag{3.13}$$

The individual lepton numbers are

$$L_\alpha(t) = \frac{n_{\nu_\alpha}(t) - n_{\bar{\nu}_\alpha}(t)}{n_\gamma(t)}, \tag{3.14}$$

where n_{ν_α}, $n_{\bar{\nu}_\alpha}$, and n_γ are the neutrino, antineutrino and photon number densities, respectively. Here we neglect contributions to the forward scattering potential from neutrino-baryon and neutrino-charged-lepton interactions since we will consider lepton numbers much larger than the baryon to photon ratio [3, 19].

The decoherence function $D(\epsilon, t)$ and the repopulation function $R(\epsilon, t)$ can be simplified by assuming thermal equilibrium of the background plasma [37]. The decoherence function corresponds to the loss of coherence resulting from collisions with particles in the early universe, and is proportional to the total scattering rate $\Gamma_\alpha(\epsilon, t)$ of neutrinos ν_α,

$$D(\epsilon, t) = \frac{1}{2}\Gamma_\alpha(\epsilon, t). \tag{3.15}$$

Using the assumption of thermal equilibrium, the total scattering rate can be written as

$$\Gamma_\alpha(\epsilon, t) \approx y_\alpha(t) G_F^2 \epsilon T^5(t), \tag{3.16}$$

where we have neglected corrections of order the lepton number L_α. The numerical coefficient $y_\alpha(t)$ primarily depends on the number of relativistic particles with weak charge that are populated in the thermal seas of the early universe at epoch t. For example, at temperatures $1\,\mathrm{MeV} \lesssim T \lesssim 20\,\mathrm{MeV}$ the total scattering rate mostly stems from interactions with other neutrinos and $e^\pm$ pairs, so that $y_e \approx 1.27$ and $y_{\mu,\tau} \approx 0.92$ [3]. However, at higher temperatures there can be appreciable populations of other charged leptons and quarks which will increase the total scattering rate.

The repopulation function $R(\epsilon, t)$ dictates the evolution of $P_0(\epsilon, t)$. Since P_0 is proportional to the total number of neutrinos with scaled momentum ϵ, the repopulation function corresponds to scattering into and out of neutrino states (ν_α and ν_s)

with scaled momentum ϵ. Assuming that each populated species, with the exception of ν_α and ν_s, has a thermal spectrum, the repopulation function can be written as

$$R(\epsilon, t) = \Gamma_\alpha(\epsilon, t) \left[\frac{e^\epsilon + 1}{e^{\epsilon - \eta_\alpha(t)} + 1} - f_\alpha(\epsilon, t) \right], \tag{3.17}$$

where η_α is the degeneracy parameter (ratio of the chemical potential to the temperature) associated with the Fermi-Dirac spectra of ν_α and $\bar{\nu}_\alpha$ with lepton number L_α,

$$L_\alpha = \frac{\pi^2}{12\zeta(3)} \left(\eta_\alpha + \frac{1}{\pi^2} \eta_\alpha^3 \right). \tag{3.18}$$

This form of the repopulation function is valid for temperatures above the neutrino decoupling temperature, where the active neutrinos are able to efficiently exchange energy and momentum with the plasma of the early universe.

The effect of the repopulation function is to drive the distribution of the active neutrino toward a Fermi-Dirac spectrum consistent with a lepton number L_α,

$$n_\alpha(\epsilon, t) \propto f_\alpha(\epsilon, t) \frac{\epsilon^2}{e^\epsilon + 1} \rightarrow \frac{\epsilon^2}{e^{\epsilon - \eta_\alpha(t)} + 1}. \tag{3.19}$$

3.3.2 The Quantum Zeno Ansatz

The quantum kinetic equations, even in their simplified form with the assumptions of homogeneity and isotropy of the early universe and thermal equilibrium in the background plasma, comprise a system of coupled nonlinear integro-partial differential equations that are difficult to solve. Past works have employed the quantum Zeno approximation to circumvent these difficulties [3, 29]. We write the quantum Zeno ansatz as a Boltzmann-like kinetic equation,

$$\begin{aligned} \frac{\partial}{\partial t} f_s(\epsilon, t) + \left(\frac{d\epsilon}{dt} \right) \frac{\partial}{\partial \epsilon} f_s(\epsilon, t) \quad &\approx \quad \frac{1}{4} \Gamma_\alpha(\epsilon, t) \sin^2 2\theta_M(\epsilon, t) \left[1 + \left(\frac{\Gamma_\alpha(\epsilon, t) \ell_m(\epsilon, t)}{2} \right)^2 \right]^{-1} \\ &\quad \times \left[f_\alpha(\epsilon, t) - f_s(\epsilon, t) \right], \end{aligned} \tag{3.20}$$

where the effective matter mixing angle θ_M is defined by

$$\sin^2 2\theta_M(\epsilon, t) = \frac{V_x^2(\epsilon, t)}{|\mathbf{V}(\epsilon, t)|^2} = \sin^2 2\theta \left[\sin^2 2\theta + \left(\cos 2\theta - \frac{2\epsilon T(t)}{\delta m^2} V_\alpha(\epsilon, t) \right)^2 \right]^{-1}, \tag{3.21}$$

and the neutrino oscillation length is

$$\ell_m(\epsilon,t) = |\mathbf{V}(\epsilon,t)|^{-1} = \left[\left(\frac{\delta m^2}{2\epsilon T(t)}\sin 2\theta\right)^2 + \left(\frac{\delta m^2}{2\epsilon T(t)}\cos 2\theta - V_\alpha(\epsilon,t)\right)^2\right]^{-1/2}. \tag{3.22}$$

The $d\epsilon/dt$ term takes into account the change in the scaled momentum of a neutrino propagating along its world line through the expanding early universe. Using the conservation of comoving entropy and assuming radiation domination, this is

$$\frac{d\epsilon}{dt} = \frac{\epsilon}{3g}\frac{dg}{dt}, \tag{3.23}$$

where g is the effective statistical weight in relativistic particles and is calculated with a weighted sum of the bosonic (g_b) and fermionic (g_f) degrees of freedom,

$$g = \sum_{\text{bosons}} g_b + \frac{7}{8}\sum_{\text{fermions}} g_f. \tag{3.24}$$

For example, at temperatures $1\,\text{MeV} \lesssim T \lesssim 20\,\text{MeV}$ the plasma of the early universe consists of photons ($g_b = 2$), $e^\pm$ pairs ($g_f = 4$), and neutrinos and antineutrinos of all three active flavors ($g_f = 6$), so $g \approx 10.75$, where we neglect corrections of order the lepton numbers.

Using the quantum Zeno ansatz instead of the full quantum kinetic equations eases computational demands by allowing calculations to be performed with distribution functions (amplitude squared) instead of with quantum amplitudes. The former approach avoids the computational pitfalls of rapidly varying complex phases that plague the latter. In Sec. 3.5, we will compare the sterile neutrino production rates calculated by the quantum kinetic equations to those implied by the quantum Zeno ansatz.

Inspection of the quantum Zeno ansatz, Eq. (3.20), suggests that maximal sterile neutrino production should occur when $\sin^2 2\theta_M = 1$. This corresponds to the resonance condition in the coherent MSW process,

$$\delta m^2 \cos 2\theta = \frac{4\sqrt{2}\zeta(3)}{\pi^2} G_F \mathcal{L} \epsilon_{\text{res}} T^4 - 2 r_\alpha G_F^2 \epsilon_{\text{res}}^2 T^6. \tag{3.25}$$

The solutions to Eq. (3.25) are the resonant scaled momenta

$$\epsilon_{\text{res}}(t) = \frac{\sqrt{2}\zeta(3)}{\pi^2 r_\alpha G_F} \frac{\mathcal{L}(t)}{T^2(t)} \left(1 \pm \sqrt{1 - \frac{\pi^4 r_\alpha \delta m^2 \cos 2\theta}{4\zeta^2(3)\mathcal{L}^2(t)T^2(t)}} \right). \tag{3.26}$$

Therefore, resonances occur when the following condition is met:

$$|\mathcal{L}(t)|\, T(t) \geq \frac{\pi^2}{2\zeta(3)} \sqrt{r_\alpha \delta m^2 \cos 2\theta}. \tag{3.27}$$

In Sec. 3.5 we will discuss the results of our numerical calculations and the effects of these MSW-like resonances and this resonance condition. The production of sterile neutrinos from an initial active neutrino distribution reduces the potential lepton number $\mathcal{L}$. Furthermore, the expansion of the universe results in a decrease of the temperature T. These two trends together ensure that the resonance condition, Eq. (3.27), will be violated at some point. However, the enhancement in sterile neutrino production associated with this MSW resonance is suppressed by the quantum Zeno effect.

The quantum Zeno effect is the result of scattering-induced decoherence interrupting the accumulation of quantum phase, suppressing quantum transitions between two discrete states [38]. In the quantum Zeno ansatz, this effect is represented by the multiplicative factor,

$$\left[1 + \left(\frac{\Gamma_\alpha \ell_m}{2} \right)^2 \right]^{-1}.$$

The ratio of the neutrino oscillation length, ℓ_m, to the mean scattering length, Γ_α^{-1}, determines the level of suppression stemming from the quantum Zeno effect.

If the neutrino oscillation length is much larger than the scattering length, $\ell_m \gg \Gamma_\alpha^{-1}$, quantum coherence is lost before significant quantum phase can be accumulated, suppressing the transition. This is the case at the MSW resonances because at resonance the neutrino oscillation length is maximal. The suppression of sterile neutrino production at the MSW resonances means that maximal sterile neutrino production occurs at a time that does not correspond to an MSW resonance. However, since we will be considering small values of $\sin^2 2\theta$, the MSW resonances have small widths and as a result we nevertheless have maximal sterile neutrino production near to these MSW resonances.

Far from resonance, there is little suppression from the quantum Zeno effect. This results from a coincidence in the functional form of the forward scattering potential and total scattering rate. At temperatures much larger than the resonance temperature, the product $\Gamma_\alpha \ell_m$ approaches a constant much less than 1, while at temperatures much lower than the resonance temperature, $\Gamma_\alpha \ell_m$ rapidly falls as the temperature of the expanding universe decreases.

There is another possibility for maximizing the sterile neutrino production rate. This occurs when the potential lepton number has decreased and/or the temperature has fallen to a point where the resonance condition, Eq. (3.27), is no longer satisfied and there are no MSW resonances. In this scenario, $\sin^2 2\theta_M$ reaches a local maximum but is less than 1, which means that the neutrino oscillation length tends to be much smaller than in the resonant case. Additionally, this occurs at later times, and thus lower temperatures, during the expansion of the universe, which means the product $\Gamma_\alpha \ell_m$ is significantly smaller than in the resonant case. As a result, the overall sterile neutrino production rate can be higher than in the resonant case and would have a broader peak than in the resonant case. With the right conditions, this nonresonant production of sterile neutrinos can become significant.

Throughout this section we have discussed the transformation properties of $\nu_\alpha \leftrightarrow \nu_s$ using the quantum kinetic equations and the quantum Zeno ansatz. However, to consider the general problem of neutrino transformation in the early universe, we must also include its CP-counterpart, $\bar{\nu}_\alpha \leftrightarrow \bar{\nu}_s$. The quantum kinetic equations and quantum Zeno ansatz are similar for the $\bar{\nu}_\alpha$, $\bar{\nu}_s$ system with a few alterations. The forward scattering potential V_α [Eq. (3.12)] is adjusted by replacing $\mathcal{L}_\alpha$ with $-\mathcal{L}_\alpha$, and the total scattering rate Γ_α [Eq. (3.16)] is replaced by one appropriate for antineutrinos, $\bar{\Gamma}_\alpha$. However in the early universe, to lowest order, these two scattering rates are equal, $\Gamma_\alpha \approx \bar{\Gamma}_\alpha$.

In this paper we will consider large lepton numbers which helps to avoid the necessity of considering both neutrinos and antineutrinos. For a large positive lepton number, all of the action occurs in the neutrino sector. The effective matter mixing angle for antineutrinos is significantly less than their vacuum mixing angles, while neutrinos may experience the MSW-like resonances discussed above. For large negative lepton numbers, the same is true, but for the CP-counterpart.

3.4 Calculations

Calculating the evolution of the active and sterile neutrino distribution functions remains a daunting task. In addition to the quantum Zeno ansatz, Eq. (3.20), we must elucidate the lepton number evolution. We assume that the active neutrinos are in thermal equilibrium in the early universe and that active-sterile neutrino conversion is the only flavor changing interaction. The former assumption of thermal equilibrium is a good one before weak decoupling where the high temperature of the universe ($T \gtrsim 3\,\mathrm{MeV}$) ensures that the weak interaction time scale is much shorter than a Hubble time, the time scale for the expansion of the universe. The latter assumption amounts to assuming that there is no exotic physics other than active-sterile neutrino oscillations. For the epoch before weak decoupling, the time evolution of the lepton number L_α is

$$\frac{d}{dt}L_\alpha(t) = -\frac{1}{4\zeta(3)}\int_0^\infty d\epsilon \frac{\epsilon^2}{e^\epsilon + 1}\frac{\partial}{\partial t}f_s(\epsilon, t). \tag{3.28}$$

Together, the quantum Zeno ansatz [Eq. (3.20)] and lepton number evolution [Eq. (3.28)] form a formidable system of integro-partial differential equations. To simplify the situation, we assume that the effective statistical weight, g, is constant. Strictly speaking, this is not the case in the early universe because species fall out of thermal equilibrium as time progresses and the temperature decreases. However, a well accepted detailed history $g(t)$ does not currently exist. As a result, for illustrative purposes, we will assume that g is constant.

By making this assumption we benefit in a number of ways. The temperature evolution of the universe, $T(t)$, is greatly simplified. As different species fall out of thermal equilibrium, particle-antiparticle pair annihilation reheats the universe, resulting in a complicated temperature evolution. The temperature evolution, as given by the Friedman equation, the conservation of comoving entropy, and assuming radiation domination, is

$$\frac{1}{T}\frac{dT}{dt} = -\left(\frac{4\pi^3}{45}\right)^{1/2} g^{1/2}\frac{T^2}{m_{\mathrm{PL}}}. \tag{3.29}$$

Since $T(t)$ is a monotonically decreasing function of time, we can invert it to find $t(T)$. We are then able to perform our calculations as a function of temperature.

In addition, a constant g means that, by Eq. (3.23), $d\epsilon/dt = 0$. As a result, the quantum Zeno ansatz becomes an ordinary differential equation for a family of sterile neutrino distribution functions, parameterized by ϵ. The only coupling between the different values of ϵ that remains is found in the lepton number evolution, Eq. (3.28).

We choose a value of g that is representative of the early universe before the QCD transition, $170\,\mathrm{MeV} \lesssim T \lesssim 1\,\mathrm{GeV}$. In this epoch, the plasma of the early universe consists of photons ($g_b = 2$), gluons ($g_b = 16$), $e^{\pm}$ and $\mu^{\pm}$ pairs ($g_f = 8$), neutrinos and antineutrinos of all three active flavors ($g_f = 6$), and up, down, and strange quarks and antiquarks ($g_f = 36$), so $g \approx 61.75$, where we neglect corrections of order the lepton numbers and baryon to photon ratio. At higher temperatures the other quarks come into the picture, but at this point the time scale for expansion in the early universe is so fast that there is little net effect from the difference in g values.

We use the forward scattering potential given in Eq. (3.12), which is accurate at times after the QCD transition and for lepton numbers much larger than the baryon to photon ratio. However, we are interested in times before the QCD transition where gluons and free quarks thermally populate the early universe. The proper form of the forward scattering potential remains an open area of research [39, 40]. The results presented in this paper will remain relevant unless the total forward scattering potential arising from the quarks is many orders of magnitude larger than the forward scattering on color singlet baryons and mesons with the same net baryon number.

On the other hand, the total scattering rate is greatly influenced by the additional species thermalized before the QCD transition. However, since neutrino-quark interactions are not well studied, the total scattering rate in the QCD epoch remains a question mark. We use the values given in Sec. 3.3.1, although our calculations deal with a different epoch in the early universe. In addition, we calculate the effects of an increased scattering rate, by assuming that this rate is proportional to the number of relativistic particles with weak charge populated in the early universe.

We solve the system of integro-differential equations posed by the quantum Zeno ansatz for different values of ϵ, and the lepton evolution. Using Eq. (3.29), we change variables to follow the sterile neutrino distribution functions and lepton number as a function of the declining temperature of the expanding universe. The initial conditions are chosen so that there are initially no sterile neutrinos, $f_s = 0$, and the initial lepton number is a free parameter, but we assume that there is an equivalent lepton number in each of the active neutrino species. The initial (final) temperature for the calculations is chosen to be high (low) enough that the choice of this has no effect on the final outcome (sterile neutrino spectrum and final lepton number).

For illustrative purposes, we choose to work with electron neutrinos as the sole active species which mixes with sterile neutrinos ($\alpha = e$). We do not include mixing with ν_μ or ν_τ; this includes active-active mixing with ν_e and among themselves, and active-sterile mixing with ν_s. This is unrealistic, since the neutrino mixing matrix could be quite complicated. However, our simplistic model will at least serve to illustrate trends in sterile neutrino production and lepton number depletion [3, 19].

In addition to the numerical procedure outlined above, we also solve the quantum kinetic equations, Eqs. (3.9−3.10), for a given value of ϵ. Using the lepton evolution calculated with the quantum Zeno ansatz, we compare the evolution of the sterile neutrino distribution function between the two methods. The principal difficulty in solving the quantum kinetic equations is the need to resolve rapidly varying complex phases. To ease these computational demands, we employ an eighth-order Runge-Kutta method [41] which allows the use of a larger time step to solve the problem.

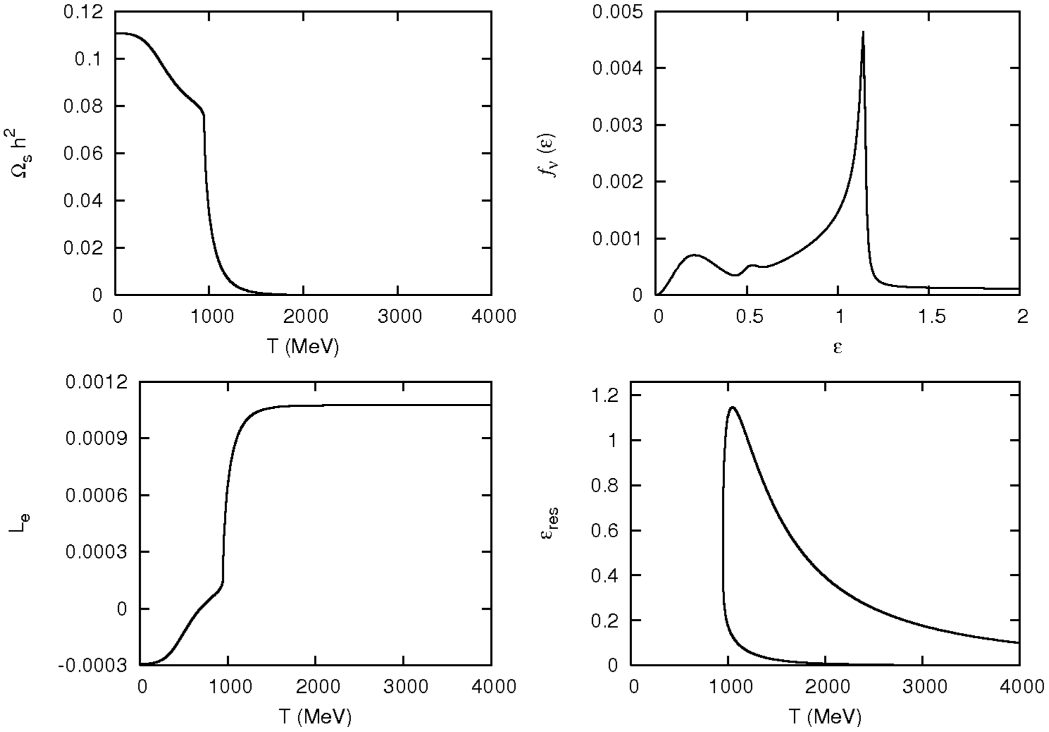

Figure 3.1: Results for our calculation using the quantum Zeno ansatz. In this calculation, we take the sterile neutrino rest mass $m_s = 64\,\mathrm{keV}$, vacuum mixing angle $\sin^2 2\theta = 10^{-10}$, and initial lepton number $L_{e0} = 1.1 \times 10^{-3}$. The upper left panel shows the cumulative sterile neutrino production history in terms of its closure fraction in the current epoch, $\Omega_s h^2$. Below that, in the lower left corner, is the lepton number history. The upper right panel displays the final ν_s spectrum as a function of scaled momentum ϵ. In the lower right panel is a plot that tracks the resonant values of ϵ as our calculation evolves in temperature.

3.5 Results

The particulars of phenomena revealed by the calculations described in the last section depend on the assumed values of sterile neutrino mass m_s, vacuum mixing angle θ, and initial lepton number, L_{e0}, in each active neutrino species. (As discussed above, we take $L_{e0} = L_{\mu 0} = L_{\tau 0}$.) Some ranges of the sterile neutrino parameters can be ruled out by the x-ray observations [2–11] or by observations of smaller-scale large scale structure (*e.g.*, the Lyman-α forest) coupled with structure formation calculations [9, 42–44]. Bounds on the lepton numbers from big bang nucleosynthesis considerations [21–24] are much larger than those employed in our calculations. It is important to note that these lepton number limits constrain the final lepton numbers, not the initial lepton numbers. However, other parameter values remain unconstrained by these considerations and, therefore, are still "in play" for providing a relic sterile neutrino density which could comprise some or all of the dark matter. The observed dark matter closure fraction, Ω_c, is measured to be $\Omega_c h^2 = 0.1105 \pm 0.0039$ where $h \equiv H_0/100\,\mathrm{km\,s^{-1}\,Mpc^{-1}}$, with H_0 the Hubble parameter [45].

A set of parameters that produces the correct relic mass density to be the dark matter, but is nevertheless ruled out by x-ray observations provides particularly instructive cases. These parameters give lepton number depletion and sterile neutrino production histories which show a variety of possible behaviors associated with resonant and nonresonant evolution. Scenarios associated with these parameters give distinctive features in the final relic sterile neutrino energy spectrum which are directly attributable to the way the MSW resonance sweep couples with lepton number depletion.

Results for an example set of these parameters are shown in Fig. 3.1. For this case we have taken $m_s = 64\,\mathrm{keV}$, $\sin^2 2\theta = 10^{-10}$, and $L_{e0} = 1.1 \times 10^{-3}$. Using the quantum Zeno ansatz, our calculations yield a sterile neutrino relic density which is consistent with the observed dark matter closure fraction.

The panel in the lower right of Fig. 3.1 shows the sweep history of the two MSW resonances (*i.e.*, as in Eq. 3.26). The resonant scaled momentum ($\epsilon_{\rm res}$) of each resonance has a characteristic behavior. As the universe expands, the temperature T drops, and lepton number is depleted, these resonances first diverge and then converge in scaled momentum. At a temperature $\sim 950\,\mathrm{MeV}$, the temperature has fallen and the lepton number has been depleted to a point where the resonance condition, Eq. (3.27), cannot be satisfied and so subsequently there can be no MSW resonances.

The lepton number history and the cumulative sterile neutrino production history (as measured by its closure fraction in the current epoch $\Omega_s h^2$) are shown in the lower and upper left-hand panels of Fig. 3.1, respectively. The temperature where MSW resonances cease to exist corresponds to an abrupt shift in the sterile neutrino production mechanism, from resonant to nonresonant production. Roughly 70 percent of the total relic sterile neutrino density is produced resonantly. At temperatures slightly above those characteristic of the resonance cessation event, there is an epoch of precipitous depletion of lepton number and concomitant production of sterile neutrinos.

The sharp decline in lepton number and the subsequent loss of resonance are a consequence of the coupling between the sweep of the MSW resonances and lepton number evolution. As the MSW resonances sweep through the ν_e distribution, and ν_e's are converted to ν_s's, lepton number is lost. In turn, the decreasing lepton number accelerates the resonance sweep rate. This positive feedback loop results in the precipitous depletion of lepton number. This process ends once MSW resonances cease to exist, as seen in our calculations.

This behavior, coupled with the dominance of resonant ν_s production, results in a characteristic set of peaks in the relic sterile neutrino energy spectrum

$$f_\nu(\epsilon) \equiv f_s(\epsilon, T_f)\frac{\epsilon^2}{e^\epsilon + 1}, \tag{3.30}$$

where T_f is the final temperature in the calculations. These features are seen in the upper right panel of Fig. 3.1. In this figure, there are two distinct peaks seen at $\epsilon \approx 0.2$ and $\epsilon \approx 1.15$, and a smaller peak at $\epsilon \approx 0.5$. The three peaks are the result of different physical processes. Understanding these processes provides physical insight into the mechanism of sterile neutrino production.

Since the magnitude of the lepton number is small throughout the calculation, $|L_e| \ll 1$, we can make the approximation that $f_e(\epsilon, T) \approx 1$, neglecting corrections of order the lepton number. As a result, Eq. (3.20) can be solved analytically if we use the lepton number evolution $L_e(T)$ from our calculations. This will provide an analytical backbone upon which to base our analysis.

Using this approximation, the solution to the quantum Zeno ansatz yields a relic sterile neutrino energy spectrum

$$f_\nu(\epsilon) \approx \frac{\epsilon^2}{e^\epsilon + 1}\left(1 - \exp\left\{-\int_{T_0}^{T_f} \gamma(\epsilon, \tau)\, d\tau\right\}\right), \tag{3.31}$$

where

$$\gamma(\epsilon, T) \equiv \frac{1}{4\dot{T}(T)} \frac{\Gamma_e(\epsilon, T)\sin^2 2\theta_M(\epsilon, T)}{1 + \frac{1}{4}\Gamma_e^2(\epsilon, T)\ell_m^2(\epsilon, T)} \tag{3.32}$$

is the $\nu_e \leftrightarrow \nu_s$ conversion rate per unit temperature interval. In theory, the initial temperature $T_0 \to \infty$, but in practice is chosen as described in Sec. 3.4.

For a fixed value of ϵ, $\gamma(\epsilon, T)$ is a sharply peaked function of temperature T whenever MSW resonances exist. This is the result of this function's proportionality to $\sin^2 2\theta_M$, which has sharp peaks when $\sin^2 2\theta_M = 1$ at the MSW resonances discussed above. The locations in temperature of these resonances are implicitly given by the solutions of Eq. (3.25) for a fixed value of ϵ.

However, the widths of the peaks in $\gamma(\epsilon, T)$ do not correspond to the widths of the associated MSW resonances. Both $\sin^2 2\theta_M(\epsilon, T)$ and $\ell_m^2(\epsilon, T)$ are sharply peaked functions. The resonance width of both functions is $\delta T \approx \mathcal{H} \tan 2\theta$ (see, *e.g.* Ref. [19]), where $\mathcal{H}$ is the density scale height at resonance and is defined as

$$\begin{aligned} \mathcal{H} &\equiv \left|\frac{1}{V_e}\frac{dV_e}{dT}\right|_{\text{res}}^{-1} \\ &= \left|\frac{5}{T} - \frac{8\sqrt{2}\zeta(3)}{\pi^2\delta m^2\cos 2\theta} G_F \epsilon \mathcal{L} T^3 \left(1 - \frac{d\log\mathcal{L}}{d\log T}\right)\right|_{\text{res}}^{-1}. \end{aligned} \tag{3.33}$$

In the neighborhood of each resonance, $\Gamma_e^2 \ell_m^2/4 \gg 1$, so near resonance

$$\gamma(\epsilon, T) \approx \frac{1}{\dot{T}(T)\Gamma_e(\epsilon, T)} \frac{\sin^2 2\theta_M(\epsilon, T)}{\ell_m^2(\epsilon, T)}. \tag{3.34}$$

The sharp peaks in both $\sin^2 2\theta_M(\epsilon, T)$ and $\ell_m^2(\epsilon, T)$, in a sense, cancel each other out. This is because the ratio of these functions,

$$\frac{\sin^2 2\theta_M(\epsilon, T)}{\ell_m^2(\epsilon, T)} = \left(\frac{\delta m^2 \sin 2\theta}{2\epsilon T}\right)^2, \tag{3.35}$$

is no longer strongly peaked.

A measure of the width of the resonances in $\gamma(\epsilon, T)$ can be obtained by setting $\Gamma_e^2 \ell_m^2/4 = 1$. Far from resonance, $\Gamma_e^2 \ell_m^2/4 \lesssim 1$, so that $\gamma(\epsilon, T) \propto \epsilon\, T^2 \sin^2 2\theta_M$, which means $\gamma(\epsilon, T)$ has the same resonant shape as $\sin^2 2\theta_M$. When $\Gamma_e^2 \ell_m^2/4 \gtrsim 1$ closer to the resonance, $\gamma(\epsilon, T) \propto \epsilon^{-3} T^{-10}$, which means the peaked behavior is truncated and the location of the maximum of the neutrino conversion rate is displaced from the location of the MSW resonance to a slightly lower temperature. The change in the forward scattering potential required to satisfy this condition is $\delta V_e \approx \Gamma_e/2$. The width in temperature space corresponding to this potential width is

$$\begin{aligned} \delta T(\epsilon, T_{\mathrm{res}}) &= \left|\frac{\delta V_e}{V_e}\right|_{\mathrm{res}} \left|\frac{1}{V_e}\frac{dV_e}{dT}\right|_{\mathrm{res}}^{-1} \\ &\approx \frac{\epsilon\, T_{\mathrm{res}}}{\delta m^2 \cos 2\theta} \Gamma_e(\epsilon, T_{\mathrm{res}}) \mathcal{H}. \end{aligned} \tag{3.36}$$

If we restrict ourselves to values of ϵ for which MSW resonances are possible ($\epsilon < 1.15$ for the calculations done with the parameters in Fig. 3.1), then the sharp peaks in $\gamma(\epsilon, T)$ allow us to make the approximation:

$$\int_{T_0}^{T_f} \gamma(\epsilon, \tau)\, d\tau \approx \sum_i g_i \gamma(\epsilon, T_{\mathrm{res},i}) \delta T(\epsilon, T_{\mathrm{res},i}), \tag{3.37}$$

where g_i is a numerical coefficient of order unity, $T_{\mathrm{res},i}$ is the temperature of the MSW resonance for scaled momentum ϵ, and the sum is performed over every resonance. This approximation breaks down when two resonances begin to overlap, a situation we will discuss below.

The product

$$\gamma(\epsilon, T_{\rm res})\delta T \approx \frac{1}{2}\frac{\delta m^2}{2\epsilon T_{\rm res}}\frac{\sin^2 2\theta}{\cos 2\theta}\left(\dot{T}^{-1}\mathcal{H}\right), \tag{3.38}$$

is equal to one-half of the the dimensionless adiabaticity parameter defined in Eq. (38) of Ref. [19], but with the flavor off-diagonal potential set to zero, $B_{e\tau} = 0$. Note also that the density scale height in this work, $\mathcal{H}$, is defined as the width in temperature of the MSW resonance, but the density scale height in Ref. [19], $\mathcal{H} = \dot{T}^{-1}\mathcal{H}$, is defined as the physical width of the MSW resonance.

If the g_i in Eq. (3.37) are equal to π, then this result is equivalent to the Landau-Zener approximation. However, these numerical coefficients depend on the shape of the resonances, in particular on the shape of the forward scattering potential V_e. On the other hand, the coherent $\nu_e \rightarrow \nu_s$ probability is only equal to the Landau-Zener approximation when the forward scattering potential is linear. It is interesting to see the relationship between the coherent $\nu_e \rightarrow \nu_s$ conversion through the coherent MSW process and scattering-induced decoherent ν_s production. Reference [16] used this result without this analysis.

The low-ϵ peak is the product of two opposing factors: a ν_e spectrum that increases and a $\nu_e \rightarrow \nu_s$ conversion probability that decreases as ϵ increases. At small values of ϵ, the number density of ν_e with scaled momentum ϵ that are available to be converted into ν_s is proportional to ϵ^2.

The lower right panel in Fig. 3.1 shows that at these ϵ values there are two resonances, one at a high temperature ($\gtrsim 2000\,\mathrm{MeV}$) and another at a lower temperature near the resonance cessation event ($\sim 1000\,\mathrm{MeV}$). At these temperatures $\delta T \propto \epsilon T^3 |d\log\mathcal{L}/d\log T - 1|^{-1}$, so that the product $\gamma(\epsilon, T_{\rm res})\delta T$ in Eq. (3.37) is proportional to $\epsilon^{-2}T_{\rm res}^{-7}|d\log\mathcal{L}/d\log T - 1|^{-1}$. Consequently, the contribution from the low-temperature resonance is dominant over the contribution from the high-temperature resonance. At small values of ϵ ($\epsilon \lesssim 0.4$), the relic sterile neutrino distribution is

$$f_\nu(\epsilon) \approx \frac{\epsilon^2}{e^\epsilon + 1}\left(1 - \exp\left\{-\kappa\epsilon^{-2}T_{\rm res}^{-7}\left|\frac{d\log\mathcal{L}}{d\log T} - 1\right|_{\rm res}^{-1}\right\}\right), \tag{3.39}$$

where κ is a constant that depends on sterile neutrino parameters and physical constants, and $T_{\rm res} = T_{\rm res}(\epsilon)$ is the low-temperature solution to Eq. (3.25). This distribution can be seen graphically in the lower right panel of Fig. 3.1.

Examination of Fig. 3.1 reveals that $T_{\rm res}(\epsilon)$ is a slowly decreasing function of ϵ (*e.g.*, a factor of 4 increase in ϵ leads to a 15 percent decrease in $T_{\rm res}$). As a result, $\epsilon^{-2}T_{\rm res}^{-7}$ remains a decreasing function of ϵ. In addition, $d\log\mathcal{L}/d\log T$ is maximal immediately preceding the resonance cessation event and decreases with increasing temperature. It follows that $|d\log\mathcal{L}/d\log T - 1|^{-1}$ is also a decreasing function of ϵ. Thus, the cumulative $\nu_e \rightarrow \nu_s$ conversion probability, $1 - e^{-\int\gamma\,d\tau}$, is a decreasing function of ϵ. The interplay between this and the increasing spectrum of ν_e produces the peak seen at low values of ϵ.

The high-ϵ peak corresponds to the maximum value of ϵ ($\epsilon_{\rm max}$) for which MSW resonances exist. At this value of ϵ, the MSW resonance equation, Eq. (3.25), has only one positive temperature solution (a double root). In the case shown in Fig. 3.1, this occurs at $\epsilon_{\rm max} \approx 1.15$.

For $\epsilon < \epsilon_{\rm max}$, the energy spectrum increases as ϵ increases, and as it approaches the maximum value, it increases at a greater rate until it hits the peak. Here, the proportionality to ϵ loses the sway it had at lower values of ϵ because the fractional changes are an order of magnitude smaller. In this regime, the high-temperature resonance moves to lower temperatures where it becomes significant in contributing to the $\nu_e \rightarrow \nu_s$ conversion probability. Additionally, as the two resonances approach each other, the peaks tend to blend with each other, enhancing the value of $\int\gamma\,d\tau$, culminating with the merger of the two peaks. The sharp increase in f_ν indicates the point at which this phenomenon becomes significant.

For values of ϵ slightly larger than $\epsilon_{\rm max}$, the energy spectrum falls off precipitously. This is because neutrinos with $\epsilon > \epsilon_{\rm max}$ have no resonances, and thus sterile neutrino production is suppressed compared to the regime with resonant production.

The mid-ϵ peak corresponds to the last resonant value of ϵ. At the temperature where MSW resonances cease to exist, there is an abrupt transition from resonant to nonresonant sterile neutrino production. During the final stages of resonant sterile

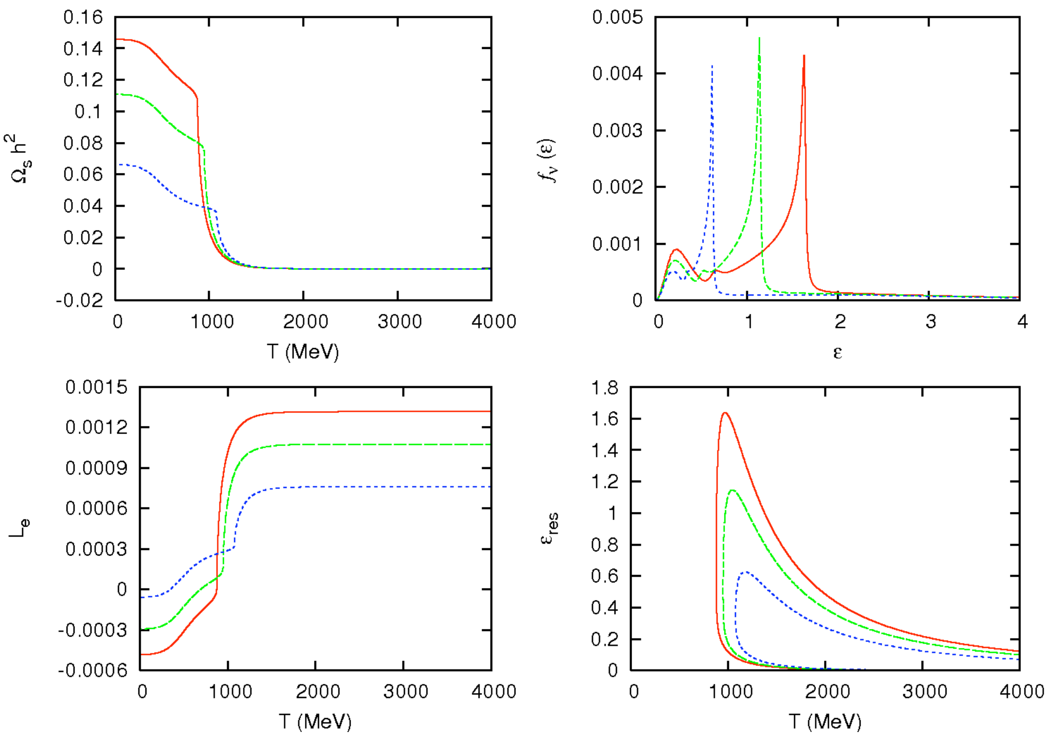

Figure 3.2: The four panels present the same quantities as in Fig. 3.1. In this figure, we have taken $m_s = 64\,\mathrm{keV}$, $\sin^2 2\theta = 10^{-10}$, and three different values for the initial lepton number: $L_{e0} = 0.76 \times 10^{-3}$ (short dashed curves), 1.1×10^{-3} (long dashed curves), and 1.3×10^{-3} (solid curves).

neutrino production, there is a large conversion rate of active neutrinos to sterile neutrinos, producing a large lepton number loss rate, leading to a smaller resonance width. Immediately after the resonance cessation event, lepton number is depleted at a far lower rate, as only nonresonant conversion remains. This leads to the low-temperature side of the resonance being much broader than the high-temperature side. As a result, there is an enhancement in the $\nu_e \rightarrow \nu_s$ conversion probability that is maximized at the last resonant ϵ. This effect is significantly smaller than the effects associated with the two peaks discussed previously.

Figures 3.2 - 3.4 show the effects of changing each of the three free parameters in our calculation. Figure 3.2 presents the effects of changing the initial lepton number in each active neutrino species, but leaving the sterile neutrino mass and vacuum mixing angle fixed. Figure 3.3 shows the effects of changing the sterile neutrino mass, and Figure 3.4 shows the effects of changing the vacuum mixing angle θ. Each figure displays the same four panels as discussed for Fig. 3.1. The results discussed above serve as a guide to understanding the trends in these figures.

In Fig. 3.2, we have taken $m_s = 64\,\mathrm{keV}$ and $\sin^2 2\theta = 10^{-10}$. We have varied the initial lepton number and show three cases, corresponding to $L_{e0} = 0.76 \times 10^{-3}$, 1.1×10^{-3}, and 1.3×10^{-3}.

The resonance cessation event occurs at a higher temperature for lower initial lepton numbers. We can understand this result using the resonance condition, Eq. (3.27). Since we assume that initially the lepton number is equal in each active neutrino species and we only allow ν_e-ν_s neutrino oscillations, the potential lepton number can be written as $\mathcal{L}(T) = 2L_{e0} + 2L_e(T)$. Most of the initial ν_e lepton number is depleted by $\nu_e \to \nu_s$ conversion, so that at the cessation event $\mathcal{L} \approx 2L_{e0}$. As a result, lower initial lepton numbers mean an earlier (higher temperature) loss of resonance.

The maximum resonant ϵ, ϵ_{max}, increases with increasing initial lepton number. As seen in Eq. (3.26), the upper resonance is proportional to $\mathcal{L}/T^2$. This implies that the resonant scaled momenta can reach higher values for higher initial lepton numbers. For $\epsilon \lesssim 2.2$ there are more ν_e available to convert into ν_s at a given value of ϵ as ϵ increases.

We must perform the same analysis done above in estimating the cumulative $\nu_e \to \nu_s$ conversion probability. Preserving the proportionality to the potential lepton number and sterile neutrino mass and mixing angle, we have

$$\gamma(\epsilon, T_{\mathrm{res}})\delta T \propto \epsilon^{-2} T_{\mathrm{res}}^{-7} \left| \frac{d\log\mathcal{L}}{d\log T} - 1 \right|_{\mathrm{res}}^{-1} \mathcal{L}^{-1} m_s^4 \sin^2 2\theta, \tag{3.40}$$

where the assumed sterile neutrino mass is $m_s \approx \sqrt{\delta m^2}$. The relevant resonance temperatures are approximately equal to the temperature of the resonance cessation event, which increases with decreasing initial lepton number. In our calculations, T_{res}^{-7} dominates over $\mathcal{L}^{-1}$, so in concert with the trend for ϵ_{max}, increasing the initial

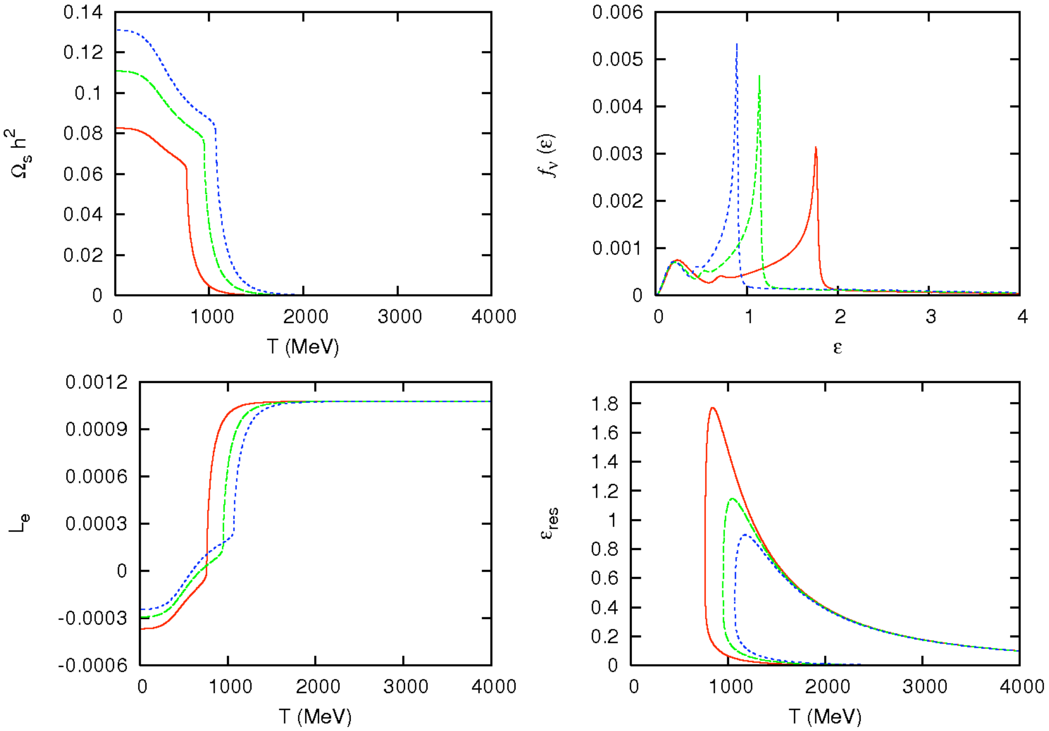

Figure 3.3: The four panels present the same quantities as in Fig. 3.1. In this figure, we have taken $L_{e0} = 1.1 \times 10^{-3}$, $\sin^2 2\theta = 10^{-10}$, and three different values for the sterile neutrino rest mass: $m_s = 45\,\text{keV}$ (solid curves), $64\,\text{keV}$ (long dashed curves), and $79\,\text{keV}$ (short dashed curves).

lepton number leads to a larger (in magnitude) loss of ν_e lepton number,

$$\Delta L_e = -\frac{1}{4\zeta(3)} \int_0^\infty f_\nu(\epsilon)\, d\epsilon. \tag{3.41}$$

Consequently, the number density of sterile neutrinos produced, $n_{\nu_s} = -n_\gamma \Delta L_e$, increases with increasing initial lepton numbers. Thus, the sterile neutrino closure fraction, $\Omega_s \propto m_s n_{\nu_s}$, also increases with increasing initial lepton number.

In Fig. 3.3, we have taken $L_{e0} = 1.1 \times 10^{-3}$, $\sin^2 2\theta = 10^{-10}$ and varied the sterile neutrino rest mass. In this figure we show the results of our calculations for sterile neutrino masses $m_s = 45\,\text{keV}$, $64\,\text{keV}$, and $79\,\text{keV}$.

It is clear from this figure that the resonance cessation event occurs at higher temperatures for higher masses. This trend can be understood by noticing that the right hand side of Eq. (3.27) is proportional to m_s. Therefore, with the same arguments as above, but now with a fixed lepton number, equality in Eq. (3.27) (which marks the end of resonances) is reached at higher temperatures for higher assumed sterile neutrino masses.

In this calculation, at high temperatures ($T \gtrsim 2000\,\mathrm{MeV}$) the resonant values of ϵ do not depend on sterile neutrino mass. Using the proportionality in Eq. (3.40), lepton number depletion, and the concomitant sterile neutrino production, will be highest for the higher mass sterile neutrinos, at least early on. As a result, the highest mass sterile neutrino will have the lowest value of ϵ_{max} and the highest temperature at which the resonance cessation event occurs.

The two competing factors in Eq. (3.40), T_{res}^{-7} and m_s^4, nearly balance each other, but the higher value of ϵ_{max} for lower sterile neutrino masses results in a larger (in magnitude) value of ΔL_e. However, it can be seen in the lower left panel of Fig. 3.3 that the values of ΔL_e for the three sterile neutrino masses shown do not differ by much. As a result, the sterile neutrino closure fraction, the relevant quantity in searching for a dark matter candidate, increases for increasing assumed sterile neutrino mass.

In Fig. 3.4, we have taken $m_s = 64\,\mathrm{keV}$ and $L_{e0} = 1.1 \times 10^{-3}$ but have employed different values of the vacuum mixing angle θ. The figure shows three cases, for $\sin^2 2\theta = 0.5 \times 10^{-10}$, 1.0×10^{-10}, and 2.0×10^{-10}.

For the vacuum mixing angles that we are concerned with here, the locations of the MSW resonances are insensitive to the value of θ (since $\cos 2\theta \approx 1 - 0.5 \sin^2 2\theta$). As a result, differences in the evolution of ϵ_{res} are linked to the differences in the lepton number evolution. At high temperatures ($T \gtrsim 1500\,\mathrm{MeV}$ for this calculation), the resonances sweep through the ν_e distribution at the same rate, but the proportionality to $\sin^2 2\theta$ in Eq. (3.40) leads to a larger sterile neutrino production for larger vacuum mixing angles. As a result, the resonance condition, Eq. (3.27), will be violated at the highest temperature for the highest mixing angle. Thus, the largest mixing angle corresponds to the highest resonance cessation temperature and the smallest value of ϵ_{max}.

The combination of the proportionality of the cumulative $\nu_e \rightarrow \nu_s$ conversion rate

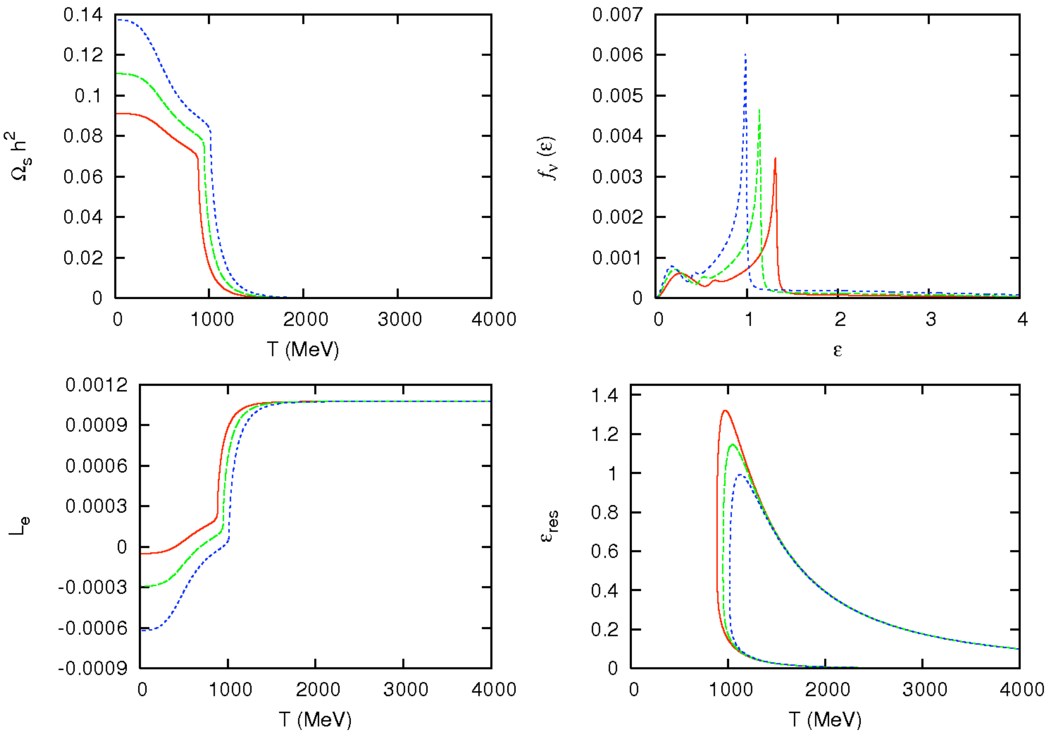

Figure 3.4: The four panels present the same quantities as in Fig. 3.1. In this figure, we have taken $m_s = 45\,\mathrm{keV}$, $L_{e0} = 1.1 \times 10^{-3}$, and three different values for the vacuum mixing angle: $\sin^2 2\theta = 0.5 \times 10^{-10}$ (solid curves), 1.0×10^{-10} (long dashed curves), and 2.0×10^{-10} (short dashed curves).

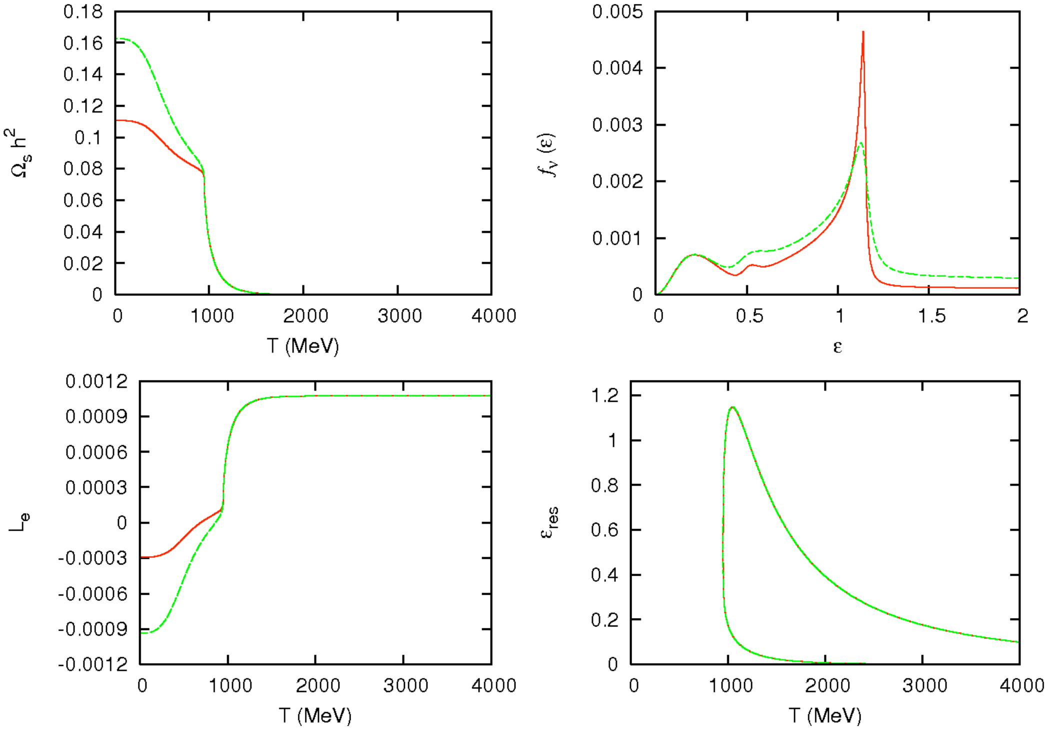

Figure 3.5: The four panels present the same quantities as in Fig. 3.1. In this figure, we have taken $m_s = 64\,\mathrm{keV}$, $L_{e0} = 1.1 \times 10^{-3}$, and $\sin^2 2\theta = 10^{-10}$. We present two calculations, one with a low total scattering rate Γ_e as discussed in section 3.3.1 (solid curves), and one with a higher total scattering rate $\Gamma_e \to 3.5\Gamma_e$ (dashed curves). For $T \gtrsim 950\,\mathrm{MeV}$, the cumulative sterile neutrino production history, lepton number history, and resonant values of ϵ are nearly identical in the two calculations.

to $\sin^2 2\theta$, along with the weak dependence of the resonant temperatures and ϵ_{max} on the vacuum mixing angle, result in resonant production of sterile neutrinos being highest for higher values of vacuum mixing angle. However, this is just the tip of the iceberg. Nonresonant scattering-induced decoherent production of sterile neutrinos is also proportional to $\sin^2 2\theta$. As a result, higher vacuum mixing angles generally result in a higher sterile neutrino closure fraction.

In Fig. 3.5, we adopt the same parameters as in Fig. 3.1 ($m_s = 64\,\mathrm{keV}$, $\sin^2 2\theta = 10^{-10}$, and $L_{e0} = 1.1 \times 10^{-3}$), but we modify the calculation by increasing the total scattering rate, Γ_e. In the calculations for Figs. 3.1 - 3.4, we have used a value of $y_e = 1.27$ in the total scattering rate, Eq. (3.16). However, as discussed in Sec.

3.3.1, this is a value that is relevant for temperatures much lower than those in our calculations.

We modify our calculations by assuming that the total scattering rate is proportional to the number of weak degrees of freedom that are in thermal equilibrium in the early universe. The value $y_e \approx 1.27$ stems from ν_e scattering on $e^{\pm}$ pairs and neutrinos and antineutrinos of all three active flavors. However, for the temperatures that we are concerned with here, there are also $\mu^{\pm}$ pairs and up, down, and strange quarks and antiquarks thermally populated in the early universe. By including all three quark colors and the fact that the weak current is left-handed, we modify the total scattering rate by a factor of 3.5. In other words, in testing the sensitivity to the scattering rate, we substitute $\Gamma_e(\epsilon, T) \rightarrow 3.5\Gamma_e(\epsilon, T)$.

This calculation shows that there is little effect in the resonant conversion regime. This result can be understood by noticing that $\gamma(\epsilon, T_{\text{max}}) \propto \Gamma_e^{-1}$ and $\delta T \propto \Gamma_e$. Therefore, the resonant production of sterile neutrinos is only weakly dependent on the total scattering rate. In Fig. 3.5 this is readily apparent, because the evolution of the resonant scaled momentum and the lepton number (and consequently the sterile neutrino production history) are nearly identical for $T \gtrsim 950\,\text{MeV}$.

The most dramatic effect of an increased scattering rate can be seen in the sterile neutrino production history after the resonance cessation event. Roughly 55percent of the final sterile neutrino relic density is produced nonresonantly (compared with 30 percent in the lower Γ_e case). This is because away from resonance the quantum Zeno effect is less efficient at suppressing sterile neutrino production, allowing the $\nu_e \rightarrow \nu_s$ rate to increase with Γ_e.

Another effect of the increased scattering rate is seen in the sterile neutrino energy distribution function. The most significant difference is that the high-ϵ peak is not as sharply peaked in this case. This is due to the combination of two processes. Nonresonant sterile neutrino production for $\epsilon > \epsilon_{\text{max}}$ is enhanced with a larger scattering rate, producing a less steep drop off. The merging of the two resonances that created the sharp peak in the low Γ_e case is less effective for a larger Γ_e. As discussed above, the peaks are broader with a smaller amplitude. Consequently, when these

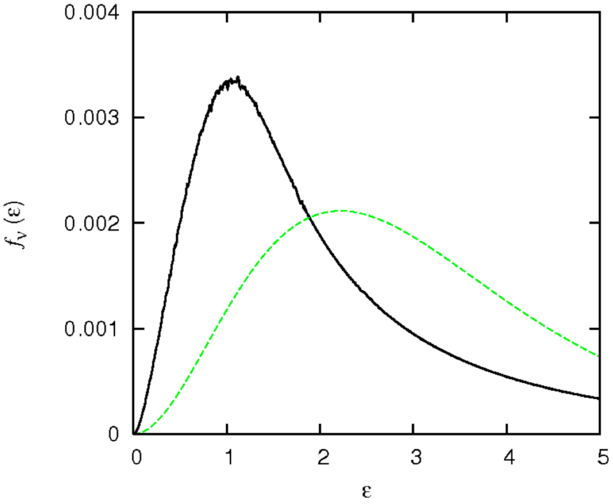

Figure 3.6: The sterile neutrino energy spectrum as a function of scaled momentum ϵ for an "in play" sterile neutrino dark matter candidate with $m_s = 12\,\mathrm{keV}$, $\sin^2 2\theta = 3.2\times 10^{-11}$, and $L_{e0} = 4.8\times 10^{-3}$ (solid curve). Also shown is a Fermi-Dirac spectrum normalized so that both spectra would produce the same number density of sterile neutrinos (dashed curve).

peaks come together, the result is a smaller cumulative sterile neutrino production.

To this point we have only discussed sterile neutrino dark matter candidates that are ruled out by the current X-ray observations. In Fig. 3.6 we present the energy spectrum for a sterile neutrino dark matter candidate that is still "in play" as far as the x-ray observations are concerned. To evade the x-ray limits, we must reduce the sterile neutrino mass and/or vacuum mixing angle. From the studies we conducted above, we know that the relic sterile neutrino closure fraction is more strongly dependent on mass than on mixing angle. Therefore, we must reduce both mass and mixing angle to get under the x-ray limits. However, to get the correct relic density we also increase the initial lepton number and the scattering rate as discussed above for Fig. 3.5.

For this calculation we use a sterile neutrino rest mass $m_s = 12\,\mathrm{keV}$ with vacuum mixing angle $\sin^2 2\theta = 3.2 \times 10^{-11}$ and initial lepton number $L_{e0} = 4.8 \times 10^{-3}$. The sterile neutrino properties are just below the current x-ray constraints, while the initial lepton number is much less than the best constraints on the lepton numbers in the early universe. We display only the energy spectrum because the other three panels do not provide much physical insight in this case.

For this case our calculations give $\epsilon_{\text{max}} \approx 200$, which means that the resonance sweeps through the entire ν_e distribution. As a result, the high-ϵ peak cannot be seen in Fig. 3.6. The mid-ϵ peak is at $\epsilon \approx 60$, so that is also missing. We are left with the low-ϵ peak and a long tail at higher ϵ that eventually disappears because of the scarcity of neutrinos in the ν_e distribution at these scaled momenta.

For this particular case the resonance cessation event occurs at $T \approx 100\,\text{MeV}$, but as discussed above, this corresponds to $\epsilon \approx 60$. The low-temperature resonance for more relevant values of ϵ (*i.e.*, $\epsilon \sim 3$) occurs at temperatures $\sim 170\,\text{MeV}$. Since the resonances persist to such low temperatures, there is very little nonresonant production of sterile neutrinos. As a result, the relic sterile neutrino density produced is relatively insensitive to the total scattering rate. However, this temperature is of interest in the early universe as it is the epoch of the QCD transition. The nature of this transition affects the specifics of the sterile neutrino production [46] but in broad brush should serve to enhance the final sterile neutrino closure fraction.

Also plotted on Fig. 3.6 is a Fermi-Dirac spectrum whose normalization is chosen to have an equivalent sterile neutrino density. The peak in the sterile neutrino spectrum is at $\epsilon \approx 1$, while the Fermi-Dirac spectrum peaks at $\epsilon \approx 2.2$. We see that a significant fraction of the total sterile neutrino density has smaller values of ϵ than in its Fermi-Dirac counterpart. Nonetheless, the high-ϵ tail of the distribution yields an average value of ϵ, $\langle\epsilon\rangle \approx 2$, compared to an average ϵ of 3.15 for a Fermi-Dirac spectrum. As a result, the sterile neutrino population produced in our calculations is "colder" by a factor of about 1.6 than an equivalent population with a Fermi-Dirac spectrum. This is qualitatively consistent with the findings in Ref. [16], but the sterile neutrino population here is not as cold.

Our numerical calculations show that the sterile neutrino rest mass, vacuum mixing angle, and initial lepton number parameters which produce the correct dark matter closure fraction, but which evade X-ray bounds, produce relic ν_s energy spec-

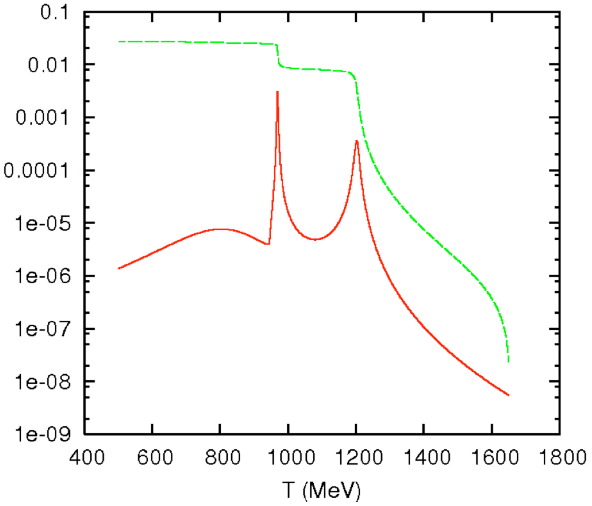

Figure 3.7: The solid curve is the sterile neutrino conversion rate per unit temperature interval, $|df_s/dT|$ for $\epsilon = 1$ in our calculations with $m_s = 64\,\mathrm{keV}$, $\sin^2 2\theta = 10^{-10}$, and $L_{e0} = 1.1 \times 10^{-3}$. The dashed curve shows the fractional difference between the rate inferred from a solution of the quantum kinetic equations to the rate implied by the quantum Zeno ansatz.

tra which are qualitatively similar to that in Fig. 3.6. Since this generic spectrum is skewed relative to a Fermi-Dirac form toward lower values of ϵ, viable dark matter sterile neutrinos which are produced via lepton number enhancement should be "colder" than their rest masses would suggest.

Finally, in Fig. 3.7 we perform a consistency check to determine the validity of the quantum Zeno ansatz that we have used throughout our calculations. To do this, we use the sterile neutrino parameters and initial lepton numbers employed in the calculations for Fig. 3.1 ($m_s = 64\,\mathrm{keV}$, $\sin^2 2\theta = 10^{-10}$, and $L_{e0} = 1.1 \times 10^{-3}$), and also use the smaller total scattering rate discussed above. We solve the quantum kinetic equations presented in Sec. 3.3.1 for $\epsilon = 1$, using the lepton number evolution from our calculations.

Plotted in Fig. 3.7 are the instantaneous $\nu_e \rightarrow \nu_s$ conversion rate per unit temperature interval, $|df_s/dT|$ (solid curve), and the fractional difference between the rate inferred from our solution to the quantum kinetic equations and the rate given by the quantum Zeno ansatz (dashed curve). Note that the actual conversion rate is always slightly larger than the rate from the quantum Zeno effect, but in general the two agree within a few percent. Note also that the differences change by an order of magnitude at the resonances.

Since the actual rate is possibly slightly higher than the rate we used with the quantum Zeno ansatz, we probably under-produce sterile neutrinos in our calculations. The interval between the two resonances is an important one in determining the final sterile neutrino production. If corrections on the order of a percent occurred for all our values of ϵ, this could increase the temperature of the resonance cessation event and, in turn, increase the ultimate relic sterile neutrino density, possibly in a nonlinear fashion. Our numerical calculations show that a 1 % increase in the conversion rate gives a 0.3 % increase in relic sterile neutrino density. We conclude that a small change in the conversion rate does not lead to a significant change in the relic sterile neutrino density.

3.6 Conclusions

One option for producing viable sterile neutrino dark matter is lepton number enhancement of scattering-induced decoherence. The calculations presented here address the basic physics of this production process. A key conclusion of our work is that the interplay of lepton number depletion and resonant sterile neutrino production leads to a set of generic peak features in the relic sterile neutrino energy spectrum. We have studied how these peaks depend on the assumed initial lepton number, the magnitude of the assumed active-sterile coupling (*i.e.*, the vacuum mixing angle), and the sterile neutrino rest mass. We conclude that relic sterile neutrinos with parameters that evade x-ray constraints will have a characteristic single-peak energy spectrum. This spectrum will be “cold” compared to a Fermi-Dirac form spectrum with the same integrated relic number density. This could relax to some extent Lyman-alpha forest constraints on sterile neutrino rest mass [47].

We have compared the widely-used quantum Zeno ansatz with a full quantum kinetic equation treatment of scattering-induced decoherence production of sterile neutrinos in the early universe. Our conclusion is that the quantum Zeno approximation is adequate, at least during the epoch in the early universe when $\sim$ keV mass sterile neutrinos are produced.

Finally, we should note the limitations of this study and point out the topics that need further detailed examination. The calculations presented here are crafted to study the physical effects which determine relic sterile neutrino energy spectra. They only treat schematically the microphysics of scattering degrees of freedom and finite temperature in-medium effects. We have attempted to gauge the sensitivity of final relic ν_s densities and energy spectra to these issues by simply varying the prescription for active neutrino scattering rates. Though we find that our generic spectral features are relatively insensitive to changes in these rates, our calculations nevertheless cannot serve to predict relic densities accurately.

At least three aspects of our calculations for sterile neutrino production and lepton number depletion are simplistic: (1) we have allowed only a single channel, $\nu_e \to \nu_s$, for sterile neutrino production; (2) we have taken initial, preexisting lepton numbers in all active neutrino species to be the same; and (3) we have not allowed mixing between active neutrino flavors. As for the last point, the study in Ref. [19] suggests that dynamically including active-active mixing should be roughly similar to having a larger initial value of L_{e0} in our model. The idea being that as ν_e are converted to ν_s, some ν_μ and ν_τ neutrinos convert into ν_e. In essence then, the net lepton number in the mu and tau neutrino seas serves as a reservoir that "feeds" the ν_e sea as sterile neutrinos are produced. In fact, the measured active-active mixing parameters may suggest mixing between the flavors is efficient and that equality of lepton numbers is a plausible assumption [22]. A larger reservoir of active neutrinos feeding into $\nu_e \to \nu_s$ would not change the *qualitative* aspects of our conclusions on the interplay of lepton number depletion and neutrino asymmetry-enhanced sterile neutrino production in the early universe.

In contrast, if there were more than one kind of sterile neutrino, or if there were multiple channels of active-sterile conversion (*e.g.*, $\nu_{\mu,\tau} \to \nu_s$ in addition to $\nu_e \to \nu_s$), then both lepton number depletion and sterile neutrino production histories might be different than those calculated here. In fact, a key conclusion of our work is that these histories, as well as the relic sterile neutrino energy spectrum that goes with them, are a product of the potentially complicated coupling between the sterile neutrino production channels and the way lepton numbers evolve. This is a rich problem which deserves further consideration.

This work was supported in part by NSF Grant PHY-04-00359 at UCSD. C.T.K. would like to thank J. Kao for useful discussions on the computational aspects of this work and the ARCS Foundation, Inc. for financial support. We would like to thank A. Kusenko for valuable conversations.

Chapter 3, in full, is a reprint of material previously published as C. T. Kishimoto and G. M. Fuller, “Lepton Number-Driven Sterile Neutrino Production in the Early Universe”, *Physical Review* D**78**, 023524 (2008). I was the primary investigator and author of this paper.

Bibliography

[1] S. Dodelson and L. M. Widrow, Physical Review Letters **72**, 17 (1994).

[2] K. Abazajian, G. M. Fuller and W. H. Tucker, Astrophysical Journal **562**, 593 (2001).

[3] K. Abazajian, G. M. Fuller and M. Patel, Physical Review D **64**, 023501 (2001).

[4] A. D. Dolgov and S. H. Hansen, Astroparticle Physics **16**, 339 (2002).

[5] K. Abazajian and S. M. Koushiappas, Physical Review D **74**, 023527 (2006).

[6] A. Boyarsky, A. Neronov, O. Ruchayskiy and M. Shaposhnikov, Physical Review D **74**, 103506 (2006).

[7] A. Boyarsky, A. Neronov, O. Ruchayskiy and M. Shaposhnikov, Monthly Notices of the Royal Astronomical Society **370**, 213 (2006).

[8] A. Boyarsky, A. Neronov, O. Ruchayskiy, M. Shaposhnikov and I. Tkachev, Physical Review Letters **97**, 261302 (2006).

[9] A. Palazzo, D. Cumberbatch, A. Slosar and J. Silk, Physical Review D **76**, 103511 (2007).

[10] H. Yüksel, J. F. Beacom and C. R. Watson, Physical Review Letters **101**, 121301 (2008).

[11] C. R. Watson, J. F. Beacom, H. Yüksel and T. P. Walker, Physical Review D **74**, 033009 (2006).

[12] M. Shaposhnikov and I. Tkachev, Physics Letters B **639**, 414 (2006).

[13] A. Kusenko, Physical Review Letters **97**, 241301 (2006).

[14] K. Petraki and A. Kusenko, Physical Review D **77**, 065014 (2008).

[15] K. Petraki, Physical Review D **77**, 105004 (2008).

[16] X. Shi and G. M. Fuller, Physical Review Letters **83**, 3120 (1999).

[17] R. Foot, M. J. Thomson and R. R. Volkas, Physical Review D **53**, R5349 (1996).

[18] X. Shi, Physical Review D **54**, 2753 (1996).

[19] K. Abazajian, N. F. Bell, G. M. Fuller and Y. Y. Y. Wong, Physical Review D **72**, 063004 (2005).

[20] C. T. Kishimoto, G. M. Fuller and C. J. Smith, Physical Review Letters **97**, 141301 (2006).

[21] J. P. Kneller, R. J. Scherrer, G. Steigman and T. P. Walker, Physical Review D **64**, 123506 (2001).

[22] K. N. Abazajian, J. F. Beacom and N. F. Bell, Physical Review D **66**, 013008 (2002).

[23] Y. Y. Y. Wong, Physical Review D **66**, 025015 (2002).

[24] A. D. Dolgov, S. H. Hansen, S. Pastor, S. T. Petcov, G. G. Raffelt and D. V. Semikoz, Nuclear Physics B **632**, 363 (2002).

[25] A. Cuoco, F. Iocco, G. Mangano, G. Miele, O. Pisanti and P. D. Serpico, International Journal of Modern Physics A **19**, 4431 (2004).

[26] P. D. Serpico and G. G. Raffelt, Physical Review D **71**, 127301 (2005).

[27] V. Simha and G. Steigman, Journal of Cosmology and Astroparticle Physics **8**, 011 (2008).

[28] R. Foot and R. R. Volkas, Physical Review Letters **75**, 4350 (1995).

[29] R. Foot and R. R. Volkas, Physical Review D **55**, 5147 (1997).

[30] P. Di Bari and R. Foot, Physical Review D **65**, 045003 (2002).

[31] S. P. Mikheyev and A. Y. Smirnov, Yadernaya Fizika **42**, 1441 (1985).

[32] L. Wolfenstein, Physical Review D **17**, 2369 (1978).

[33] B. H. J. McKellar and M. J. Thomson, Physical Review D **49**, 2710 (1994).

[34] G. Sigl and G. Raffelt, Nuclear Physics B **406**, 423 (1993).

[35] D. Nötzold and G. Raffelt, Nuclear Physics B **307**, 924 (1988).

[36] G. M. Fuller, R. W. Mayle, J. R. Wilson and D. N. Schramm, Astrophysical Journal **322**, 795 (1987).

[37] N. F. Bell, R. R. Volkas and Y. Y. Y. Wong, Physical Review D **59**, 113001 (1999).

[38] B. Misra and E. C. G. Sudarshan, Journal of Mathematical Physics **18**, 756 (1977).

[39] D. Boyanovsky and C. M. Ho, Journal of High Energy Physics **07**, 30 (2007).

[40] D. Boyanovsky and C. M. Ho, Physical Review D **76**, 085011 (2007).

[41] A. R. Curtis, Numerische Mathematik **16**, 268 (1970).

[42] M. Viel, J. Lesgourgues, M. G. Haehnelt, S. Matarrese and A. Riotto, Physical Review D **71**, 063534 (2005).

[43] K. Abazajian, Physical Review D **73**, 063513 (2006).

[44] U. Seljak, A. Makarov, P. McDonald and H. Trac, Physical Review Letters **97**, 191303 (2006).

[45] D. N. Spergel, R. Bean, O. Doré, M. R. Nolta, C. L. Bennett, J. Dunkley, G. Hinshaw, N. Jarosik, E. Komatsu, L. Page, H. V. Peiris, L. Verde, M. Halpern, R. S. Hill, A. Kogut, M. Limon, S. S. Meyer, N. Odegard, G. S. Tucker, J. L. Weiland, E. Wollack and E. L. Wright, Astrophysical Journal Supplement Series **170**, 377 (2007).

[46] K. N. Abazajian and G. M. Fuller, Physical Review D **66**, 023526 (2002).

[47] D. Boyanovsky, Physical Review D **77**, 023528 (2008).

Chapter 4

Neutrino-Accelerated Hot Hydrogen Burning

Throughout this chapter, the standard short-hand nomenclature for nuclear reactions is used $A(B,C)D$, which is equivalent to the reaction $A + B \rightarrow C + D$. For example, the capture of an electron anti-neutrino on a proton to form a neutron and positron is written as $p(\bar{\nu}_e, e^+)n$.

4.1 Abstract

We examine the effects of significant electron anti-neutrino fluxes on hydrogen burning. Specifically, we find that the bottleneck weak nuclear reactions in the traditional pp-chain and the hot CNO cycle can be accelerated by anti-neutrino capture, increasing the energy generation rate. We also discuss how anti-neutrino capture reactions can alter the conditions for break out into the *rp*-process. We speculate on the impact of these considerations for the evolution and dynamics of collapsing very- and super- massive compact objects.

4.2 Introduction

Hydrogen burning involves the conversion of four protons into an alpha particle, two positrons, neutrinos and photons. The principal bottleneck involved in this process is the weak interaction conversion of protons into neutrons. For decades the primary mechanisms of hydrogen burning have been an astronomical staple. Bethe and Critchfield [1] first elucidated the proton-proton chain (pp-chain) where the weak conversion is accomplished by two protons interacting to become a deuteron, $p(p,\nu_e e^+)d$. von Weizsäcker [2] and Bethe [3] independently described the CNO cycle, where carbon is used as a catalyst in hydrogen burning, and the weak conversion of protons to neutrons occurs through the positron decay of isotopes of oxygen with half lives of about 100 seconds.

A large flux of electron anti-neutrinos ($\bar{\nu}_e$) could alter the hydrogen burning paradigm. Anti-neutrino capture could perform the necessary conversion of protons to neutrons. The $\bar{\nu}_e$-capture cross sections of relevance are very small, but depend strongly on neutrino energy. The smallness of these cross sections allows energetic neutrinos to escape from deep within a compact object, where the temperature and other energy scales are high, and freely stream to where hydrogen burning is occurring. Nevertheless, if $\bar{\nu}_e$-capture is to have a significant effect on hot hydrogen burning, a truly prodigious flux ($\phi_{\bar{\nu}_e} \gtrsim 10^{40}$ cm^{-2} s^{-1}) and large neutrino energy ($\langle E_{\bar{\nu}_e} \rangle \gtrsim$ a few MeV) would be necessary. It should be kept in mind, however, that to affect hydrogen burning, the $\bar{\nu}_e$-capture rates need only be comparable to the corresponding positron decay rates.

The difficulty would be to find an environment capable of producing these fluxes of neutrinos, yet quiescent enough that simple hydrogen burning could be relevant, and the products of such burning could be ejected into space. High entropy electron-positron plasmas are efficient engines for the production of neutrinos and anti-neutrinos of all flavors. Possible environments that may merit future investigations into the effects of anti-neutrino capture on hydrogen burning include high mass accretion disks and collapsing very- and super- massive objects.

In this paper, we investigate the effects of a prodigious neutrino flux on hot hydrogen burning. In section 4.3 we point out the effects of anti-neutrino capture on the rate limiting steps in both the pp-chain and the β-limited CNO cycle, and its implications for the energy generation rates. In section 4.4, we examine the consequences for the *rp*-process and energy generation mechanisms. In section 4.5, we consider the case of a supermassive star collapsing on the general relativistic Feynman-Chandrasekhar instability, and the effects of its internal neutrino production on hydrogen burning in its envelope. We give conclusions in section 4.6.

4.3 Neutrino-Induced Hydrogen Burning Mechanisms

The rate limiting step in the pp-chain is the weak interaction conversion of two protons into a deuteron, a positron, and an electron neutrino. A significant flux of electron anti-neutrinos allows an alternate mechanism to be favored, where anti-neutrino capture on a proton creates a neutron and a positron ($\bar{\nu}_e + p \to n + e^+$ has been considered in supermassive objects in Refs. [4] and [5]). This step would be followed by a fast radiative proton capture to form a deuteron. Comparing the two reaction rates: $p(p, \nu_e e^+)d$ vs. $p(\bar{\nu}_e, e^+)n(p, \gamma)d$, we find that for the prodigious anti-neutrino fluxes discussed in the introduction ($\phi_{\bar{\nu}_e} \gtrsim 10^{40}$ cm^{-2} s^{-1}, $\langle E_{\bar{\nu}_e} \rangle \gtrsim$ a few MeV) the anti-neutrino capture path is significantly faster in relevant astrophysical environments. This provides not only a new reaction path for hydrogen burning, but increases the energy generation rate by several orders of magnitude.

The β-limited CNO cycle, or hot CNO cycle, proceeds at a rate dictated by the positron decay of ^{14}O and ^{15}O, with half lives of 71 s and 122 s, respectively (see, *e.g.*, Refs. [6] and [7]). These decays likewise could be augmented by electron anti-neutrino capture, $^{14}\mathrm{O}(\bar{\nu}_e, e^+)^{14}\mathrm{N}$ and $^{15}\mathrm{O}(\bar{\nu}_e, e^+)^{15}\mathrm{N}$. Figure 4.1 shows the acceleration of the relevant weak rates as a function of total electron anti-neutrino flux for an assumed Fermi-Dirac $\bar{\nu}_e$-energy spectrum with average $\bar{\nu}_e$-energy $\langle E_{\bar{\nu}_e} \rangle = 10$ MeV and zero

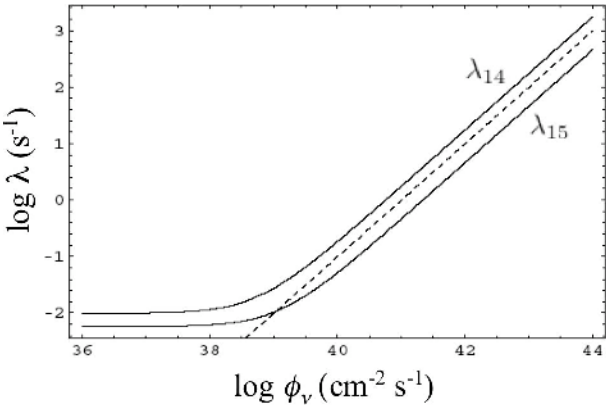

Figure 4.1: Key weak decay rates as a function of electron anti-neutrino flux, assuming a Fermi-Dirac $\bar{\nu}_e$-energy spectrum with zero chemical potential and average $\bar{\nu}_e$-energy $\langle E_{\bar{\nu}_e} \rangle = 10$ MeV. The solid lines, labeled λ_{14} and λ_{15} are the total weak decay rates of ^{14}O and ^{15}O, respectively, through positron decay and anti-neutrino capture. The dashed line is the rate of conversion of a proton to a neutron via anti-neutrino capture alone.

chemical potential. The flux at which anti-neutrino capture becomes important scales appoximately as $\langle E_{\bar{\nu}_e} \rangle^{-2}$. For a large enough flux ($\phi_{\bar{\nu}_e} \gtrsim 10^{39}$ cm^{-2} s^{-1} in the case of Figure 4.1), the reaction rates are proportional to the incident flux of electron anti-neutrinos. Our weak rate calculations are described in Appendix 4.A.

Additionally, the CNO cycle is accelerated by the presence of free neutrons. The strong interaction reactions $^{15}\mathrm{O}(n,p)^{15}\mathrm{N}$ and $^{14}\mathrm{O}(n,p)^{14}\mathrm{N}$ have a significantly larger cross section than the electromagnetic reaction $n(p,\gamma)d$. As a result, neutrons are diverted from the modified pp-chain into the CNO cycle. Figure 4.2 shows how the neutrons created by $p(\bar{\nu}_e, e^+)n$ are distributed between the competing reactions $^{15}\mathrm{O}(n,p)^{15}\mathrm{N}$, $^{14}\mathrm{O}(n,p)^{14}\mathrm{N}$ and $n(p,\gamma)d$. Notice that for an assumed Fermi-Dirac $\bar{\nu}_e$-energy spectrum with $\langle E_{\bar{\nu}_e} \rangle = 10$ MeV and zero chemical potential, the ratio of neutron captures on ^{15}O to ^{14}O to p is approximately 4.5 : 2 : 1 for a large range of $\bar{\nu}_e$-fluxes. The calculations used in producing Figure 4.2 employed (n,p) rates takn from Ref. [8]. It should be kept in mind that the branching ratios apparent in Figure 4.2 may vary with different reaction rate sets (see, *e.g.*, the NACRE compilation [9]). However, general qualitative conclusions and trends drawn from Figure 4.2 are valid.

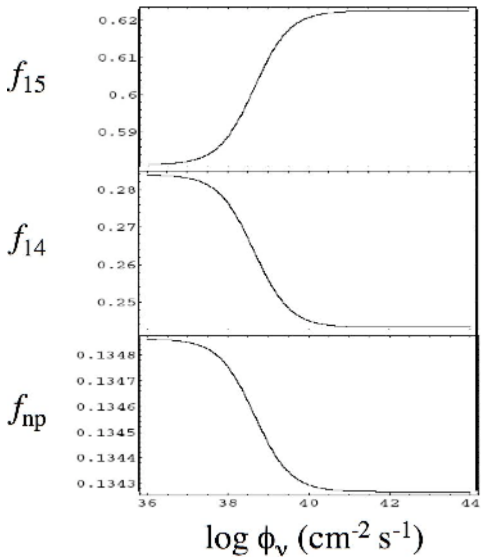

Figure 4.2: Fraction of neutron captures on ^{15}O (f_{15}), ^{14}O (f_{14}) and p (f_{np}), assuming a Fermi-Dirac $\bar{\nu}_e$-energy spectrum with zero chemical potential, average $\bar{\nu}_e$-energy $\langle E_{\bar{\nu}_e} \rangle = 10$ MeV and $X/Z' = 100$, where X is the hydrogen mass fraction and Z' is the mass fraction in carbon, nitrogen and oxygen isotopes.

Figure 4.3 illustrates the most significant reaction flow paths involved in hydrogen burning when a significant $\bar{\nu}_e$-flux is present. The pp-chain is modified as anti-neutrino capture allows the circumvention of the slow $p(p, \nu_e e^+)d$ reaction. Also included are the triple-alpha process, which would provide a path between the pp-chain and CNO cycle, and the break out into the rp-process via $^{15}\mathrm{O}(\alpha,\gamma)^{19}\mathrm{Ne}(p,\gamma)^{20}\mathrm{Na}$ [10].

4.4 Side Effects

A large flux of electron anti-neutrinos certainly accelerates the weak rates that provide the bottleneck in hot hydrogen burning. However, since this flux also increases the rates of other positron decays, a number of side effects are possible.

A principal mechanism for break out into the rp-process involves the reaction path $^{15}\mathrm{O}(\alpha,\gamma)^{19}\mathrm{Ne}(p,\gamma)^{20}\mathrm{Na}$. The criteria for break out into the rp-process can be found in the competition between proton capture on ^{19}Ne, and the decay of ^{19}Ne

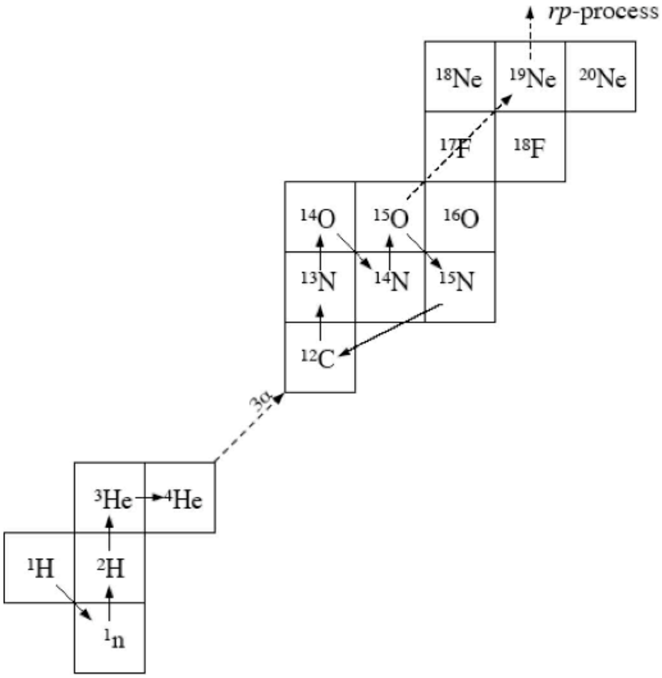

Figure 4.3: Qualitative picture of hydrogen burning under the influence of a prodigious electron anti-neutrino flux. Shown are a modified pp-chain, β-limited CNO cycle, and the less significant triple-α reaction and break-out to the *rp*-process.

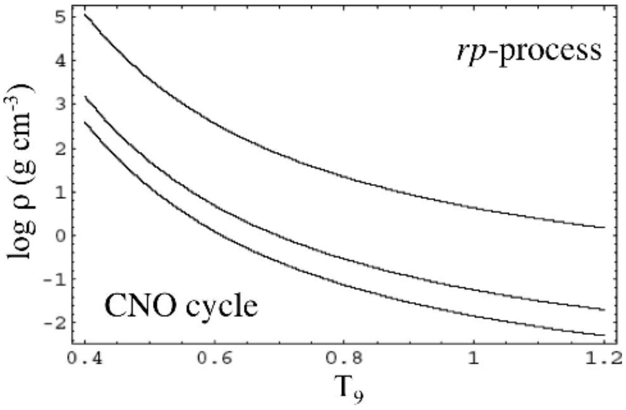

Figure 4.4: Conditions for break-out into the *rp*-process, assuming a Fermi-Dirac $\bar{\nu}_e$-energy spectrum, zero chemical potential, and $\langle E_{\bar{\nu}_e} \rangle = 10$ MeV. The plotted contours are for, in ascending order, $\phi_{\bar{\nu}_e} = 10^{38,40,42}$ cm^{-2} s^{-1}. Zero neutrino flux is indistinguishable from $\phi_{\bar{\nu}_e} = 10^{38}$ cm^{-2} s^{-1}.

through positron emission and now, anti-neutrino capture. Thus for densities and temperatures that satisfy the inequality

$$\rho X \lambda_{p\gamma}(^{19}\mathrm{Ne}) > \lambda_w(^{19}\mathrm{Ne}), \tag{4.1}$$

break out into the *rp*-process will occur [10]. Here the density ρ is in $\mathrm{g\,cm^{-3}}$, X is the hydrogen mass fraction, $\lambda_w(^{19}\mathrm{Ne})$ is the total weak decay rate of ^{19}Ne (positron emission and $\bar{\nu}_e$-capture), and $\lambda_{p\gamma} = N_A \langle \sigma v \rangle_{p\gamma}$, where N_A is Avagadro's number and the thermally averaged product of cross section and speed is taken from Ref. [8]. Note that the more recent work in Ref. [9] gives rates for $^{19}\mathrm{Ne}(p,\gamma)^{20}\mathrm{Na}$ which differ from those from Ref. [8], especially at low temperatures. However, for the range of temperature conditions of interest here, our adopted rate for this process lies within the range of rates predicted in Ref. [9].

Including a large flux of electron anti-neutrinos would result in higher weak decay rates (λ_w). This increase in the right hand side of equation (4.1) would require an increase in temperature (increasing $\lambda_{p\gamma}(^{19}\mathrm{Ne})$) for a given density at which break out into the *rp*-process would occur. Figure 4.4 shows the effects of an electron anti-neutrino flux on the conditions necessary for break out into the *rp*-process.

The pp-chain is the dominant process of energy generation in the sun, while the

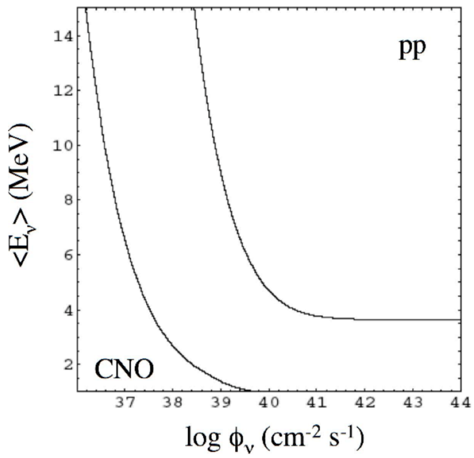

Figure 4.5: Comparison of energy generation rates for the pp-chain and CNO cycle at a temperature of 5×10^8 K. The contours are where the energy generation rates are equal for the two hydrogen burning mechanisms for values of $X/Z' = 10, 100$ (from right to left). Larger $\bar{\nu}_e$-fluxes and average energies favors the pp-chain, while smaller fluxes and average energies favor the CNO cycle.

CNO cycle is dominant in stars that are more massive. However, with a large flux of electron anti-neutrinos, these processes become independent of temperature so long as the temperature is high enough to guarantee that proton capture remains comparatively fast. A high flux of electron anti-neutrinos allows the pp-chain to compete favorably with the CNO cycle. For example, Pruet, et al. [11] have studied nucleosynthesis in supernova winds where hydrogen "burning" is completely dominated by ν_e and $\bar{\nu}_e$ capture on free nucleons (see also Ref. [12]).

The scarcity of ^{15}O in comparison to free protons means that for large anti-neutrino fluxes and average energies, the pp-chain is the dominant mechanism in hydrogen burning at temperatures that the CNO cycle would traditionally dominate. Figure 4.5 shows a comparison between the energy generation rates of the pp-chain and the CNO cycle for $X/Z' = 10$ and 100, where X is the hydrogen mass fraction and Z' is the mass fraction in carbon, nitrogen, and oxygen isotopes. For large anti-neutrino fluxes and average energies, the pp-chain is the dominant energy generation mechanism, while for low fluxes and average energies the CNO cycle takes over.

4.5 Example: Supermassive Stars

Now we consider the case of a supermassive star, a star so massive that it collapses on the general relativistic Feynman-Chandrasekhar instability ($M \gtrsim 5 \times 10^4 M_\odot$) [13]. If such objects did exist, for example in the early universe, their homologous cores would emit copious fluxes of neutrinos and anti-neutrinos of all flavors during their collapse [14]. Ref. [14] examined the collapsing core of a supermassive star, calculating the luminosity and energy spectrum of neutrinos emitted. The total neutrino luminosity was found to be

$$L_\nu \approx 2.8 \times 10^{57} \left(M_5^{\mathrm{HC}}\right)^{-1.5} \text{ erg s}^{-1}, \tag{4.2}$$

where M_5^{HC} is the mass of the homologous core in units of $10^5 M_\odot$. Additionally they found the energy spectrum of neutrinos of all flavors to fit remarkably well to a Fermi-Dirac spectrum with a higher temperature than the central plasma temperature ($T_\nu \approx 1.6T$) and a degeneracy parameter (chemical potential divided by temperature) $\eta_\nu \approx 2$. The ν_e and $\bar{\nu}_e$ emissivity in these objects predominantly comes from thermal electron-positron pair annihilation. (See Ref. [15] for a complete discussion of neutrino/antineutrino production processes.)

We can check the effect of this flux of neutrinos and antineutrinos on the nuclear physics in the gas in the envelope of the star. As a point of reference, we choose a radius of 100 Schwarzschild radii ($r = 3 \times 10^{12} M_5^{\mathrm{HC}}$ cm) where the gravitational binding energy of a nucleon is approximately equal to the nuclear energy liberated in these reactions, so there is a chance that any new nuclear physics that occurs as a result of $\bar{\nu}_e$-capture could be relevant. By "relevant" we mean that it is conceivable that material from this location could avoid being swallowed by the black hole forming in the core. Only a detailed simulation with general relativistic hydrodynamics could reveal whether or not material affected by $\bar{\nu}_e$-capture is ever ejected into space. We are now free to repeat the analyses done above, but with one free parameter, the mass of the collapsing homologous core.

Figure 4.6 shows the acceleration of the relevant weak rates as a function of homologous core mass. The anti-neutrino capture rate is proportional to $(M_5^{\mathrm{HC}})^{-4}$.

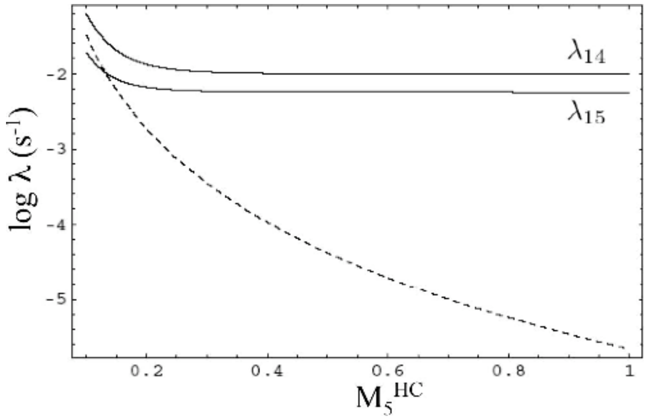

Figure 4.6: Rates of relevant weak decays at a distance of 100 Schwartzschild radii from the center of a supermassive star with homologous core mass $M_5^{\rm HC} \times 10^5 M_\odot$. As in Figure 4.1, the solid lines are the total rates of decay of ^{14,15}O, and the dashed line is the proton to neutron conversion rate through anti-neutrino capture alone.

We see that the effects of anti-neutrino capture on the decay rates of ^{14}O and ^{15}O become insignificant for large homologous core masses ($M_5^{\rm HC} \gtrsim 0.4$). If supermassive stars ever formed, it is conceivable that they were in the first generation of stars with primordial initial abundances. In this case the CNO cycle would be negligible, at least initially [13]. However, even in this case, the energy generation rate of the pp-chain would be boosted by several orders of magnitude. It would be interesting to see if this added energy source would have a discernible effect on the eventual fate of a collapsing supermassive star.

Including a hydrogen burning phase in the final stages of the collapse of a supermassive star may affect the eventual fate of its baryons. Hydrodynamic, post-Newtonian calculations done in Ref. [13] show that initially metal-free supermassive stars will collapse to black holes. A fully relativistic simulation in axial symmetry deduces that the supermassive star collapses to a black hole surrounded by some remaining gas in an ambient disk [16].

The principal nucleosynthetic issue is whether any material that had experienced $\bar{\nu}_e$ capture-affected hydrogen burning escapes being incorporated into a black hole. Of course, there is the prior issue of whether material at the relatively low temperatures and densities which characterize hydrogen burning ever experiences high $\bar{\nu}_e$-fluxes. Both issues are related: to see nucleosynthesis products of $\bar{\nu}_e$ capture-affected hydrogen burning, the material must be ejected before the point at which nuclear burning proceeds past simple hydrogen burning and approaches or attains nuclear statistical equilibrium (NSE). We are skeptical that these conditions can be met. Fully relativistic numerical simulations could settle these issues.

Obviously, the NSE nucleosynthetic yield is uninteresting in the context of this paper. However, a mass shedding scenario could be conducive to conditions that favor hydrogen burning and the *rp*-process. Speeding up weak decays could affect the relative abundances of the *rp*-process elements. A simulation that follows these species and their chemical reactions would be necessary to address this issue.

4.6 Conclusions

In this paper we have examined the effects of a prodigious flux of electron anti-neutrinos on hydrogen burning. We have found that the traditional positron decay bottlenecks in hydrogen burning can be removed and replaced by much faster $\bar{\nu}_e$-capture reactions under some conditions. This would result in an increase of several orders of magnitude in the energy generation rate over what would be expected without such a flux.

Additionally, the $\bar{\nu}_e$-flux would alter the conditions necessary for break-out into the *rp*-process, increasing the temperature necessary to do so at a given density. If conditions allow the break-out into the *rp*-process, we could expect an acceleration of the flow toward the iron-peak facilitated by and accelerated by $\bar{\nu}_e$-capture.

When applied to the neutrino flux emitted in the final stages of the collapse of a supermassive star, interesting changes from current simulations may occur on the lower end of the supermassive star mass spectrum. Whether or not these effects are relevant, remains an open question that can only be answered by simulations that are able to include hydrogen burning during the final collapse of the star.

Important issues that remain open include finding an astrophysical environment where the effects discussed here could take place. Accretion disks surrounding black holes may provide a combination of high accretion rates and hot, high entropy disks which could produce the necessary fluxes of electron anti-neutrinos. (See for example Ref. [17] for a discussion of neutrino emission in lower mass accretion disks.) Supermassive stars may exhibit this effect, though there is uncertainty related to whether or not these objects ever existed. Computer simulations would be useful to determine any changes in the expected nucleosynthetic yield, and the effects of their possible distribution into the surrounding IGM.

We would like to thank S. E. Woosley, Y.-Z. Qian and A. Heger for useful discussions. This work was supported in part by NSF grant PHY-04-00359 and the TSI collaboration's DOE SciDAC grant at UCSD. C.T.K. would like to acknowledge a fellowship from the ARCS Foundation, Inc.

Chapter 4, in full, is a reprint (with the exception of the citation style, which has been revised to ensure consistency with the rest of the dissertation) of material previously published as C. T. Kishimoto and G. M. Fuller, "Neutrino-Accelerated Hot Hydrogen Burning", *Astrophysical Journal* **656**, 1104 (2007). I was the primary investigator and author of this paper.

Appendix 4.A Calculation of Weak Rates

In this work we calculate the $\bar{\nu}_e$-capture rates in the manner described in Refs. [18–20]. We employ measured discrete states only.

Our ^{14}O$(\bar{\nu}_e, e^+)^{14}$N rate calculation includes only the ^{14}O ground state (spin and parity $J^\pi = 0^+$) and the measured weak branches to the ^{14}N ground state ($J^\pi = 0^+$, $\log_{10} ft = 7.3$), first excited state ($J^\pi = 1^+$, $\log_{10} ft = 3.5$), and second excited state ($J^\pi = 1^+$, $\log_{10} ft = 3.1$). Contributions to the stellar rate from thermal excitation of parent states are small here as a result of the high first excited state excitation energy (5.17 MeV) and the temperatures of interest. Likewise, branches to higher excited states in ^{14}N are not significant. A possible exception is the first isobaric analog state in ^{14}N ($J^\pi = 0^+$) at excitation energy of 8.62 MeV. This branch will have a large matrix element but will be Q-value-hindered relative to the $0^+ \rightarrow 0^+$ ground state to first excited state, pure Fermi branch.

Our $^{15}\mathrm{O}(\bar{\nu}_e, e^+)^{15}\mathrm{N}$ rate calculation includes only the ground state ($J^\pi = 1/2^-$) branch. This channel has a large matrix element, corresponding to $\log_{10} ft = 3.6$. Branches to ^{15}N excited states will not be significant. ^{15}N states below 9.15 MeV excitation energy have positive parity and the branches from the ^{15}O ground state to them will be forbidden. We note, however, that ^{15}O and ^{15}N are isospin mirrors. This can be a significant fact for stellar weak interaction rates, as it implies large Fermi and Gamow-Teller matrix elements coupling each parent state with its daughter isobaric analog state [18, 19]. Thermal excitation of ^{15}O excited states would open weak branches to corresponding isobaric analog states in ^{15}N. This is not likely at the temperatures of interest because the first excited state of ^{15}O is at about 5.2 MeV excitation.

Our calculation of the $^{19}\mathrm{Ne}(\bar{\nu}_e, e^+)^{20}\mathrm{Na}$ rate includes only the ground state of ^{19}Ne ($J^\pi = 1/2^+$) and branches to the ground ($J^\pi = 1/2^+$) and third excited state ($J^\pi = 3/2^+$) of ^{19}F. The first of these branches, with $\log_{10} ft = 3.2$, dominates the rate. We note, however, that ^{19}Ne and ^{19}F are isospin mirrors. Since temperatures are high near CNO cycle breakout, thermal excitation of the first ($J^\pi = 5/2^+$) and second ($J^\pi = 1/2^-$) excited states can be expected to carry a fraction of the total weak rate. However, on the assumption that the matrix elements for these branches are identical to that for the ground-to-ground transitions, inclusion of these branches makes little difference ($< 1\%$) for the rates and our conclusions.

Bibliography

[1] H. A. Bethe and C. L. Critchfield, Physical Review **54**, 248 (1938).

[2] C. F. von Weizsäcker, Physik. Zeitschr. **39**, 633 (1938).

[3] H. A. Bethe, Physical Review **55**, 434 (1939).

[4] S. E. Woosley, Nature **269**, 42 (1977).

[5] G. M. Fuller and X. Shi, Astrophysical Journal **487**, L25 (1997).

[6] F. Hoyle and W. A. Fowler, Report on the properties of massive objects, in *Quasi-Stellar Sources and Gravitational Collapse*, edited by I. Robinson, A. Schild. and E. L. Schucking, p. 62, 1965.

[7] J. Audouze, J. W. Truran and B. A. Zimmerman, Astrophysical Journal **184**, 493 (1973).

[8] G. R. Caughlan and W. A. Fowler, Atomic Data and Nuclear Data Tables **40**, 283 (1988).

[9] G. Vancraeynest, P. Decrock, M. Gaelens, M. Huyse, P. Van Duppen, C. R. Bain, T. Davinson, R. D. Page, A. C. Shotter, P. J. Woods, F. Binon, P. Duhamel, J. Vanhorenbeeck, R. Coszach, T. Delbar, W. Galster, J. S. Graulich, P. Leleux, E. Liénard, P. Lipnik, C. Michotte, A. Ninae, J. Vervier, H. Herndl, H. Oberhummer, C. Sükösd and M. Wiescher, Physical Review C **57**, 2711 (1998).

[10] R. K. Wallace and S. E. Woosley, Astrophysical Journal Supplement Series **45**, 389 (1981).

[11] J. Pruet, R. D. Hoffman, S. E. Woosley, H.-T. Janka and R. Buras, Astrophysical Journal **644**, 1028 (2006).

[12] Y.-Z. Qian, G. M. Fuller, G. J. Mathews, R. W. Mayle, J. R. Wilson and S. E. Woosley, Physical Review Letters **71**, 1965 (1993).

[13] G. M. Fuller, S. E. Woosley and T. A. Weaver, Astrophysical Journal **307**, 675 (1986).

[14] X. Shi and G. M. Fuller, Astrophysical Journal **503**, 307 (1998).

[15] N. Itoh, H. Hayashi, A. Nishikawa and Y. Kohyama, Astrophysical Journal Supplement Series **102**, 411 (1996).

[16] M. Shibata and S. L. Shapiro, Astrophysical Journal **572**, L39 (2002).

[17] R. Surman, G. C. McLaughlin and W. R. Hix, Astrophysical Journal **643**, 1057 (2006).

[18] G. M. Fuller, W. A. Fowler and M. J. Newman, Astrophysical Journal Supplement Series **42**, 447 (1980).

[19] G. M. Fuller, W. A. Fowler and M. J. Newman, Astrophysical Journal **252**, 715 (1982).

[20] G. M. Fuller and B. S. Meyer, Astrophysical Journal **453**, 792 (1995).

Chapter 5

Quantum Coherence of Relic Neutrinos

5.1 Abstract

We argue that in at least a portion of the history of the universe the relic background neutrinos are spatially-extended, coherent superpositions of mass states. We show that an appropriate quantum mechanical treatment affects the neutrino mass values derived from cosmological data. The coherence scale of these neutrino flavor wavepackets can be an appreciable fraction of the causal horizon size, raising the possibility of spacetime curvature-induced decoherence.

5.2 Introduction

In this letter we point out a curious feature of the neutrino background and the potential implications of this both for models of neutrino clustering and for astrophysical limits on neutrino rest mass. With Standard Model interactions, neutrinos and antineutrinos in the early universe should be in thermal and chemical equilibrium with the photon- and $e^{\pm}$-plasma for temperatures $T > T_{\mathrm{weak}} \sim 1\,\mathrm{MeV}$. For $T \ll T_{\mathrm{weak}}$, the neutrinos and antineutrinos will be completely decoupled, comprising seas of "relic" particles freely falling through spacetime with energy-momentum and flavor distributions reflecting pre-decoupling equilibrium plus the expansion of the universe. This is analogous to the presently-decoupled cosmic microwave background (CMB) photons. These photons had been coupled and in thermal equilibrium in the early universe when $T > T_{\rm em} \approx 0.26\,{\rm eV}$.

Experiments have demonstrated that the neutrino energy (mass) eigenstates $|\nu_i\rangle$ are not coincident with the weak interaction (flavor) eigenstates $|\nu_\alpha\rangle$. These bases are related by the Maki-Nakagawa-Sakata (MNS) matrix, $|\nu_\alpha\rangle = \sum_i U^*_{\alpha i}|\nu_i\rangle$, where $\alpha = e, \mu, \tau$, and $i = 1, 2, 3$ denotes the mass eigenstates, with corresponding vacuum mass eigenvalues m_i, and where $U_{\alpha i}$ are the unitary transformation matrix elements (parameterized by 3 mixing angles θ_{12}, θ_{23}, θ_{13}, and a CP-violating phase δ).

Absolute neutrino masses remain unknown, but the neutrino mass-squared differences are measured. Studies of atmospheric neutrinos reveal a characteristic mass-squared splitting, $|\delta m^2_{\rm atm}| \approx 2.4 \times 10^{-3}\,{\rm eV}^2$, associated with $\nu_\mu \rightleftharpoons \nu_\tau$ mixing with $\sin^2\theta_{23} \approx 0.50$. Likewise, solar neutrino observations and reactor-based experimental data suggest that the solar neutrino deficit problem is solved by flavor transformation in the $\nu_e \rightleftharpoons \nu_{\mu/\tau}$ channel and that the characteristic mass-squared difference for this solution is $\delta m^2_\odot \approx 7.6 \times 10^{-5}\,{\rm eV}^2$, and that $\sin^2\theta_{12} \approx 0.31$. Current experimental limits on θ_{13} are $\sin^2\theta_{13} \leq 0.040$ (2σ limit) [1]. The CP-violating phase and ordering of the neutrino mass splittings remain unconstrained by experiment. In the "normal" neutrino mass hierarchy the solar neutrino mass-squared doublet lies below the atmospheric doublet; in the "inverted" mass hierarchy it is the other way around. This is illustrated in Fig. 5.1.

5.3 Neutrino Evolution

For $T > T_{\rm weak}$, prior to decoupling, solutions of the quantum kinetic equations for neutrino flavor evolution show that neutrinos will be forced by weak interaction-mediated scattering into flavor eigenstates [2, 3]. At epoch $T_{\rm weak}$, corresponding to scale factor $a_{\rm weak}$, the neutrino distribution functions for each flavor will be two-

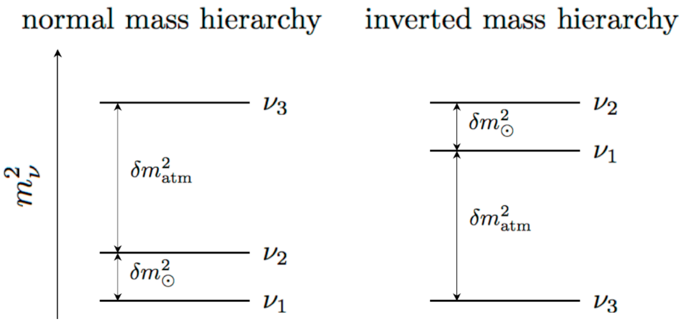

Figure 5.1: Neutrino mass eigenvalue ordering in the "normal mass hierarchy" on the left and the "inverted mass hierarchy" on the right.

parameter, Fermi-Dirac black bodies, with the number density of ν_α's in energy interval dE_ν given by

$$dn_{\nu_\alpha} = \frac{1}{2\pi^2} \cdot \frac{p^2}{e^{E_\nu/T_{\rm weak} - \eta_{\nu_\alpha}} + 1} \left(\frac{dE_\nu}{dp} \right)^{-1} dE_\nu, \tag{5.1}$$

where we employ natural units with $\hbar = c = k_B = 1$, the degeneracy parameter (ratio of chemical potential to temperature) for neutrino species ν_α is η_{ν_α}, and where the neutrino energy-momentum dispersion relation is

$$E_\nu = \sum_i |U_{\alpha i}|^2 \left(p^2 + m_i^2\right)^{1/2}, \tag{5.2}$$

with $p = |\mathbf{p}|$ the magnitude of the spacelike momentum. Here we will ignore small spectral distortions between ν_e and $\nu_{\mu,\tau}$ from $e^\pm$-annihilation.

Subsequent to decoupling, these pure flavor states can be regarded as collisionless, simply free falling through spacetime with their momentum components redshifting with the scale factor, $p \propto a^{-1}$. As a result, the number density of ν_α at an epoch with scale factor a is

$$dn_{\nu_\alpha}(a) \approx \frac{T_\nu^3(a)}{2\pi^2} \cdot \frac{\epsilon^2 d\epsilon}{e^{E_\nu(a)/T_{\rm weak} - \eta_{\nu_\alpha}} + 1}, \tag{5.3}$$

where $T_\nu(a) = T_{\rm weak} a_{\rm weak}/a$ is an effective "temperature" of the neutrinos, $\epsilon = p/T_\nu(a)$ is a co-moving invariant, and the energy-momentum dispersion relation is

$$E_\nu(a) \approx T_{\rm weak} \left(\epsilon^2 + \frac{\sum_i |U_{\alpha i}|^2 m_i^2}{T_{\rm weak}^2} \right)^{1/2}. \tag{5.4}$$

In both of these expressions, we have neglected corrections of order $(m_i/T_{\rm weak}\epsilon)^4$ which are small since experimental measurements of neutrino masses have $m_i \lesssim 1$ eV, $T_{\rm weak} \sim 1$ MeV, and small values of ϵ are suppressed in the neutrino distribution function, Eq. (5.3). The energy-momentum dispersion relation, Eq. (5.4), leads to the standard choice for the effective mass of a neutrino in flavor state ν_α,

$$m^2_{{\rm eff},\nu_\alpha} = \sum_i |U_{\alpha i}|^2 m_i^2. \tag{5.5}$$

This is the dynamical mass for an ultrarelativistic neutrino of flavor ν_α. However, we will show that when the neutrino momentum redshifts to a point where the neutrino's kinematics become less relativistic, this effective mass is no longer relevant in characterizing the energy-momentum dispersion relation.

Examining Eqs. (5.3) and (5.4), we notice that the distribution function for ν_α maintains a self-similar form with ϵ and η_{ν_α} being co-moving invariants. This form is suggestive of, though subtly different than, a Fermi-Dirac blackbody with temperature T_ν and degeneracy parameter η_{ν_α}. The energy distribution functions for neutrinos in mass eigenstates are a weighted sum of the flavor eigenstates,

$$dn_{\nu_i} = \sum_\alpha |U_{\alpha i}|^2 dn_{\nu_\alpha}. \tag{5.6}$$

If the degeneracy parameters for the three flavors were all equal, then the distribution function for the mass states would have the same Fermi-Dirac form. This follows from unitarity, $\sum_\alpha |U_{\alpha i}|^2 = 1$. However, in general the distribution functions of neutrinos in mass eigenstates would not have a Fermi-Dirac form where the degeneracy parameters were not identical for all three active flavors.

CMB- and large scale structure-derived neutrino mass limits typically are predicated on an assumption that these distribution functions have a Fermi-Dirac black body form. This assumption is invalid when the energy spectra of the various neutrino flavors are not identical, *i.e.,* when the neutrino degeneracy parameters (or, equivalently, the corresponding lepton numbers) are unequal.

The measured solar neutrino mixing parameters coupled with Big Bang Nucleosynthesis (BBN) considerations limit $\eta_{\nu_\alpha} < 0.15$ [4, 5] for all flavors and dictate that

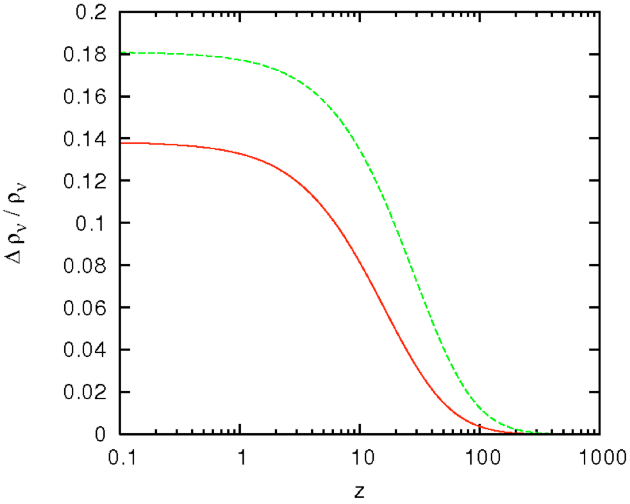

Figure 5.2: $(\rho_\nu^{(0)} - \rho_\nu)/\rho_\nu$ as a function of redshift. Solid curve is for $m_1 = 1$ meV in the normal neutrino mass hierarchy and the dashed curve is for $m_3 = 1$ meV in the inverted hierarchy.

the degeneracy parameters be within an order of magnitude of each other [4, 6, 7]. Consequently, the spectral and number density differences for the neutrino flavors stemming from disparate lepton numbers cannot be large, but conceivably could be $\lesssim 15\%$. Nevertheless, as neutrino mass limits improve with future higher precision CMB experiments and better large scale structure observations, it may be necessary to include the possibility of non-Fermi-Dirac energy spectra in these neutrino mass analyses. For the remainder of this letter, we will assume that all the neutrino degeneracy parameters are zero to illustrate another important result.

However, there is a more general issue associated with determining neutrino masses from cosmological data. A naive method of calculating ρ_ν, the energy density of neutrinos in the universe, is to use the effective mass in Eq. (5.5) and the number density distributions of neutrinos in flavor eigenstates,

$$\rho_\nu^{(0)} = \sum_\alpha \int (p^2 + m^2_{\mathrm{eff},\nu_\alpha})^{1/2} dn_{\nu_\alpha}. \tag{5.7}$$

However, if we wish to calculate the energy density of these quantum mechanical particles, we ought to consider the energy (mass) eigenstates in the calculation,

$$\begin{aligned}\rho_\nu &= \sum_i \int (p^2 + m_i^2)^{1/2} dn_{\nu_i} \\ &= \sum_{i,\alpha} \int |U_{\alpha i}|^2 (p^2 + m_i^2)^{1/2} dn_{\nu_\alpha}. \end{aligned} \tag{5.8}$$

At late times (large scale factors or equivalently small redshifts), the momenta of the neutrinos have redshifted to a point where they are comparable to the neutrino masses. We note that in this case the quantum mechanically consistent calculation diverges from the naive approach of using the effective neutrino masses. Fig. 5.2 shows the fractional difference between these two calculation techniques. At large redshifts, neutrino momenta are large enough that all three mass eigenstates are ultrarelativstic and masses have little effect on the overall energy density. On the other hand, at low redshifts, neutrino momenta have redshifted to a point where the kinematics of the neutrinos is no longer ultrarelativistic and rest mass becomes significant in the overall energy density. At this point the difference in the two methods manifests itself in the difference between the quantum mechanical expectation value for the mass, $\langle m \rangle$, and the root-mean-squared mass expectation value, $\langle m^2 \rangle^{1/2}$.

As can be seen in Fig. 5.2, the disparity in calculating the value of ρ_ν becomes significant, of order 10%, for redshifts of order $1 - 10$, at least for $m_1 \sim 1$ meV. This could be important because this is the epoch of structure formation in the universe where the energy density in neutrinos and the character of their kinematics are relevant to the formation of large scale structures.

One method of experimentally determining the mass of the neutrino using the CMB is by inferring the transfer function in the matter power spectrum at large wavenumbers (or small scales). Massive neutrinos contribute to the closure fraction in cold dark matter at the current epoch (as inferred by measurements of the CMB power spectrum), but at higher redshifts, when structure formation occurs, these neutrinos may act as hot dark matter. As a result, the amount of cold dark matter at these earlier epochs is reduced, suppressing the formation of large scale structure compared to a situation without massive neutrinos. A comparison of the

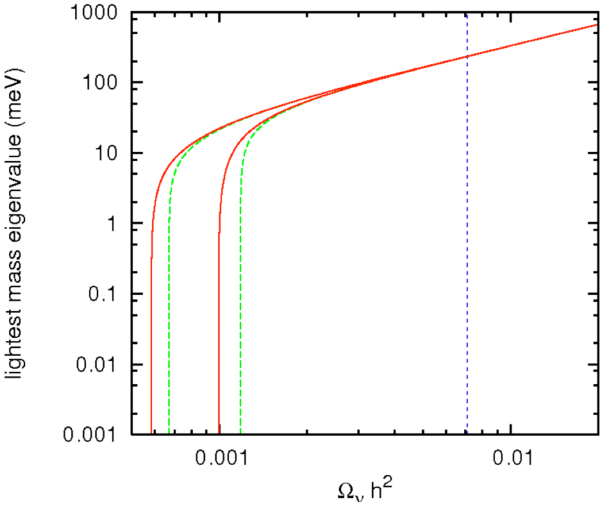

Figure 5.3: The lightest mass eigenvalue as a function of $\Omega_\nu h^2$. Solid curves use the quantum mechanical calculation method described here, while dashed curves use the naive method illustrated in Eq. (5.7). The curves on the left correspond to the normal neutrino mass hierarchy, while the curves on the right are for the inverted hierarchy. Also plotted is the limit from the WMAP 5-year data, $\Omega_\nu h^2 < 0.0071$ (95% confidence limit).

observationally-inferred matter power spectrum with the power spectrum expected without the effects of massive neutrinos implies Ω_ν, the closure fraction contributed by neutrinos. Determining the energy density in neutrinos at late times is an important aspect of this procedure and is necessary in deriving neutrino masses.

This is a concern since the naive computation of neutrino energy densities differs from the quantum mechanical method. Fig. 5.3 shows the relationship between the lightest mass eigenvalue (m_1 in the normal hierarchy or m_3 in the inverted hierarchy) and the measured value of Ω_ν. We see that the limit on $\Omega_\nu h^2$ for excluding the inverted hierarchy is reduced by about 15%. (Here h is the Hubble parameter in units of 100 km s^{-1} Mpc^{-1}.) In addition, at low mass values, we see that the mass is a very sensitive function of $\Omega_\nu h^2$. As a result, mass measurements using this method are sensitive to the precision in the inferred measurement of $\Omega_\nu h^2$. A 10% error in the measurement of $\Omega_\nu h^2$ would prevent us from inferring a lightest neutrino mass

$\lesssim 5$ meV. For neutrino masses $\lesssim 10-20$ meV, there can be a significant error in determining the lightest mass eigenvalue if the quantum mechanical treatment we present here was not used.

The current observational limits (shown in Fig. 5.3 as the five-year WMAP data [8]), are nowhere near the regime where a consistent quantum mechanical treatment is necessary. However, the quantum mechanical analysis may be relevant for higher precision future neutrino mass inferences based on transfer function arguments.

One possible complication has not been discussed. It has been claimed that the phase space density of the relic neutrinos is high so that quantum coherence between momentum states may develop as a result of fermion exchange symmetry [9]. We note that the initial distribution of neutrinos, Eq. (5.1), is determined by Fermi-Dirac quantum statistics because it reflects emergence from an environment where thermal equilibrium obtains. Moreover, the general relativistic analog to Liouville's Theorem assures us that as these neutrinos freely stream through spacetime, their proper phase space density remains unchanged and therefore continues to respect the Pauli principle.

5.4 Gravitational Induced Decoherence

There is a second, peculiar effect born from the fact that these relic neutrinos decouple from the plasma of the early universe in flavor eigenstates. A decoupled relic neutrino ν_α can be regarded as a coherent superposition of mass states with common spacelike momentum $\mathbf{p}$. As the universe expands and this momentum redshifts downward, there will come an epoch where the higher rest mass component of this flavor wavepacket will tend toward a nonrelativistic velocity, while the lower mass components speed along at nearly the speed of light. From this point onward the spatial scale of the coherent flavor wavepacket will grow rapidly with time. The net result is that at the present epoch, and at the redshift $z \sim 1$ epoch where neutrinos are falling into dark matter potential wells, the relic neutrinos are coherent structures with sizes considerably larger than the spatial scale of the gravitational potential wells

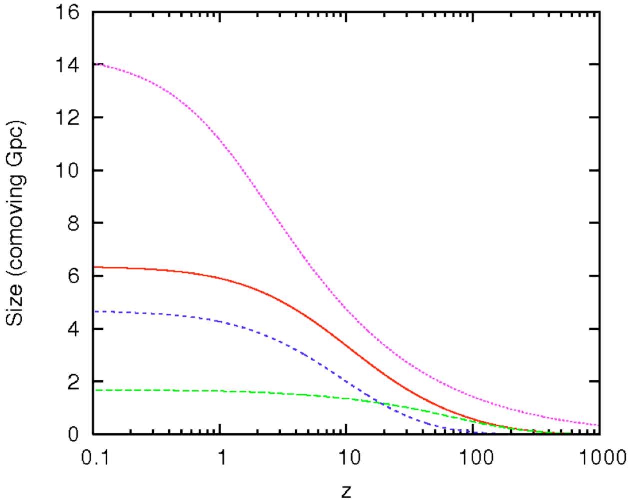

Figure 5.4: The separation of mass eigenstates as a function of redshift. Solid curve for $\nu_1 - \nu_3$, long dashed curve for $\nu_2 - \nu_3$, and medium dashed curve for $\nu_1 - \nu_2$. The causal horizon is the short dashed curve.

of galaxies and, in some cases, comparable to the causal horizon size.

Using the normal neutrino mass hierarchy scheme and $m_1 = 1\,\mathrm{meV}$, Fig. 5.4 shows how the size of a relic neutrino flavor wavepacket would grow with the expansion of the universe.

The more massive components of these neutrino flavor wave packets become non-relativistic very early on, and it is interesting that the two different possibilities for the neutrino mass hierarchy yield quite different kinematic histories for the relic neutrinos. For example, with $m_1 = 1\,\mathrm{meV}$ in the normal neutrino mass hierarchy, the measured neutrino mass-squared differences imply that $m_2 \approx 8.7\,\mathrm{meV}$, and $m_3 \approx 49\,\mathrm{meV}$. Consequentially, as the wave packets for the three mass eigenstates redshift in the expanding universe, the wave packet corresponding to each of the three mass eigenstates tends to become non-relativistic at three distinct epochs, $z \sim 5$, 50, and 300 respectively. These are the epochs in which mass eigenstates separate as the neutrino flavor wavepacket travels through spacetime, as can be seen in Fig. 5.4.

On the other hand, the inverted neutrino mass hierarchy would yield a different history. The three neutrino masses would be $m_3 = 1$ meV, $m_1 \approx 49$ meV, and $m_2 \approx 50$ meV, which would imply that the lightest mass eigenstate would tend to be non-relativistic at $z \sim 5$ while the two heavier mass eigenstates would become non-relativistic at $z \sim 300$.

If the lightest neutrino mass eigenvalue is $\ll 1\,\mathrm{meV}$, then the relic neutrinos might be coherent flavor eigenstates consisting of superpositions of relativistic and nonrelativistic components at the epoch $z \approx 2$ when these particles begin to fall into the gravitational potential wells associated with galaxies. Though the role of spacetime curvature in quantum state reduction is not settled [10–12], an obvious set of questions is posed.

First, does the process of "capturing" a neutrino into a gravitational potential well lead to flavor wavepacket de-coherence? Given the disparity between the relatively small local spacetime curvature scale and the flavor wavepacket size in this example, it is plausible that the gravitational tidal stress induces de-coherence. In this picture, the neutrino clustering/capture process would be tantamount to a "measurement," with capture occurring when flavor wave function collapse yields a nonrelativistic mass-energy eigenstate.

However, this line of reasoning calls into question the premise of coherent flavor eigenstates at the epoch when neutrinos are captured into, *e.g.,* clusters of galaxies. Fig. 5.4 shows that the relic neutrino flavor wavepackets can have spatial extents that are on the order of the causal horizon size. In this case, the wavepacket sizes are comparable to the spacetime curvature scale of the universe itself. In this picture, the complete de-coherence history of the relic neutrinos could be obtained only through solution of a fully covariant Dirac-like field development equation with all matter and dark matter distributions *plus* a prescription for de-coherence (wave function collapse).

An alternative possibility is that de-coherence would never happen. In this picture spacetime curvature would merely cause the relic neutrino flavor wavepackets to suffer phase space distortion as they fall through spacetime and into gravitational potential wells.

In either case, unitarity implies that the comoving number density of neutrinos at a given mass is fixed. As a result, unless there is new physics associated with curvature-induced decoherence, the accretion history of neutrinos in potential wells should depend only on the neutrino masses and, in particular, the mass hierarchy.

This work was supported in part by NSF grant PHY-06-53626. We would like to thank B. Keating, Y. Raphaelli, E. Gawiser and especially M. Shimon for many valuable conversations.

Chapter 5, in part, is a reprint of material previously published as G. M. Fuller and C. T. Kishimoto, "Quantum Coherence of Relic Neutrinos", *Physical Review Letters* **102**, 201303 (2009). I was the primary investigator and author of this paper.

Bibliography

[1] T. Schwetz, M. Tórtola and J. W. F. Valle, New Journal of Physics **10**, 113011 (2008).

[2] C. T. Kishimoto and G. M. Fuller, Physical Review D **78**, 023524 (2008).

[3] N. F. Bell, R. R. Volkas and Y. Y. Y. Wong, Physical Review D **59**, 113001 (1999).

[4] K. Abazajian, N. F. Bell, G. M. Fuller and Y. Y. Y. Wong, Physical Review D **72**, 063004 (2005).

[5] J. P. Kneller, R. J. Scherrer, G. Steigman and T. P. Walker, Physical Review D **64**, 123506 (2001).

[6] K. N. Abazajian, J. F. Beacom and N. F. Bell, Physical Review D **66**, 013008 (2002).

[7] A. D. Dolgov, S. H. Hansen, S. Pastor, S. T. Petcov, G. G. Raffelt and D. V. Semikoz, Nuclear Physics B **632**, 363 (2002).

[8] E. Komatsu, J. Dunkley, M. R. Nolta, C. L. Bennett, B. Gold, G. Hinshaw, N. Jarosik, D. Larson, M. Limon, L. Page, D. N. Spergel, M. Halpern, R. S. Hill, A. Kogut, S. S. Meyer, G. S. Tucker, J. L. Weiland, E. Wollack and E. L. Wright, Astrophysical Journal Supplement Series **180**, 330 (2009).

[9] D. Pfenniger and V. Muccione, Astronomy & Astrophysics **456**, 45 (2006).

[10] R. Penrose, General Relativity and Gravitation **28**, 581 (1996).

[11] J. Christian, Physical Review Letters **95**, 160403 (2005).

[12] R. Feynman, *Feynman Lectures on Gravitation,* edited by B. Hatfield (Addison-Wesley, Reading, MA, 1995).

Appendix A

Physical Constants and Natural Units

Table A.1 lists a number of physical constants that are relevant in the presentation of this dissertation. The values presented are the current (2006) values as recommended by the Committee on Data for Science and Technology (CODATA), and may be found on the website of the National Institute of Standards and Technology (NIST): `http://physics.nist.gov/cuu/Constants/index.html` . The values are presented in a common form representing both the mean value and standard uncertainty (1-σ uncertainties), where $(a.bcde \pm 0.00fg) \times 10^h$ is repesented as $a.bcde(fg) \times 10^h$. The values are given in *cgs* (centimeter-gram-second) units [as opposed to SI, *a.k.a mks* (meter-kilogram-second), units], which are commonly used in astrophysics.

Throughout this dissertation, with the exception of Chapter 4 and where it is otherwise noted, natural units are used where $\hbar = c = k_B = 1$. By removing three dimensionful constants, which incorporate four independent physical units, we reduce the number of dimensions to one. It is useful in astroparticle physics to express all units in terms of MeV. Table A.2 includes a number of derived physical constants that are useful in understanding natural units. The errors shown are consistent not only with the individual errors of the parameters, but also with covariance between

Table A.1: Fundamental Physical Constants in *cgs* units. *Source: 2006 CODATA values.*

Constant	Value		
Boltzmann Constant	k_B	$1.380\ 6504(24) \times 10^{-16}$	erg K^{-1}
Electron Mass	m_e	$9.109\ 382\ 15(45) \times 10^{-28}$	g
Electron Volt	eV	$1.602\ 176\ 487(40) \times 10^{-12}$	erg
Gravitational Constant	G_N	$6.674\ 28(67) \times 10^{-8}$	erg cm g^{-2}
Neutron Mass	m_n	$1.674\ 927\ 211(84) \times 10^{-24}$	g
Proton Mass	m_p	$1.672\ 621\ 637(83) \times 10^{-24}$	g
Reduced Planck constant	$\hbar$	$1.054\ 571\ 628(53) \times 10^{-27}$	erg s
Speed of light in vacuum	c	$2.997\ 924\ 58(\mathrm{exact}) \times 10^{10}$	cm s^{-1}

the experimental values of the fundamental physical constants presented in Table A.1.

A.1 Temperature

The temperature is converted using the Boltzmann constant,

$$T = k_B T = \left[8.617\ 343(15) \times 10^{-2}\right] T_9 \text{ MeV},$$

where $T_9 = T/(10^9 \text{ K})$ is the temperature in units of 10^9 K.

A.2 Length and Time

As is commonly the case in relativity, we set $c = 1$, which allows us to relate temporal scales to spatial scales,

$$1 \text{ s} = 1 \text{ light-second} = 2.997\ 924\ 58 \times 10^{10} \text{ cm}.$$

By using the relationship $\hbar c = 1$, a length scale can be related to an inverse energy scale,

$$1 \text{ cm} = \frac{1 \text{ cm}}{\hbar c} = 5.067\ 731\ 16(13) \times 10^{10} \text{ MeV}^{-1}.$$

Table A.2: Derived Physical Constants using natural units. *Source: 2006 CODATA values.*

Constant	Value		
	$\hbar c$	$1.973\ 269\ 631(50) \times 10^{2}$	MeV fm
Boltzmann Constant	k_B	$8.617\ 343(15) \times 10^{-11}$	MeV K^{-1}
Electron Mass	$m_e c^2$	$0.510\ 998\ 910(13)$	MeV
Fermi Constant	$G_F/(\hbar c)^3$	$1.166\ 37(1) \times 10^{-11}$	MeV^{-2}
Neutron Mass	$m_n c^2$	$9.395\ 653\ 46(23) \times 10^{2}$	MeV
Planck Mass	$m_{pl} c^2$	$1.220\ 892(61) \times 10^{22}$	MeV
Proton Mass	$m_p c^2$	$9.382\ 720\ 13(23) \times 10^{2}$	MeV

As a result, a density is given by

$$1\ \mathrm{cm}^{-3} = 1\ \mathrm{cm}^{-3}\,(\hbar c)^3 = 7.683\ 503\ 55(58) \times 10^{-33}\ \mathrm{MeV}^3.$$

A.3 Mass

As is also the case in relativity, setting $c = 1$ allows us to identify masses with energies,

$$1\ \mathrm{g} = (1\ \mathrm{g})\,c^2 = 5.609\ 589\ 12(14) \times 10^{26}\ \mathrm{MeV}.$$

Some useful figures of merit are the mass of a nucleon (proton or neutron) is approximately 1 GeV, and the mass of an electron is approximately 500 keV.

Another important figure of merit is the mass of the sun. The solar mass, $M_\odot$, is often a convenient unit in astrophysics whose measured value from the Particle Data Group is

$$M_\odot = 1.988\ 4(2) \times 10^{33}\ \mathrm{g},$$

or expressed in MeV,

$$M_\odot = 1.115\ 4(1) \times 10^{60}\ \mathrm{MeV}.$$

The Planck mass is a mass scale that can be created by the physical constants $\hbar$,

c, and G_N, and is defined as

$$m_{pl} = \sqrt{\frac{\hbar c}{G_N}} = 2.176\ 44(11) \times 10^{-5} g,$$

or in MeV,

$$m_{pl} = 1.220\ 892(61) \times 10^{22}\ \text{MeV}.$$

The Planck mass is significant in this dissertation in its relationship to Newton's gravitational constant in natural units,

$$G_N = \frac{1}{m_{pl}^2}.$$